Millimeter-Wave Band Pass Distributed Amplifier for Low-Cost Active Multi-Beam Antennas

by

Mehrdad Fahimnia

A thesis
presented to the University of Waterloo
in fulfillment of the
thesis requirement for the degree of
Doctor of Philosophy
in
Electrical and Computer Engineering

Waterloo, Ontario, Canada, 2012

Abstract

Recently, there have been a great interest in the millimeter-wave (mmW) and terahertz (THz) bands due to the unique features they provide for various applications. For example, the mmW is not significantly affected by the atmospheric constraints and it can penetrate through clothing and other dielectric materials. Therefore, it is suitable for a vast range of imaging applications such as vision, safety, health, environmental studies, security and non-destructive testing.

Millimeter-wave imaging systems have been conventionally used for high end applications implementing sophisticated and expensive technologies. Recent advancements in the silicon integrated and low loss material passive technologies have created a great opportunity to study the feasibility of low cost mmW imaging systems. However, there are several challenges to be addressed first. Examples are modeling of active and passive devices and their low performance, highly attenuated channel and poor signal to noise ratio in the mmW.

The main objective of this thesis is to investigate and develop new technologies enabling cost-effective implementation of mmW and sub-mmW imaging systems. To achieve this goal, an integrated active Rotman lens architecture is proposed as an ultimate solution to combine the unique properties of a Rotman lens with the superiority of CMOS technology for fabrication of cost effective integrated mmW systems.

However, due to the limited sensitivity of on-chip detectors in the mmW, a large number of high gain, wide-band and miniaturized mmW Low Noise Amplifiers (LNA) are required to implement the proposed integrated Rotman lens architecture. A unique solution presented in this thesis is the novel Band Pass Distributed Amplifier (BPDA) topology. In this new topology, by short circuiting the line terminations in a Conventional Distributed Amplifier (CDA), standing waves are created in its artificial transmission lines. Conventionally, standing waves are strongly avoided by carefully matching these lines to $50\,\Omega$ in order to prevent instability of the amplifier. This causes that a large portion of the signal be absorbed in these resistive terminations. In this thesis, it is shown that due to presence of highly lossy parasitics of CMOS transistor at the mmW the amplifier stability is inherently achieved. Moreover, by eliminating these lossy and noise terminations in the CDA, the amplifier gain is boosted and its noise figure is reduced. In addition, a considerable decrease in the number of elements enables low power realization of many amplifiers in a small chip area.

Using the lumped element model of the transistor, the transfer function of a single stage BPDAs is derived and compared to its conventional counter part. A methodology to design a single stage BPDA to achieve all the design goals is presented. Using the presented design guidelines, amplifiers for different mmW frequencies have been designed, fabricated and tested. Using only 4 transistors, a 60 GHz amplifier is fabricated on a very small chip area of $0.105\,\mathrm{mm}^2$ by a low-cost 130 nm CMOS technology. A peak gain of 14.7 dB and a noise figure of 6 dB are measured for this fabricated amplifier.

Moreover, it is shown that by further circuit optimization, high gain amplification can be realized at frequencies above the cut-off frequency of the transistor. Simulations show 32 and 28 dB gain can be obtained by implementing only 6 transistors using this CMOS technology at 60 and 77 GHz. A 4-stage 85 GHz amplifier is also designed and fabricated and a measured gain of 10 dB at 82 GHz is achieved with a 3 dB bandwidth of 11 GHz from 80 to 91 GHz. A good agreement between the simulated and measured results verifies the accuracy of the design procedure.

In addition, a multi-stage wide-band BPDA has been designed to show the ability of the proposed topology for design of wide band mmW amplifiers using the CMOS technology. Simulated gain of 20.5 dB with a considerable 3 dB bandwidth of 38 GHz from 30 to 68 GHz is achieved while the noise figure is less than 6 dB in the whole bandwidth. An amplifier figure of merit is defined in terms of gain, noise figure, chip area, band width and power consumption. The results are compared to those of the state of the art to demonstrate the advantages of the proposed circuit topology and presented design techniques.

Finally, a Rotman lens is designed and optimized by choosing a very small Focal Lens Ratio (FL), and a high measured efficiency of greater than 30% is achieved while the lens dimensions are less than 6 mm. The lens is designed and implemented using a low cost Alumina substrate and conventional microstrip lines to ease its integration with the active parts of the system.

Acknowledgements

I would like to express my profound gratitude to my smart supervisor Professor Safieddin Safavi-Naeini for his supervision during my Ph.D. program. He supported me in many ways and provided me with great opportunities.

I wish to express my deepest gratitude to my lovely wife, for everything she did to make my PhD life as comfortable and easy as possible and has always stood by my side patiently and lovingly, and to my wonderful children.

My sincere thanks to Professor M. Jamal Deen from McMaster University for accepting to be the external examiner of my defence session. I am also thankful to my Examining Committee members, Dr. Nasser Lashgarian Azad, Dr. Siddharth Garg and Dr. Slim Boumaiza for reviewing my thesis and giving their comments and suggestions.

My special thanks to my supervisor at University of Tehran, Dr. Mahmoud Mahoammad-Taheri and Dr. Ying Wang at University of Ontario Institute of Technology for their priceless support and fruitful research collaboration. I am very grateful to James Dietrich at advanced RF lab at University of Manitoba for his profound support in the test and characterization of millimeter-wave chips, Phil Regier for CAD support and Bill Jolly for test and assembly support.

I would like to acknowledge the Natural Sciences and Engineering Research Council of Canada (NSERC) and Research in Motion (RIM) for funding my research, CMC Microsystems for the tools and chip fabrication and to the all the supportive people in Agilent technologies and ComDev for their kind supports.

There are many friends who helped me in some way or another during my PhD studies. Special mention must go to Dr. Mohammad-Reza Nezhad-Ahmadi, Dr. Behzad Biglarbegian and Ahmed Abdellatif Shehata for their support and research collaboration.

Also I would like to thank Prof. Raafat Mansour, Prof. Sorin Voinigescu, Prof. Reza Faraji-Dana, Dr. Reza Rafi, Dr. Siamak Fouladi, Dr. Leila Yousefi, Dr. Mehrbod Mohajer, Dr. Maher Bakri Kassem, Khosrow Modaresi, Aidin Taeb, Zahra Sotoodeh, Sara Attar, Chris Schroeder and Eric Dacquay for their help. Thanks to all of my friends for their technical help and wonderful friendship. My apologies to anyone I have missed.

Last but not least, I am really indebted to my parents.

Dedication

In loving memory of my father
Mr. Hadi Fahimnia,
my brother Amir-Hossein Fahimnia
and my sister Maryam Fahimnia.

Contents

List of Tables **x**

List of Figures **xi**

List of Symbols and Abbreviations **xv**

1 INTRODUCTION **1**

1.1 Motivation 1

1.2 Thesis Overview 4

1.3 Main Contributions 5

2 PASSIVE MILLIMETER WAVE IMAGING SYSTEMS: A TECHNOLOGY OVERVIEW **6**

2.1 Introduction 6

2.2 Passive MmW Imaging Systems 7

2.2.1 Basic radiometer architecture 10

2.2.2 The Dicke-Type radiometer architecture 15

2.3 Active Rotman Lens Architecture for Passive MmW Imaging Systems 16

2.3.1 An overview of radiometer based imaging systems 16

2.3.2 Active Rotman lens architecture 17

2.3.3 General noise analysis 19

2.3.4 Radiometer sensitivity analysis 21

2.3.5 Performance comparison of active Rotman lens architectures 22

2.3.6 High gain LNA requirement for active Rotman lens architectures 24

2.4 Conclusion 25

3 A NEW BAND PASS DISTRIBUTED AMPLIFIER TOPOLOGY: THEORY AND DESIGN 26

3.1 Introduction 26

3.2 Distributed Amplifier (DA) 27

3.2.1 Conventional Distributed Amplifier (CDA) 27

3.2.2 Conventional Band Pass Distributed Amplifier 29

3.3 The Novel Band Pass Distributed Amplifier (BPDA) Topology [1] 30

3.3.1 Single stage CDA and single stage BPDA transfer functions 32

3.3.2 Bandwidth and center frequency calculations 36

3.3.3 Input/output matchings 38

3.3.4 Stability consideration 38

3.3.5 TL (Transmission Line) analysis of the single stage BPDA topolgy [2] 42

3.4 Conclusion 46

4 DESIGN AND FABRICATION OF OPTIMUM MILLIMETER WAVE LOW NOISE BAND PASS DAS (BPDA) 48

4.1 Introduction 48

4.2 Characterization of an On-Chip Transmission Line for CMOS MMIC Applications [3] 49

4.2.1 On-chip TL structure 50

4.2.2 TL EM-simulation 51

4.2.3 TL fabrication and measurement 51

4.2.4 TL parameter extraction 52

4.3 Low Noise Design of a Single Stage BPDA [4] 53

4.4 Design and Fabrication of a V-band CMOS SSBPDA [5] 56

4.5 CMOS Amplifiers Which Can Operate Above f_T 63

4.6 A Multi-Stage BPDA for Wide-Band MmW Applications 66

4.7 Conclusion 68

5 MINIATURIZED, LOW COST ROTMAN LENS FOR MILLIMETER WAVE APPLICATION 71
5.1 Introduction 71
5.2 Beam Forming Techniques 71
5.3 Rotman Lens for Beam Forming 74
5.4 Miniaturized Rotman Lens for MmW Imaging Systems 75
  5.4.1 Microstrip line for mmW Rotman lens 76
  5.4.2 Stripline for mmW Rotman lens 77
  5.4.3 Design of miniaturized mmW Rotman Lenses 79
  5.4.4 Design and fabrication of miniaturized Rotman Lens at 77 GHz 81
5.5 Conclusion 84

6 CONCLUSIONS AND FUTURE DIRECTIONS 85
6.1 Conclusion and Contributions 85
6.2 Future Research Directions 88

APPENDICES 89

A An accurate, simple and scalable model for mmW CMOS transistors 90

B Design equations for Rotman lens 94

Bibliography 100

List of Tables

2.1 Different sensor categories for the millimeter-wave and THz regions [6]. 8

2.2 The performance comparison of reported mmW detectors and the required LNA gain to achieve 0.4 K $NEDT$ for a typical mmW imaging systems with β=0.6, B=15 GHz, NF_{LNA}=8 dB using equation 2.6. . 14

2.3 Typical building block parameters for active Rotman lens (RL) architectures shown in Fig. 2.4. 22

2.4 Resulted imager sensitivity for architectures shown in Fig. 2.4. . . . 23

3.1 Performance of the published CBPDAs in the literature. 31

3.2 Comparison Results 46

4.1 Performance comparison of the designed and fabricated LNAs to the prior art. 62

4.2 Performance of the recently published CDAs in the literature using different fabrication technologies. 69

5.1 Summary of the typical performance characteristics of the microwave beam-forming systems [7]. 73

5.2 The lens parameters for some of the designed mmW Rotman lenses. 80

A.1 Scalable model parameters of transistors versus gate width, W at 77 GHz [5]. 92

List of Figures

1.1 The RF, microwave and millimeter-wave range of frequencies [8]. . . 2

2.1 Specific atmospheric attenuation in the dry air and in the presence of the atmospheric constrains: (a) Fog (0.1 gr/m3, 100 m visibility and 100% relative humidity) and (b)Light (2.5 mm/hr) and medium rain (5 mm/hr). [9] 9

2.2 Two main architectures for passive millimeter wave imaging systems: (a) Heterodyne and (b) Direct detection. 11

2.3 Block diagram of a Dicke-type radiometer. 15

2.4 m by n active Rotman lens architectures. a) conventional configuration [96] and proposed configurations using b) post lens LNAs c) pre lens LNAs and d) both pre and post lens LNAs. 18

2.5 Simplified block diagram of a m by n active Rotman lens configuration. 20

2.6 Resulted sensitivity of each imager architecture of Fig. 2.4 as a function of its detector performance, NEP, for typical imager parameters. 23

2.7 LNA gain and NF requirements for the active Rotman lens architecture shown in Fig. 2.4 (b) as a function of its detector performance, NEP. 24

3.1 Circuit diagram of a conventional distributed amplifier (CDA). . . . 28

3.2 Circuit diagram of a conventional BPDA using low pass to band pass transformation [10]. 30

3.3 Circuit diagram of the proposed band pass distributed amplifier (BPDA). 32

3.4 Topology of a single stage DA: (a) the CDA and (b) the proposed BPDA. 32

3.5 Equivalent small signal circuit for: (a) the Conventional DA (CDA) and (b) the proposed band pass DA (BPDA). 33

3.6 Gain comparison of the single stage DA for different termination resistors ($R_d = R_g$). The gain cell parameters are: $L_g = 130$ pF, $L_d = 140$ pF, $C_{gs} = 95$ fF, $C_{ds} = 65$ fF, $R_{gs} = 4\,\Omega$, $R_{ds} = 55\,\Omega$, $g_m = 45$ mS and $R_L = R_S = 50\,\Omega$ (see Fig. 3.4). 36

3.7 Noise figure comparison of different DA topologies. 36

3.8 Input and output matching of band pass DA for the gain cell with the parameters given in Fig. 3.6 and with $L_{in} = 78$ pH and $L_{out} = 0$ pH. 39

3.9 Input and output stability factors of a proposed BPDA with added (a) C_{gd}=10 fF (b) C_{gd}=20 fF and (c) C_{gd}=20 fF and L_s=10 pH. . . . 41

3.10 Topology of a single stage: a) Single stage DA and b) the proposed band pass DA. 42

3.11 Comparison of gain functions for: (a) G_1, H_1, (b) G_2, H_2 for single gain cell and (c) power gains G and H for a 2 stages CSSDA using the TL model (dashed line) and lumped element model (solid line). 45

4.1 A high quality factor microstrip transmission line implemented in the CMOS technology. (a) The simplified structure and (b) the cross section [3]. 50

4.2 Simulated E-field distribution at the wave ports of a GMSL. 51

4.3 Die photo of fabricated lines with (a) 100 μm and (b) 200 μm lengths. 52

4.4 Comparison of extracted and simulated S-parameters for fabricated 100 μm line segment. (a) S_{21} and (b) S_{11}. 53

4.5 Extracted and simulated TL paraments for a 100 μm line segment. (a) Attenuation constant and (b) Phase constant. 53

4.6 The circuit diagram of the proposed gain cell with degeneration inductors. 54

4.7 Effect of L_s in the gain cell on trade-off between (a) power gain, $|S_{21}|$ and (b) stability factor, K. 55

4.8 Noise figure versus L_{gg} for the designed gain cell at 62 GHz. 56

4.9 The simplified schematic of the fabricated 4-stage cascaded BPDA. 57

4.10 The comparison between simulated and measured S-parameters for the fabricated V-band amplifiers. 58

4.11 (a) Measured stability parameters for different values of L_s (b) Noise figure comparison between simulation and measurement for L_s=20 pH. 59

4.12 Die photo of the fabricated amplifiers. 60

4.13 Simulated gain and input/output matching for the designed 6-stage amplifier at 60 GHz. 60

4.14 (a) Simulated stability parameters and (b) Noise performance for the designed 6-stage amplifier. 61

4.15 Measured S-parameters for the designed W-band amplifiers. 64

4.16 (a) Simulated stability parameters and (b) noise characteristics for the W-band designed amplifier. 64

4.17 Comparison between simulated and measured results for the fabricated 85 GHz amplifier for its (a) power gain and (b) reverse isolation. 65

4.18 Comparison between simulated and measured matchings for the fabricated 85 GHz amplifier for (a) input and (b) output. 65

4.19 Die photo of the fabricated 85 GHz amplifier. 66

4.20 The simplified schematic of the designed multi-stage BPDA consisting of three cascaded of a 2-stage BPDA. 67

4.21 Simulated S-parameters for the designed multi-stage BPDA. 67

4.22 Simulated noise figure, NF_{min}, input and output stability measure (μ and $\acute{\mu}$ for the designed multi-stage BPDA. 68

5.1 Diagram of a Rotman lens [11]. 75

5.2 Microstrip line. a)The structure and main parameters. b) the Electric (E) and magnetic (M) field lines. [12] 77

5.3 Stripline. a)The structure and main parameters. b) the Electric (E) and magnetic (M) field lines. [12] 78

5.4 Simulated Electric field distribution for the designed 4 by 4 lens on a Roger 3010 substrate at 15 GHz. 81

5.5 The diagram of the designed miniaturized 77 GHz stripline Rotman lens with 6 array ports and 7 beam ports on an Alumina substrate. 82

5.6 The simulated average insertion loss of the beam ports for the designed lens of Figure 5.5. 82

5.7 Simulated Electric field distribution for the designed 4 by 4 lens on an Alumina substrate at 77 GHz. 83

5.8 Photo of the fabricated 77 GHz Rotman lens on Alumina substrate. 83

5.9 The simulated and measured array factor for the fabricated lens at 77 GHz. 84

A.1 Two port scalable mmW transistor model 91

A.2 Frequency dependency of extracted model parameters for three different transistor gate widths. (a) R_{ds} (b) C_{ds} (c) C_{gs} (d) C_{gd} (e) R_{gs} (f) g_m and (g) τ. 93

A.1 Diagram of a Rotman lens [11]. 95

List of Symbols and Abbreviations

α	Scan angle
β	Pre-LNA attenuation factor
γ	Propagation constant
ϵ	Dielectric constant
η	Element spacing
λ	Wavelength
φ	Steering angle
τ	Integration time
F	Noise factor
f_{max}	Maximun frequency of oscillation
f_T	Unity gain frequency
k_B	Boltzman's constant
K	Rollet's stability factor
$NEDT$	Noise equivalent difference temperature
NEP	Noise equivalent power
NF	Noise figure
NF_{min}	Minimum noise figure
Q	Quality factor
$\mathcal{R}$	Responsivity
T	Absolute temperature
A/D	Analog to Digital
BEOL	Back End Of Line
BPDA	Band Pass Distributed Amplifier
BPF	Band Pass Filter
BW	Band-Width
CAD	Computer Aided Design
CBPDA	Conventional Band Pass Distributed Amplifier
CDA	Conventional Distributed Amplifier
CS	Common Source
CSSBPDA	Cascaded Single-Stage Band Pass Distributed Amplifier
CMOS	Complementary Metal Oxide Semiconductor
CPW	Coplanar Wave-Guide
DA	Distributed Amplifier
dB	Decibels
DNA	Deoxyribo-Nucleic Acid
DSP	Digital Signal Processing
EM	Electro-Magnetic
F	Noise factor
FL	Focal Length
FOM	Figure of Merit

FOV	Field of view
GCPW	Guided Coplanar Wave-Guide
GMSL	Guided Micro Strip Line
GHz	Giga Hertz
HFSS	High Frequency Structure Simulator
IF	Intermediate Frequency
III-V	Three Five Compound
IIP3	3rd-order Input Intercept Point
InP	Indium Phosphide
ISS	Impedance Standard Substrate
KCL	Kirchhoff's Current Law
KVL	Kirchhoff's Voltage Law
LNA	Low Noise Amplifier
LRRM	Line Reflect Reflect Match
MAG	Maximum Available Gaine
MESFET	Metal Semiconductor Field Effect Transistor
MIMIC	Millimeter-Wave Monolithic Integrated Circuit
mmW	Millimeter-Wave
MOS	Metal Oxide Semiconductor
MOSFET	Metal Oxide Semiconductor Field Effect Transistor
MSL	Micro Strip Line
NDI	Non-Destructive Inspection
NF	Noise figure
NMOS	N-type Metal Oxide Semiconductor
PCB	Printed Circuit Board
RADAR	RAdio Detection And Ranging
RMS	Root Mean Square
RF	Radio Frequency
RL	Rotman Lens
SiGe	Silicon Germanium
SIW	Substrate Integrated Waveguide
SNR	Signal-to-Noise Ratio
SPDT	Single Pole Double Throw
SSDA	Single-Stage Distributed Amplifier
TE	Transverse Electric
TEM	Transverse Electromagnetic
THz	Terahertz
TL	Transmission Line
TM	Transverse Magnetic
TWA	Travelling Wave Amplifier
VNA	Vector Network Analyzer

Chapter 1

INTRODUCTION

1.1 Motivation

Nano-metric silicon technologies have made a revolution in RF systems and enabled incredible advancements in the communication world. Today, a small hand held device can do many tasks; each of them required a big computer a decade ago if possible. Now, industries and research communities are moving towards Giga-bit-per-second communication in future generation mobile devices. Furthermore, nano-metric silicon revolution is rapidly extending to other mass market applications such as millimeter-wave (mmW) car-radar and imaging applications systems.

The range of frequencies whose wavelength are in the order of millimeter corresponds to 30 GHz to 300 GHz frequency band in free-space radio-wave propagations. Terahertz (THz) or sub-millimeter wave radiation refers to a frequency range from 100 GHz up to 10 THz. Various parts of the spectrum between microwave and infra-red are shown in Figure 1.1.

This spectrum has received a great amount of interest among scientists and engineers for many years and has only recently become a hot technology research topic with real market potential. The scope of this research is to explore technologies and architectures to enable implementation of low cost imaging systems using electromagnetic waves whose spectrum is between 30 GHz to 1 THz.

Past applications in mmW and sub-mmW have generally been restricted to sophisticated scientific experimentation or special applications due to technical limi-

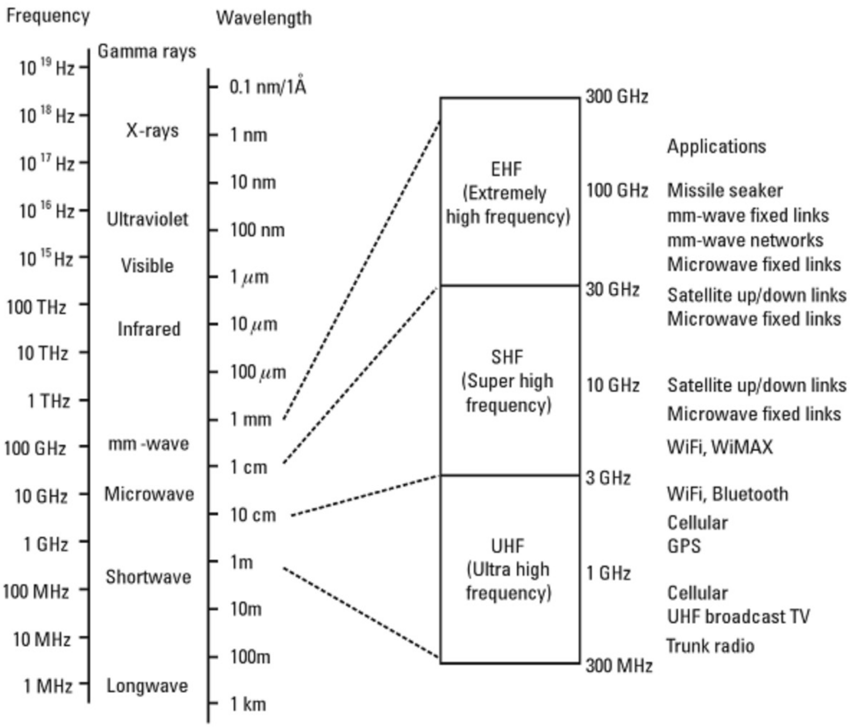

Figure 1.1: The RF, microwave and millimeter-wave range of frequencies [8].

tations [13–15]. The recent advancements in the millimeter wave active and passive technologies have created a unique opportunity to implement low-cost systems for existing and novel commercial applications in this area. Some examples are given as follows:

- **Short range wireless communication and networking:** There is a huge spectrum available in mmW/sub-mmW , and the antenna size is smaller than that of microwave counterpart which makes it possible for systems to be integrated on a single chip or in the chip package [16–19].
- **RADAR and transportation:** MmW/sub-mmW provides a larger bandwidth and higher spatial resolution as compared to those of microwave frequencies; low profile RADARs and car RADARs [20–22].
- **Astronomy:** Using ultra low noise systems with very large apertures at mmW [23, 24].
- **Bio-molecular sensing, medical and plasma diagnostics, biomedicine**

and DNA studies: Many biological macromolecules such as DNA rotation and vibration in the THz-band; these organisms have a unique response to the THz wave [25–28].

- **Security monitoring and non-destructive inspection (NDI):** MmW/sub-mmW can pass through many materials such as paper, cardboard, plastic, wood and textile. This capability allows for non-destructive and non-invasive inspection of, e.g. mails and packages in post offices, luggage and people at airports and security checkpoints and border crossings [29–32]
- **Environmental, space and atmospheric research:** MmW-sub-mmW/THz can be used to develop high resolution map of the universe. In addition, a large number of atmospheric molecules such as water, carbon monoxide, nitrogen, and oxygen can be detected in this spectrum. This can be used to assist in atmospheric environmental protection; the monitoring of the ozone layer, and environmental and geological studies [33–36].
- **Medical imaging and detection:** The transmission and reflection of THz radiation is much more sensitive to the materials it passes through as compared to those of microwave or infrared radiation. Furthermore, the photon energy is not harmful to live cells as opposed to X-ray radiation. It also provides a higher spatial resolution than that of microwave frequencies [37, 38].
- **Safety imaging systems:** Including fire control and prevention, vision through fire, all-weather vision and navigation.

  Millimeter wave systems, as compared to their lower frequency counterparts, can offer extreme communication bandwidth, much higher spatial resolution because of shorter wavelength, and remarkable ability to see through media that block infra-red and the visible spectrum [39, 40].

The challenges of using millimeter wave systems are high free space attenuation and scattering, high material loss (metal and dielectric), relatively low performance (higher noise, less gain and power output) of active devices, high cost of the active device technology and the integration of the active and passive parts of the system. To overcome these challenges, investigation, exploration and development of new active and passive technologies, topologies and integration techniques are required.

The nano-metric silicon technologies namely, the complementary metal oxide semiconductor (CMOS) and the silicon germanium (SiGe), are very promising for the mmW applications. The CMOS technology which is also available as a part of the SiGe technology has the ability to implement a very large number of transistors in a small chip area (highly integrated circuits). This is essential for the complex signal processing or performance tuning in the advanced radio front ends. At the same time, down scaling of the CMOS technology to nanometer scales have improved its RF performance parameters such as the maximum frequency of oscillation, unity current gain frequency and the minimum noise figure. SiGe with a lower device noise figure, higher power handling and frequency of operation provides superior RF performance to complement the CMOS as needed. These advantages make silicon technologies to be very attractive for high volume low cost emerging millimeter-wave markets [41, 42]

In this research, the focus is on the design and development of novel cost-effective integrated circuits and systems working within the range of millimeter wave with the emphasis on the passive imaging applications. Passive millimeter wave imaging systems are investigated and a new active Rotman lens architecture is proposed to establish a very high performance platform in the implementation of the millimeter wave integrated beam-scanning receivers.

To achieve the integration of on-chip amplifiers to implement the proposed active Rotman lens, an efficient and miniaturized Rotman lens is designed and fabricated. A new topology for implementation of miniaturized and wide-band millimeter wave low noise amplifiers using the low cost and highly integrable CMOS technology is presented. Theoretical and experimental aspect of these new technologies are explored.

1.2 Thesis Overview

In chapter 2, after a short review of low attenuation atmospheric frequency windows in the millimeter wave suitable for long range passive imaging and the most widely used radiometer architectures, system aspects of the proposed active Rotman lens architecture for passive millimeter wave imaging are presented.

In chapter 3, a novel Band Pass Distributed Amplifier (BPDA) topology is proposed to achieve realization of high performance and miniaturized low noise amplification in the millimeter wave using the cost-effective CMOS technology.

Chapter 4, presents a methodology to design low noise and stable BPDAs. Using this methodology and presented design formulas in chapter 3, various LNAs are designed and fabricated for different millimeter wave bands. A new amplifier figure of merit is defined to compare the performance of these amplifiers with the state of the art.

Designed and fabrication of a miniaturized, efficient, low profile and cost effective Rotman lens is presented in chapter 5.

Finally, chapter 6 explains the contributions and provides directions for possible future works.

1.3 Main Contributions

In summary, the main contributions of this work are:

- Proposed a high performance, cost effective active Rotman lens architecture for passive mmW imaging systems.
- Proposed a new band pass distributed amplifier topology for broad-band, high-gain and low-noise mmW amplification.
- Proposed a new design methods for simultaneously power and noise matching and highly stable mmW amplifiers using low-cost CMOS technology.
- Designed and fabricated a miniaturized, low noise 60 GHz amplifier with a measured figure of merit (FOM) of 51.
- Designed and fabricated an above f_T LNA with 10 dB gain at 85 GHz using a low-cost CMOS technology.
- Designed a multi-stage band pass DA with a simulated 20.5 dB flat gain from 38 to 68 GHz and with an excellent FOM of 514.
- Designed and fabricated a miniaturized mmW Rotman lens with a measured efficiency of %30.

Chapter 2

PASSIVE MILLIMETER WAVE IMAGING SYSTEMS: A TECHNOLOGY OVERVIEW

2.1 Introduction

In this chapter, after a short review of imaging system configurations, the advantages of passive mmW imaging systems are explained. Low attenuation atmospheric windows suitable for long range passive imaging are reviewed. The most widely used architectures for passive mmW imaging systems, the state-of-the-art mmW detector technologies key performance parameters are reviewed and compared.

The sensitivity performance of passive mmW imaging systems are still very limited [6, 43–51], due to the high path-loss, low quality of the active and passive components and the poor detector noise performance at mmW.

Active Rotman lens architectures is proposed as a unique solution to implement cost-effective integrated passive mmW imaging systems. In the proposed topology a Rotman lens is used due to its wide-band, wide-scan, simplicity (no separate beam control devices such as mechanical rotation of phase shifter are needed), and low fabrication cost.

The proposed system architectures is analyzed and its performance is compared with the state of the art. The trade-off between important design parameters is studied and shown that implementing high gain LNAs relaxes its noise figure as well as the detector performance requirements. It is shown that it is quite beneficial to implement the system using the cost-effective CMOS technology, despite its higher noise figure as compared to more complex and expensive III-V technologies.

2.2 Passive MmW Imaging Systems

An image is created form a scene or a target area by measuring and analyzing the emission radiated from the scene considering the reflection and transmission properties of materials in the target area. Imagers or generally speaking, sensor systems are categorized based on 1) the distance of the object to the sensor, 2) the transmitter architecture and 3) the receiver architecture. When the target is located close to the sensor, the system is called a pointing sensor or near field imager. In this case, the transmitter or source can be coherent such as in a network analyzer based near-field scanner or incoherent such as in a Fourier transform spectrometer. On the other hand, when there is a large distance between the target and the sensor, only an extremely small part of the radiated emission can be effectively received by the system and the system is called a remote sensor or far field imager. If the system transmits power to the object and detects the reflected power, the system is active like RADAR (RAdio Detection and Ranging). If the system does not transmit signal and the incoherent radiation from surrounding environment illuminates the object, the system is called a passive imager or radiometer. While active systems spend a large amount of energy to illuminate the target area, passive imaging systems produce image from their natural emissions [6].

Table 2.1 shows categories and examples of different sensor types in the mmW and THz regions.

The medium separating the imager from the target also plays an important role in the signal level that reaches the imager. A highly attenuative medium can cause the signal which arrives at the imager to be too low to be detectable. In a clear weather, objects are easily detectable in the presence of the sunlight which is being reflected by the objects in the optical range. At night, objects can be detected by an infra-red camera. However, the atmospheric constrains such as fog, heavy rain or snow can highly attenuate the received signal by scattering or absorption of optical or infra-red wavelengths.

Table 2.1: Different sensor categories for the millimeter-wave and THz regions [6].

Distance	Remote senor (far field imaging)		Pointing senor (near field imaging)		
Transmitter exists?	No	Yes	No	Yes	
Receiver	Incoherent	Coherent	Incoherent	Incoherent	Coherent
Example	Radiometer	RADAR	-	Fourier transform spectrometer	Network analyzer

Passive mmW imaging uses radiometers to detect the thermal radiation radiated by objects. Over the entire mmW range of frequency, there are a few low attenuation atmospheric windows suitable for long range passive mmW imaging as shown in Figure 2.1. Among these windows, the lower end of the mmW region which covers frequencies from 30 to 45 GHz provides very low attenuation [maximum 2 dB/km in 5 mm/hr rain fall rate as can be seen in Figure 2.1 (b)] in the presence of different atmospheric constrains. However, it has a limited imaging resolution due to its long wavelength. Also, the system will require a large aperture; therefore, it is not suited for many imaging applications.

On the other extreme, high end mmW region which cover frequencies from 190 to 300 GHz, provide a larger imaging window of 110 GHz and due to its shorter wave length, a better imaging resolution is possible while a small aperture size is required. However, there is a lack of the required low-cost technologies to amplify the attenuated signal. The amplification is available by complex and very expensive III-V based technologies; therefore, currently the implementation of a low-cost passive mmW imaging system is not possible. Also, the signal is highly scattered in foggy condition [up to 10 dB/km loss as can be seen in Figure 2.1 (a)] compared to that in the lower frequencies.

In the 65-110 GHz frequency window, a large window of 45 GHz is available and the signal attenuation is moderate (maximum 2 dB/km in fog or light rain and higher in the medium and heavy rain). Also, the wavelength is relatively short; therefore, an acceptable image resolution is available while a small aperture size is adequate to implement the system over this range of frequencies. Finally, the nanometer scale CMOS technology can provide a low-cost solution for implementa-

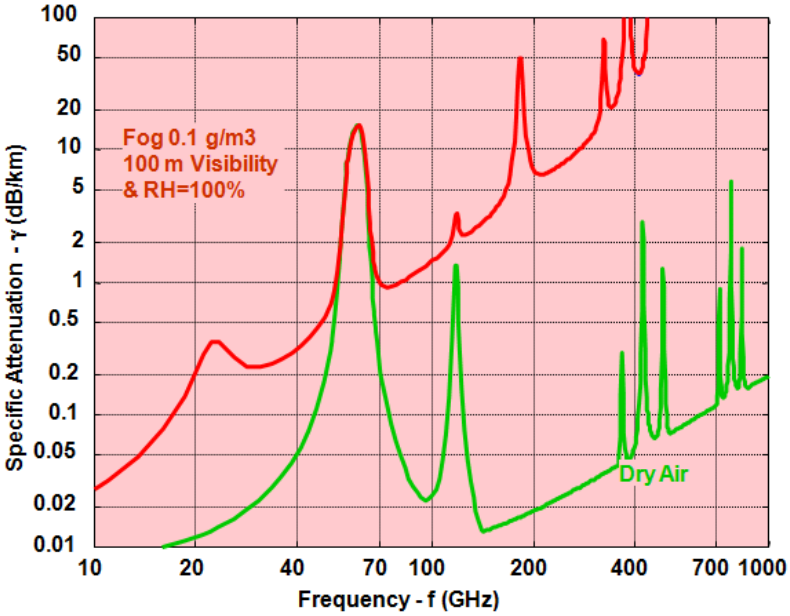

(a)

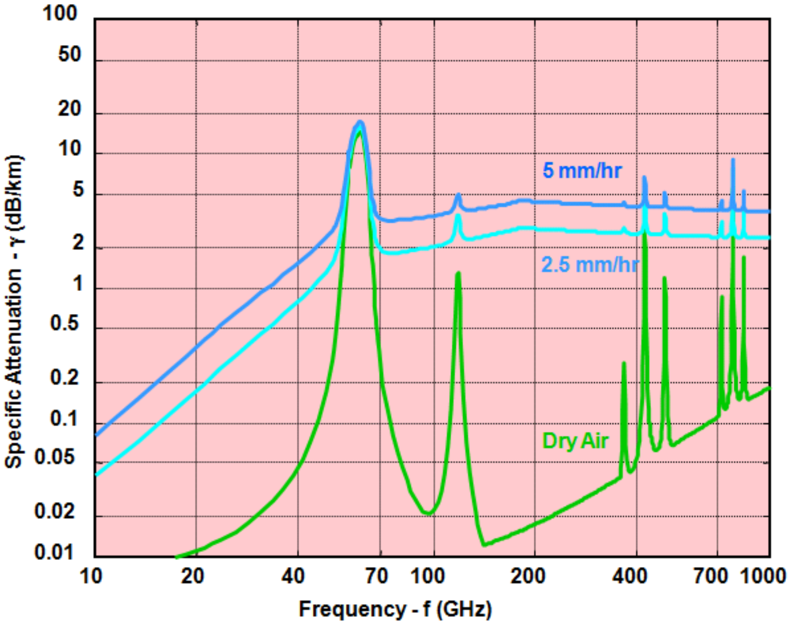

(b)

Figure 2.1: Specific atmospheric attenuation in the dry air and in the presence of the atmospheric constrains: (a) Fog (0.1 gr/m3, 100 m visibility and 100% relative humidity) and (b)Light (2.5 mm/hr) and medium rain (5 mm/hr). [9]

tion of a passive mmW imaging system. This means that although the loss is higher than that of the microwave frequency, it can be tolerated due to the advantage of the system from the aperture size and imaging resolution point of view. Therefore, this band is the main focus of this work.

It is to be emphasized that the proposed active lens concept can readily be extended to higher mmW and sub-mmW bands as active technologies become mature and available in these range of frequencies.

2.2.1 Basic radiometer architecture

Two basic radiometer architectures are known as heterodyne and direct detection and shown in Figure 2.2. The incoming emission from the object is detected by an antenna and feeds an LNA , which amplifies the received signal above the noise level of the system. In both architectures, LNA can be omitted; however, this will limit the sensitivity of the system due to the noise generated in each block of the system. Especially in the direct detection architecture, the receiver sensitivity will be limited by the antenna loss and the detector noise.

The situation is different in the heterodyne receiver as a strong local oscillator can improve the receiver sensitivity. The signal is down-converted to an Intermediate Frequency (IF) by a mixer. The weak signal is advantageous for mixing which allows linear mixing operation. Therefore, the pass-band can be defined by the IF which is much lower in cost and much higher in performance as compared with RF filtering or amplification. In both architectures, a peak detector detects the low frequency signal which is amplified by a low frequency amplifier to drive an integrator. The analog output is proportional to the image contrast and can be converted into a digital signal for further processing.

The advantage of the direct detection system over the heterodyne receiver, is its simplicity as there is no need for mmW local oscillator and mixer. This makes the direct detection architecture low cost, simpler, and ultimately much smaller in size, which is one of the main objectives in this thesis. Therefore, the direct detection architecture is selected for the purpose of this research.

The detector is among the important component of a passive mmW imaging system. Different types of detectors have been used for mmW imaging systems.

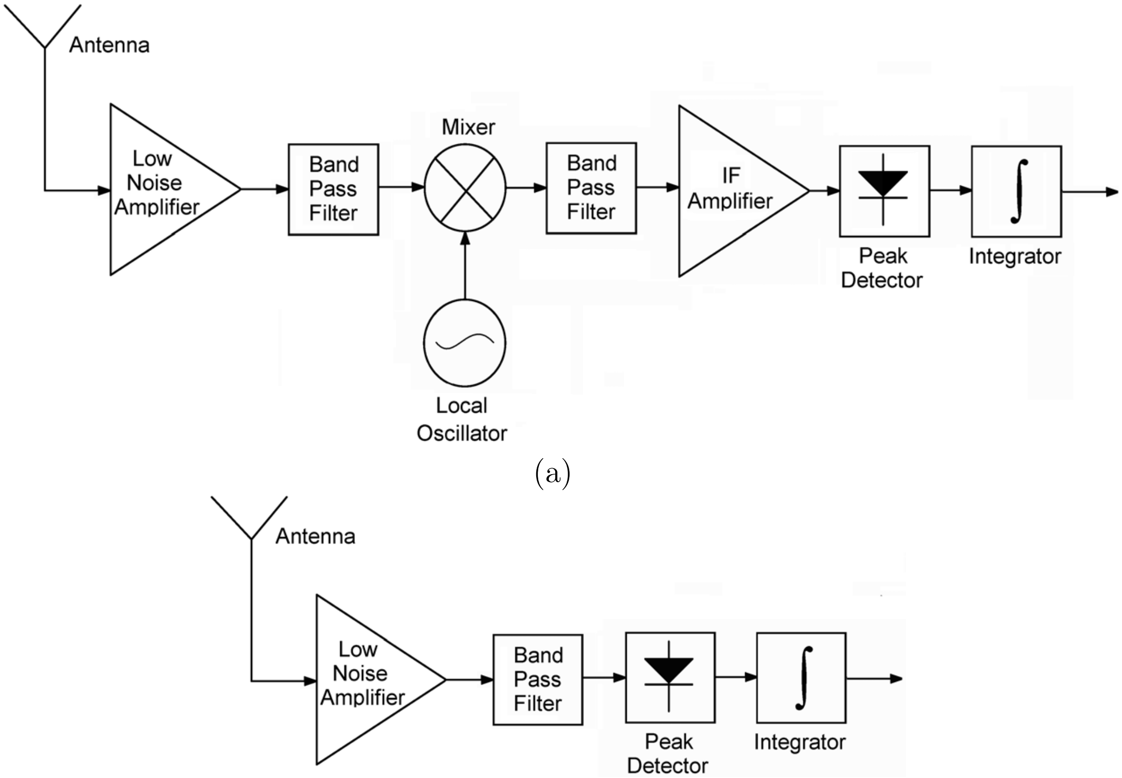

(a)

(b)

Figure 2.2: Two main architectures for passive millimeter wave imaging systems: (a) Heterodyne and (b) Direct detection.

Zero-bias Schottky diodes [52], tunnel diodes [44], hetro-structure backward diodes [53], transistor circuits [45, 46], bolometers [47] and Golays are some examples.

The responsivity ($\mathcal{R}$) of a detector is the main Figure Of Merit (FOM) of an imaging detector. This is the ratio of the output signal voltage (usually DC) of a detector to its absorbed input power (RMS value of the main component). Therefore, the unit of responsivity is (V/W) and it is expressed as [6]:

$$\mathcal{R} = \frac{V_{out}^{DC}}{P_{in}^{RF}} \tag{2.1}$$

The Noise Equivalent Power (NEP) is another FOM for an imaging detector which is by definition the input signal power at the detector required to achieve a post detector SNR of unity. By dividing out the post bandwidth effect, the normalized NEP is in unit of W/$\sqrt{\text{Hz}}$ and it is related to the detector responsivity and detector noise voltage by the following formula [6]:

$$NEP = \frac{v_n}{\mathcal{R}} = \frac{v_n}{V_{out}^{DC}} P_{in}^{RF} \tag{2.2}$$

where v_n is the detector output noise voltage. Reported CMOS detectors provide low performance (NEP=200 pW/$\sqrt{}$Hz and $\mathcal{R}$ =200 V/W) as compared to that of the high performance detector technologies (NEP<1 pW/$\sqrt{}$Hz and R>1 KV/W). However, these technologies are often incompatible with each other and multiple dies should be used to implement the imager which increases the complexity and the cost of the system. A miniature detector circuit with low noise (NEP=3 pW/$\sqrt{}$Hz and R=12 KV/W) has been recently reported using the SiGe technology [45] which is low cost and compatible with the low cost CMOS technology.

Sensitivity for radiometric and thermal imaging systems is expressed in terms of the change of the temperature of a thermal source that produces post detection SNR of unity. The resulted FOM is the Noise Equivalent Difference Temperature ($NEDT$) which is the most useful measure of the thermal radiometers performance and is given by [6]:

$$NEDT = \Delta T_M = \frac{NEP}{dP_{in}^{RF}/dT} \tag{2.3}$$

where the denominator is the change of input power which is defined on terms of temperature T in Kelvin as:

$$P_{in}^{RF} = k_B T B \tag{2.4}$$

In (2.4), B and k_B are the imager bandwidth and the Boltzman constant, respectively.

Considering pre-detector attenuation, β, and post detector integration time, τ, and using equation (2.3), one can rewrite the equation (2.4) to give the imaging $NEDT$ of a passive direct detection radiometer without an LNA [43]. That is:

$$NEDT = \frac{NEP}{\beta k_B B \sqrt{2\tau}} \tag{2.5}$$

For a practical mmW imaging system an $NEDT$ of less than 1 K is required which is not achievable in room temperature for any detector. Therefore, a high gain LNA is a requirement for that imager. In this case the noise temperature of the receiver is mainly determined by the noise of the LNA which can be much lower than that of the detector noise. In the presence of an LNA, the radiometer sensitivity is given at [45]:

$$NEDT = \sqrt{\left[\frac{2T_S^2}{B} + \left(\frac{NEP}{\beta k_B G B}\right)^2\right]\frac{1}{2\tau}} \tag{2.6}$$

where T_S and G are system noise temperature and LNA power gain, respectively.

For a radiometer with typical NEP=5 pW/$\sqrt{}$Hz, Ts=2300 K, B=15 GHz, β=0.7 and τ=33 ms; an LNA with a 25 dB gain and 7 dB noise figure will be required to achieve an $NEDT$=0.5 K. It should be noted that the system temperature, T_S, is determined by the noise figure of the LNA and the other pre-LNA noise sources.

For a radiometer implementing an LNA, the output power from LNA is $P_{in}^{RF} = Gk_BTB$. Therefore, any changes in the gain of amplifier will result in a change in the temperature and produce a false signal. Hence, the LNA should have a very stable gain and a low 1/f noise for a precise radiometer. In the presence of the LNA gain variation (ΔG), the minimum resolvable temperature for a radiometer is given by [54]:

$$NEDT = T_S\sqrt{\frac{1}{B\tau} + \left(\frac{\Delta G}{G}\right)^2} \tag{2.7}$$

For a typical radiometer with the above mentioned specifications, to have the $NEDT$=0.5 K, $\Delta G/G$ should be less than 0.0002 which is difficult to achieve in practice.

The impact of the 1/f noise and low-frequency gain variations can be eliminated, or at least greatly reduced, by periodically calibrating the radiometer using a Dicke-type radiometer architecture which will be described in the next section [43].

So far, the sensitivity of no un-cooled solid-state mmW detector is sufficient to directly measure terrestrial scene brightness temperatures for video-rate thermal imaging. However, there exist semiconductor detectors with sufficient sensitivity levels such that a single mmW monolithic integrated circuit (MIMIC) amplifier chip can provide the power level required for video-rate imaging. The comparison of mmW detector performance using different technologies and the gain required to achieve a $NEDT$ of 0.4 K for each detector are shown in Table 2.2.

Table 2.2: The performance comparison of reported mmW detectors and the required LNA gain to achieve 0.4 K $NEDT$ for a typical mmW imaging systems with β=0.6, B=15 GHz, NF_{LNA}=8 dB using equation 2.6.

Technology /Material	Topology /Device	freq. (GHz)	$\mathcal{R}$ (V/W)	NEP (pW/$\sqrt{}$Hz)	Req. LNA gain (dB)	Size (mm^2)	Ref.
CMOS 65 nm	On-chip Schottky diode	88	180	200	42.5	0.02	[43]
ErAs / InAlGaAs	Zero-bias Schottky diode	94	4500	0.4	15	-	[52]
InAs AlSb GaSb	Backward tunnel diode	87	11K	-	-	-	[44]
InAs AlSb GaSb	Backward tunnel diode	50	3650	4.2	25.5	-	[53]
SiGe 0.18 μm	Common emitter circuit	94	12K	3-4	25	0.06	[45]
CMOS 0.25 μm	Diffrential CS NMOS	650	150	300	44	-	[45, 46]
VO_2 NiCr Si_3N_4	HTSC micro bolometer	95@ T= 90 K	7500	0.23	13	-	[47]

As seen from Table 2.2, by increasing the detector NEP, an LNA with a higher gain is required to achieve the $NEDT$=0.4 K. Also, from this table, it is seen that CMOS detectors using either the Schottky diode or the transistor based circuit have very poor NEP, making them inappropriate for high sensitivity passive mmW imaging systems. On the other hand, low-cost SiGe detectors can be implemented with very low NEP and can be easily implemented in a CMOS chips.

2.2.2 The Dicke-Type radiometer architecture

The Dicke-type radiometer architecture is shown in Figure 2.3.

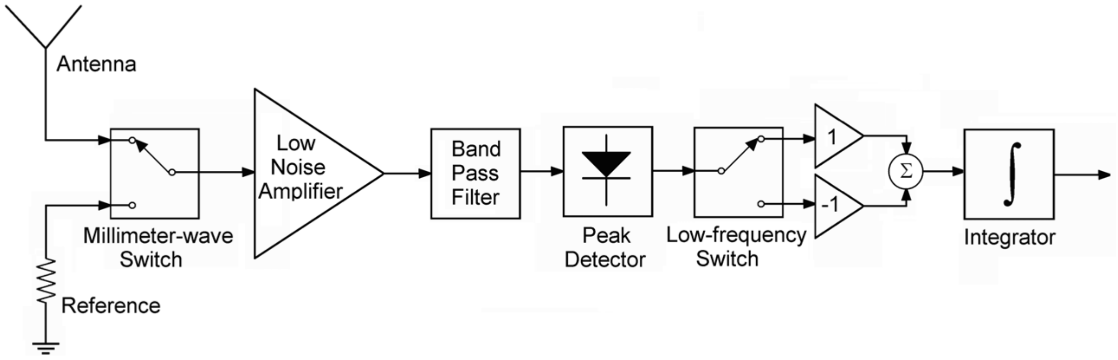

Figure 2.3: Block diagram of a Dicke-type radiometer.

The input of the receiver is switched between the antenna and a reference load which represents a calibrating temperature with a certain frequency. The switching frequency should be much higher than the 1/f corner frequency of the radiometer such that the gain variation is negligible during each cycle. In order to synchronize with the antenna switch, a multiplier switch placed after the detector.

As seen from Figure 2.3, the output of the detector is multiplied by +1 or -1 when the receiver input is connected to the antenna or the reference feed, respectively. Therefore, the detector output voltage corresponding to the reference temperature is subtracted from the received signal from the antenna.

Using this arrangement, the fluctuation in the LNA gain is effectively reduced. The measurement is performed only during the switching half-period. This results in the $NEDT$ to increase by a factor of 2. This is the main drawback of Dicke switch radiometers.

The $NEDT$ of this radiometer can be expressed by [43]:

$$NEDT = \frac{1}{\beta}\sqrt{\left\{\frac{2\left[\beta T_A + (F_{LNA}-\alpha)T_0\right]^2}{B} + \Big(\frac{NEP}{KG_{LNA}B}\Big)^2\right\} B_{LF}} \tag{2.8}$$

where β, T_A , T_0 and F_{LNA} are the pre-LNA attenuation factor, antenna temperature, ambient temperature and LNA noise factor respectively. The other critical component is the single pole double throw (SPDT) switch at the input of the receiver which should operate in the mmW frequency which is not easy to implement. The switch also introduces a considerable amount of loss which deteriorates the radiometer performance by decreasing the pre-LNA attenuation, β, as seen in equation 2.8.

2.3 Active Rotman Lens Architecture for Passive MmW Imaging Systems

2.3.1 An overview of radiometer based imaging systems

The radiometer architectures described in the previous section are known as single pixel radiometers as the beam coming from a pointed direction is converted to a signal which represents that specific part of the scene or target area. In order to create the image from the whole scene, the scanning of the whole area is required to relate each area of the scene to a pixel in the image. This can be achieved by varying the antenna main beam direction using mechanical, optical or electronic scanning techniques.

In this section, a brief overview of a few imaging system architectures implemented using various methods is presented.

Using a single pixel radiometer and mechanical scanning the antenna beam in two dimensions requires the simplest electronics. However, the mechanical structure which is required to perform an accurate scan makes the system complex and bulky. It also requires considerable time to capture the image depending on the number of pixels. Also, the scanning time for each pixel is limited to the mechanical pause time at each step which is related to the integration time which limits the sensitivity of the system.

An opto-mechanically scanning mmW imager which is intended to monitor the ground movement of aircraft in adverse weather conditions is described in [50]. It employs two counter-rotating mirrors that are tilted about their axes of rotation which scan the whole target area in a 60° by 20° field of view. A high speed vertical scanner moves the antenna through 20° and a low speed flapping mirror scans the beam horizontally through 60°. A single channel 94 GHz receiver consisting of an InP LNA followed by a down-converter and a detector is used as the radiometer for this imager. The video output is passed to an A/D converter and displayed on a conventional personal computer. This system has a spatial resolution of 0.5° and a thermal sensitivity of 2 K.

Another method to scan the whole target area is to use one radiometer for each pixel which removes the opto-mechanical structures and increases the imager speed by eliminating the need for the scanning mechanism. However, this solution requires a large number of radiometers which is not cost effective and difficult to realize in mmW. For example, to have a few thousand pixels; at the present cost of several hundred dollars per image pixel, the cost of the whole system exceeds a million dollars. Also, the system will be bulky and difficult to implement [51].

Linear array of antennas allows for the scanning of one dimension in the range of its scan angle. So scanning of this array is required only in the dimension orthogonal to it in order to measure the whole scene. This can be done by frequency scanning of each antenna element; therefore, there is no need for any focusing objects or moving parts. Also, implementing proper beam forming architecture allows the reduction in the number of receiver chains in the front end which further reduces the cost and complexity of the system.

2.3.2 Active Rotman lens architecture

Fig. 2.4 shows the proposed active Rotman lens architecture and its conventional counterpart using an m by n Rotman lens. In the conventional configuration which is shown in Fig. 2.4 (a), the incoming radiation is received by n antennas and is transferred to each array port using n piece of transmission lines. The delay provided by each line along with the appropriate lens design causes the power to be combined constructively at corresponding beam ports depending on the direction of the incoming radiation.

The m output ports of the lens are connected to an m by 1 SPmT (Single Pole m Through) switch. These switches are quite inefficient and difficult to implement in MMIC technology. The loss at this stage is directly added to the noise of the system and degrades the signal to noise ratio. In addition, due to the sequential nature of the scanning process, the integration time is reduced by an order of n for

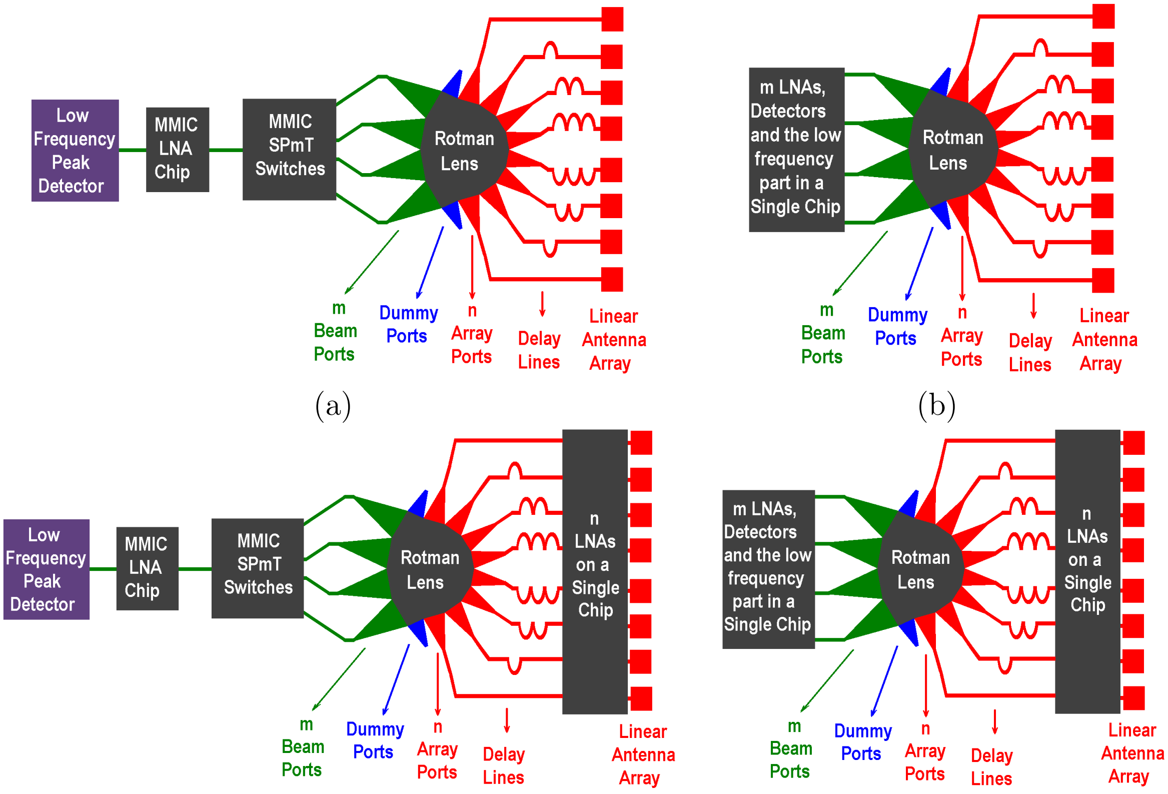

(a) (b)

(c) (d)

Figure 2.4: m by n active Rotman lens architectures. a) conventional configuration [96] and proposed configurations using b) post lens LNAs c) pre lens LNAs and d) both pre and post lens LNAs.

each pixel of the image, which directly degrades the imager sensitivity. Moreover, the switch may reduce the effective band width of the system.

In order to scan each beam port and cover the total field of view, the m output ports of the lens are connected to an m by 1 SP2mT switch in order to scan each beam port and cover the total field of view. These switches are quite inefficient and difficult to implement in MMIC technology.

Following the switch, an LNA amplifies the signal to a level higher than that of the system noise. It should be noted that, due to the passive and lossy nature of the antennas, transmission lines, lens and switch, the SNR is poor, and therefore, this architecture has a limited sensitivity.

In the proposed active lens architecture shown in Fig. 2.4 (b), m LNAs are placed after the beam ports, there is no need to use an inefficient switch. In addition, the elimination of the switch allows a parallel transfer of signals to the detectors which increases the radiometer integration time. Therefore, this configuration achieves a much better SNR as well as an enhanced band-width as we will see in section 2.3.5.

Fig. 2.4 (c) shows another method to increase the sensitivity of the system. In this configuration, n LNAs are inserted before the lens to compensate the loss of the lens. However, this configuration has many complexities such as the need for proper transition between each element in the front end and compensations for variations between LNAs.

Finally, Fig. 2.4 (d) shows an alternative configuration where, m+n LNAs are implemented in both the input and output of the lens to further improve the performance of imager. However, this method considerably increases the complexity, power consumption, total chip area and therefore the fabrication cost of the system.

2.3.3 General noise analysis

For an active array, it is important to study its system temperature and overall noise figure. Therefore, a general noise analysis is presented in this section in order to analyze and compare the performance of the above mentioned configurations. In all of these configurations, the input noise power injected into the detector is sum of the detected thermal radiation of the object and the system's noise power. For noise analysis of a single pixel radiometers, the well known Friis's formula [97] can be used:

$$F = F_1 + \frac{F_2 - 1}{G_1} + ... + \frac{F_N - 1}{G_1 G_2 ... G_{N-1}} \tag{2.9}$$

where F is the overall noise figure of the system, F_i is the noise figure of the gain block i and G_i is its gain. If a block is passive, F_i and G_i should be replaced with L_i and $1/L_i$ where L_i is the insertion loss of the passive block, respectively. However, this formula cannot be directly applied to a system with n input by m output.

Fig. 2.5 shows a simplified block diagram of an active Rotman lens configuration which can represent any architectures shown in Fig. 2.4. The system consists of identical antennas which are connected to the LNAs on each channel using identical interconnection and have a noise temperature of TA. In this figure, L_1 represent the total pre-LNA loss, including the antenna loss and its interconnection loss to the

LNA. The loss of each lens path from an array port to a beam port is shown as L_2 and the loss associated with connections from lens to post-lens LNAs, is represented by L_3. Finally, L_4 represents signal loss between the post-LNAs and the next stage which is a detector. It is obvious that, depending on the architecture, each of these losses consist of different components.

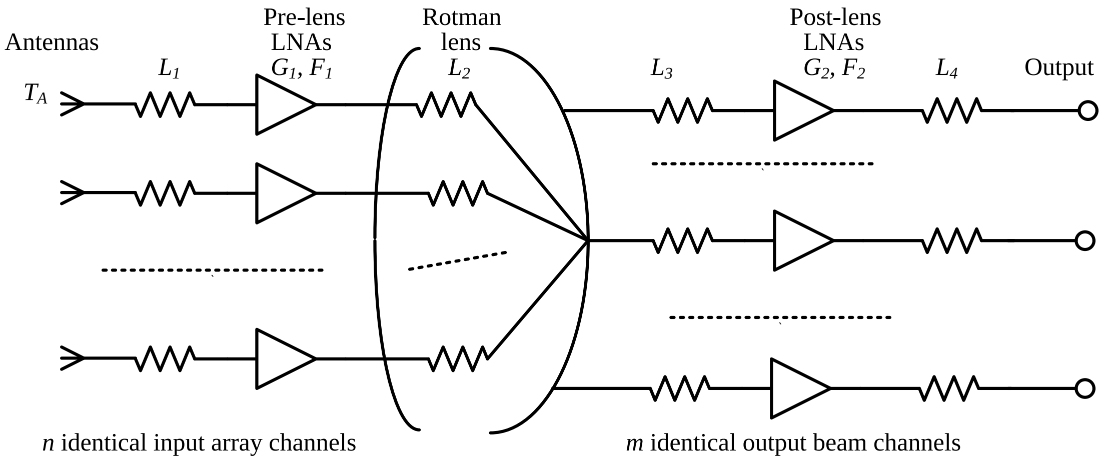

Figure 2.5: Simplified block diagram of a m by n active Rotman lens configuration.

For simplicity, we assume that each of these losses are equal on each channel and input and output impedances are $50\,\Omega$ for all blocks. The pre-lens and post-lens LNAs are characterized by power gains with a magnitude of G_1 and G_2 and noise figures of F_1 and F_2 , respectively. Assuming that the signal powers delivered to the array ports are equal and all antennas have the same noise power, the overall noise figure of the system, F, can be obtained similar to the noise analysis presented in [98]-[99]:

$$F = L_1F_1 - \frac{L_1}{G_1} + \frac{L_1L_2}{G_1} + \frac{F_2L_1L_2L_3}{G_1n} + \frac{L_1L_2L_3L_4}{G_1G_2n} \tag{2.10}$$

From equation 2.10, it is seen that, the term L_1F_1 is the dominant term, if G_1 is large enough. However, if G_1 is not large enough (i.e. in the absence of the pre-lens LNAs where G_1=1), all other loss components contribute to the overall noise figure of the system and degrades the sensitivity of the system.

The resulted system noise figure can be converted to the system noise temperature, T_S, as follows:

$$T_S = T_A + (F-1)T_0 \tag{2.11}$$

where T_A and T_0 are antenna and ambient temperatures, respectively.

The total gain of the system, G, before the detector, can be expressed as:

$$G = \frac{G_1 G_2 n}{L_1 L_2 L_3} \tag{2.12}$$

2.3.4 Radiometer sensitivity analysis

Equation (2.6) from chapter 2 will be used for radiometer sensitivity analysis [45]:

$$NEDT = \sqrt{\left[\frac{2T_S^2}{B} + \left(\frac{NEP}{\alpha k_B G B}\right)^2\right]\frac{1}{2\tau}} \tag{2.13}$$

where Ts, B, NEP, k_B, τ and G are system noise temperature RF band width, detector noise equivalent power, Boltzman constant, integration time and overall system gain, respectively. In equation (2.13), it is seen that the sensitivity can be increased by increasing its RF band width and integration time. From 2.13, it is seen that, the $NEDT$ has two terms: the first term is related to system noise temperature and the second term is related to the detector sensitivity and total system gain. Therefore, two extreme cases can be considered as follows:

1. Extremely low noise detector and high system noise figure: In this case, the imager sensitivity is directly proportional to the system noise temperature:

$$NEDT_{LowNEP} = T_S\sqrt{\frac{1}{B\tau}} \tag{2.14}$$

2. Extremely low noise system and noisy detector. In this case, the imager sensitivity is directly proportional to the detector NEP and inversely proportional to the total system gain:

$$NEDT_{LowNoiseSystem} = \frac{NEP}{K_B G B}\sqrt{\frac{1}{\tau}} \tag{2.15}$$

Usually, in practice, both terms are important, and therefore the low noise and high gain system as well as the low noise detector are the main requirements for a highly sensitive imager. In the next section, a practical example will be explained to compare the performance of the presented active lens configurations.

2.3.5 Performance comparison of active Rotman lens architectures

Using the system analysis presented in the previous sections, the performance of active Rotman lens architectures can be derived in terms of its building block parameters. The parameters for a typical system are approximated for each configuration and are summarized in Table 2.3.

Table 2.3: Typical building block parameters for active Rotman lens (RL) architectures shown in Fig. 2.4.

Components	Architecture Parameter	Conventional Fig. 2.4 (a)	Proposed Fig. 2.4 (b)	Proposed Fig. 2.4 (c)	Proposed Fig. 2.4 (d)
Antenna loss	L_1	0.5 dB	0.5 dB	1 dB	1 dB
Pre-lens	G_1	0 dB	0 dB	20 dB	10 dB
LNAs	F_1	1	1	4	4
RL loss	L_2	9 dB	9 dB	10 dB	10 dB
Post lens IL	L_3	6 dB	1 dB	4 dB	1 dB
Post lens	G_2	20 dB	20 dB	0 dB	0 dB
LNAs	F_2	4	4	1	4
post LNA IL	L_2	16 dB	16 dB	16 dB	16 dB

For each architecture, the overall gain, noise figure, system noise temperature and the resulted imager sensitivity are calculated and shown in Table 2.4.

As seen from Table 2.4, for the given building block parameters, proposed imagers shown in Fig. 2.4 (b) and (d) provide a superior performance compared to their conventional counterpart of (a). However, considerable complexity and cost associated with case (d) makes case (b) to be the preferred architecture. Using this

Table 2.4: Resulted imager sensitivity for architectures shown in Fig. 2.4.

Components	Architecture Parameter	Conventional Fig. 2.4 (a)	Proposed Fig. 2.4 (b)	Proposed Fig. 2.4 (c)	Proposed Fig. 2.4 (d)
Overall	G for n=4	9	29	7	20
system gain	G for n=8	12	36	9	25
Overall noise	NF for n=4	16.4 dB	13 dB	7.3 dB	8.9 dB
figure in dB	NF for n=8	16.2 dB	13.5 dB	7.3 dB	9.1 dB
Imager	$NEDT$	14.2 K	2.37 K	15.9 K	2.94 K
sensitivity	$NEDT$	11.6 K	2.03 K	12.6 K	2.37 K

system analysis, case (c) has no advantage over the conventional case (a), given this building block parameters.

Fig. 2.6 shows resulted sensitivity of each imager as a function of the detector performance, NEP for typical imager parameters.

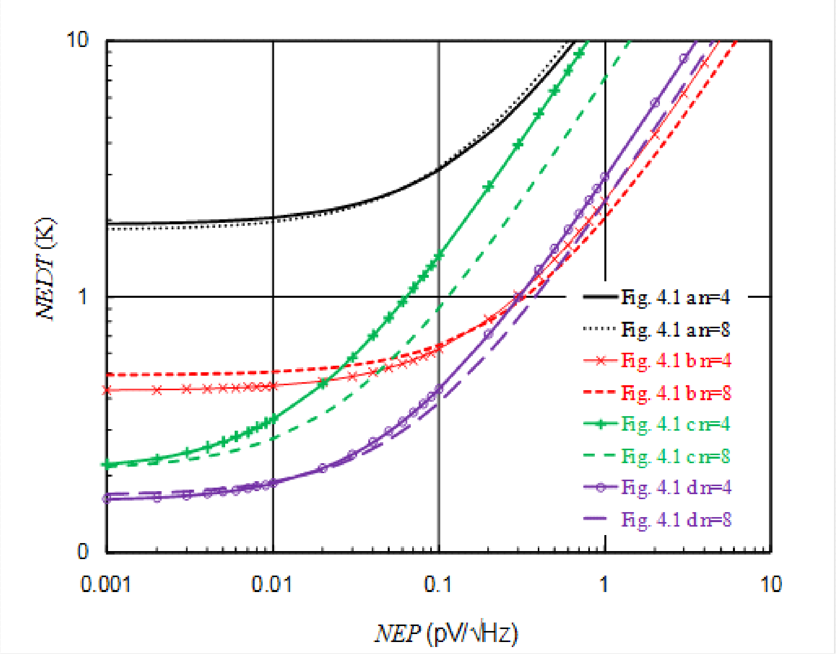

Figure 2.6: Resulted sensitivity of each imager architecture of Fig. 2.4 as a function of its detector performance, NEP, for typical imager parameters.

As can be seen from this figure, the architecture selection is highly related to the detector performance. For extremely low noise detectors ($NEP < 0.01$ pW/$\sqrt{Hz}$), the architecture of Fig. 2.4 (c) and (d) provided the best sensitivities. On the other hand, all the reported on-chip silicon detector have $NEP > 3$ pW/$\sqrt{Hz}$ (see Table 2.2), and in this case, the architecture (b) provides the best sensitivity.

2.3.6 High gain LNA requirement for active Rotman lens architectures

Fig. 2.7 shows LNA gain and NF requirements for the active Rotman lens architecture shown in Fig. 2.4 (b) as a function of its detector performance, NEP.

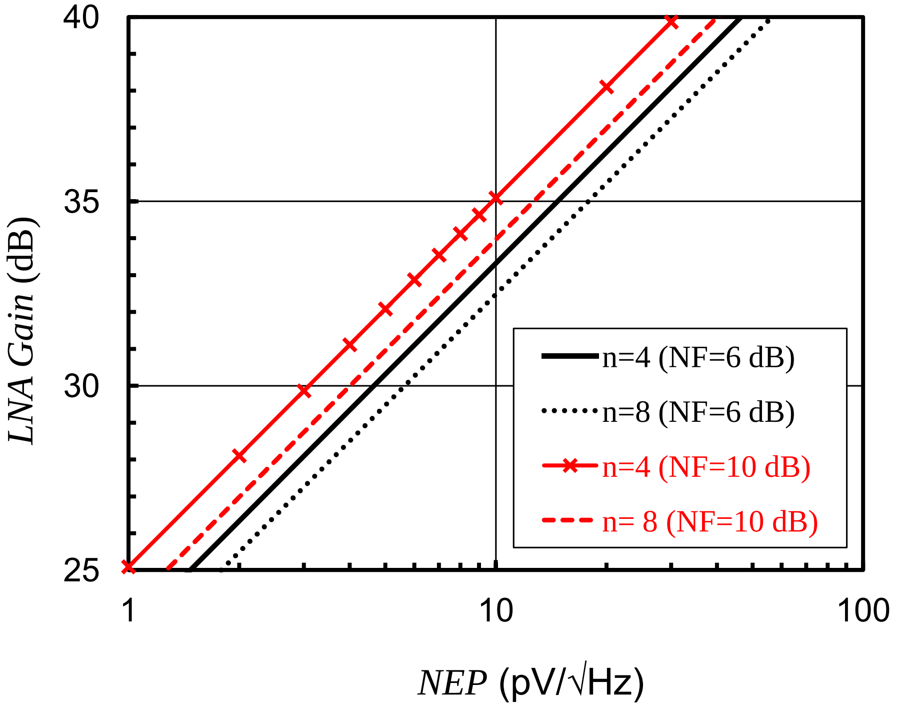

Figure 2.7: LNA gain and NF requirements for the active Rotman lens architecture shown in Fig. 2.4 (b) as a function of its detector performance, NEP.

As seen from this figure, for a more sensitive detector, the LNA requirement is relaxed, for this architecture. Also another important observation is that, the LNA noise figure requirement can be relaxed using a higher gain LNA. This suggests that the detector NEP and LNA noise figure requirement can be relaxed when a high gain LNA is used.

2.4 Conclusion

In this chapter, the state-of-the-art passive imaging systems in the mmW is presented. Low attenuation atmospheric windows suitable for long range passive imaging, basic radiometer architecture and the key performance parameters in the radiometer design are reviewed.

A new active Rotman lens architectures implementing a Rotman lens whose performance is boosted with many LNAs integrated on a single chip is introduced. The new architecture has a few advantages over the other existing solutions and can be used for future mmW imaging, RADAR and radio systems.

The proposed architecture combines the true time delay, wide scan angle and wide band advantages of a Rotman lens with the high integration capability of the silicon technology to provide a cost effective solution for a high performance mmW beam scanning receiver.

The sensitivity of the proposed architectures is performed and compared with conventional configuration. The trade-off between important design parameters are studied and it is shown that implementing high gain LNAs in this architecture, relaxes its noise figure as well as the detector performance requirements. This is quite beneficial to integrate the system using the cost effective silicon technology. It is concluded that for a poor detector performance of NEP=100 or $10\,pW/\sqrt{Hz}$ available in the COMS or SiGe technologies, an LNA with 50 or 35 dB gain will be required, respectively, with a 10 dB noise figure.

Chapter 3

A NEW BAND PASS DISTRIBUTED AMPLIFIER TOPOLOGY: THEORY AND DESIGN

3.1 Introduction

To amplify the weak signal above the system noise level, a high gain LNA is a key requirement for any receiver. Conventionally, expensive III-VI low noise devices are used to amplify the signal at mmW. Recently, the advancement of the silicon technologies have provided an opportunity to implement the whole front-end in a single low cost chip. Current amplifier topologies are not able to provide wide-band, low noise and high gain requirements for the passive mmW imaging systems.

In this chapter, a novel Band Pass Distributed Amplifier (BPDA) topology is proposed to realize high performance and miniaturized integrated circuits in the mmW using the cost effective CMOS technology. The conventional Distributed Amplifier (CDA) and the conventional BPDA using the low-pass to band pass transformation are first reviewed. Then, the frequency response and design formulas for a single stage DA are obtained by the lumped element and the transmission line models.

It is shown that the transfer function and the designed formula are only accurate up to a certain frequency range. For frequencies beyond this range, the transfer function is obtained by the transmission line model. A 2nd order approximation has been made in order to derive the design formula and it is shown that this approximation is valid at mmW.

The input and output reflection coefficients have been calculated for the BPDA topology and it is shown that by proper optimization technique, the input and output matching can be achieved at the required band. Finally, as the transistors show a bi-lateral behavior at mmW, the stability of the amplifier is studied. It is shown that if the amplifier is not unconditionally stable, the stability can be achieved by inserting a small degenerative source inductor.

3.2 Distributed Amplifier (DA)

3.2.1 Conventional Distributed Amplifier (CDA)

The distributed amplifier (DA) or traveling wave amplifier (TWA) has been widely and successfully investigated and implemented for the last six decades in various applications for both hybrid and monolithic technologies [55–80].

By providing a low pass frequency response, DAs, have found many applications in the microwave and mmW systems due to their ultra-broad band response, flat gain and group delay. The inherent high gain-bandwidth product is a result of the high cutoff frequency of the artificial transmission lines implemented in the amplifier topology and also its additive gain property. However they suffer from a low gain, high power consumption and large chip area [61]. Fig. 3.1 shows the schematic of a conventional distributed amplifier (CDA).

By properly choosing the gate and drain inductors, one can choose these parameters such that they satisfy [57]:

$$\sqrt{\frac{L_g}{C_{gs}}} = \sqrt{\frac{L_d}{C_{ds} + C_a}} = Z_0 \tag{3.1}$$

where Z_0 is the transmission line characteristic impedance, C_{gs} and C_{ds} are the gate-to-source and drain-to-source capacitors and C_a is the shunt capacitor connected to the drain of each transistor to synchronize the gate and drain transmission lines.

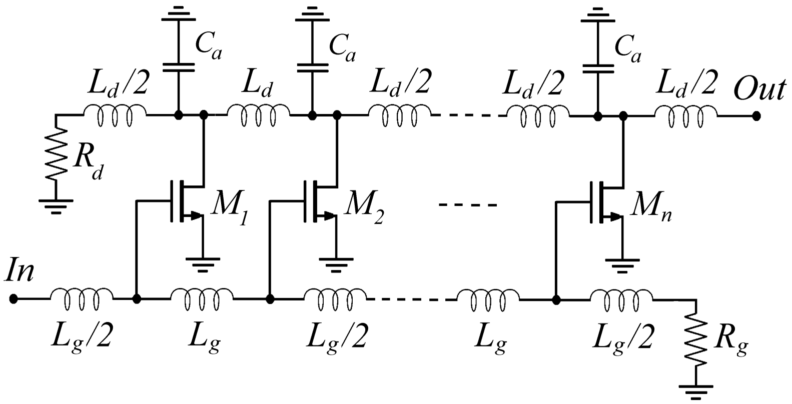

Figure 3.1: Circuit diagram of a conventional distributed amplifier (CDA).

In order that the signals amplified by each transistor arrive in phase to the output, the phase velocities of the gate and drain lines should be equal. This means:

$$\sqrt{L_g C_{gs}} = \sqrt{L_d(C_{ds} + C_a)}. \tag{3.2}$$

From (3.1) and (3.2), it can be concluded that $L_g = L_d$. The signals traveling in the left direction are out of phase and cancel out or are absorbed in the drain termination impedance of Z_d.

However, CDA has poor performance at high frequencies due to high loss associated with artificial transmission lines. One of the sources of this loss is due to the limited quality factors of the passive components such as inductors, capacitors and transmission lines implemented in the MMIC at high frequencies.

More importantly, the resistive parasitic elements of the transistor, the gate and drain resistances, create a large amount of loss in the drain and gate lines of the conventional DA. Therefore, as the signal travels along these lines, it is highly attenuated and there is no gain improvement by increasing the number of stages beyond an optimum value.

In [57], a typical CDA design guideline is presented. Theoretically by using properly designed transmission lines, an infinite bandwidth can be obtained with no limitation on gain. However, due to the losses associated with the transmission lines implemented in the DA structure, the gain-bandwidth product is limited to a fraction (≈0.7) of the cut off frequency of the amplifying device [57]. In the CDA by increasing the number of gain cells, the gain is slightly increased until the optimum number of gain cells is reached, and after that due to the loss associated with the circuit, no further improvement in gain is achieved.

For example, as shown in [57], using a typical 300 μm MESFET technology with f_{max}=77 GHz, $R_{gs}C_{gs}$=1.89 pF and $R_{ds}C_{ds}$=33 pF, a CDA with a voltage gain of 3.27 (10.3 dB power gain) and a cut-off frequency (f_{1dB}) of 16.52 GHz can be designed where R_{gs} and R_{ds} represent the ohmic losses associated with the gate and the drain of the amplifying device. In this example, the expected gain bandwidth product of the CDA is 0.7 of f_{max} and in practice due to the other loss mechanisms in the circuit, the measured result is lower than this expected value.

This problem will be a lot worse if a CMOS technology is used instead of the MESFET as the parasitic effects in the CMOS with a similar f_{max} are much higher than that of the MESFET. To increase the limited gain of the CDA, cascaded single stage DA (CSSDA) has been proposed in the literature [76–81]. By cascading two or more similar CDAs, the gain is multiplied by the number of cascaded stages while the band-width is slightly reduced. Based on the above mentioned example, if three CDAs are cascaded to each other, a gain of 35 is expected, however a large circuit with 12 gain cells and huge power consumption is required. Such configuration and design is not acceptable due to many practical issues.

In [62], by performing a noise analysis for the CDA, it is shown that, theoretically, for an infinite number of stages, N$\rightarrow \infty$, the N-stage distributed amplifier becomes noiseless. However, in reality for a large number of stages (e.g., more than 5 or 6 stages) other noise sources such as the thermal noise of the gate resistance and the inductor losses may dominate the noise figure. Finally, CDA has low pass characteristics and is not suitable for many wireless systems requiring the band pass amplifier response. Also, CDA has a limited gain, large layout foot print, high levels of power consumption and it is not optimized for noise.

3.2.2 Conventional Band Pass Distributed Amplifier

Conventional Band Pass Distributed Amplifier (CBPDA), using a low-pass to band-pass transformation technique, has already been proposed for applications which require a wide band-pass frequency response characteristics [10, 81–88]. Using this technique, each capacitor should be replaced by a parallel combination of a capacitor and an inductor, and each inductor should be replaced with a series combination of a capacitor and an inductor. This arrangement further increases the number of circuit elements which in turn decreases the circuit performance and increases its size.

Fig. 3.2 shows the schematic of a band pass DA using a low-pass to band-pass transformation technique.

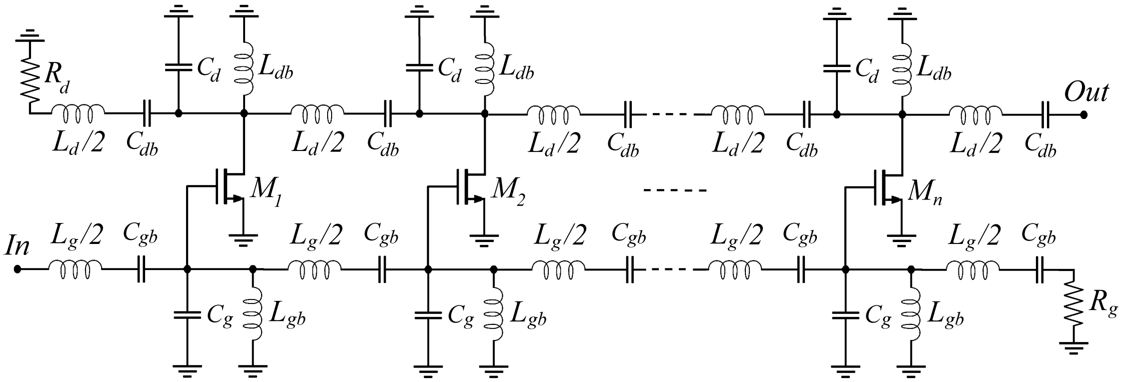

Figure 3.2: Circuit diagram of a conventional BPDA using low pass to band pass transformation [10].

As seen from this figure, the amplifier size is too large to be implemented in the MIMIC technology. In addition, due to the large number of capacitors, inductors and resistors which are lossy at the mmW, the gain and noise performances of the amplifier are poor. Also, due to the presence of capacitors in series configuration, a complex arrangement should be utilized to bias the transistors.

The performance of the published BPDAs in the literature is shown in Table 3.1.

As seen from Table 3.1, gain performance are obtained using the CBPDAs is considerably lower that what is required in many current applications.

3.3 The Novel Band Pass Distributed Amplifier (BPDA) Topology [1]

In this section, a new topology has been proposed to reduce the number of capacitors and inductors and to improve the amplifier gain and noise performances.

Table 3.1: Performance of the published CBPDAs in the literature.

Process	Discrete	Discrete	Discrete	120 nm SiGe	180 nm CMOS
Technology	BPF	BPF	Low pass to band pass transform.	High pass TLs	High pass TLs
$\lvert S_{21}\rvert$ (dB)	14	5	10	8.3	6.4
f_L (GHz)	0.5	12	2.33	21.5	9
f_H (GHz)	1	29	3.17	42.5	31
power consumption (mW)	-	-	120	-	46.8
Chip area (mm^2)	-	-	-	0.6	0.048
Year	1960	1988	2005	2010	2010
Reference	[82]	[83]	[85]	[86]	[80]

In this topology, by replacing the termination resistors in a conventional DA with short circuits as shown in Fig. 3.3, a band pass DA (BPDA) is obtained without the need for the conventional low pass to band pass transformation. Moreover, the input/output inductors ($L_g/2$ and $L_d/2$) have been replaced by L_{in} and L_{out} to achieve better input/output matchings.

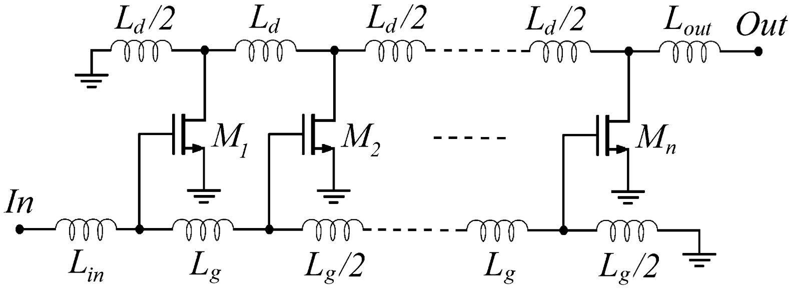

Figure 3.3: Circuit diagram of the proposed band pass distributed amplifier (BPDA).

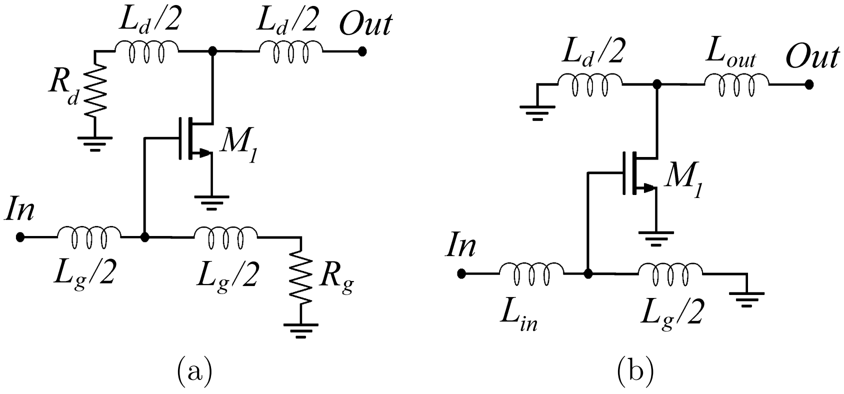

Figure 3.4: Topology of a single stage DA: (a) the CDA and (b) the proposed BPDA.

3.3.1 Single stage CDA and single stage BPDA transfer functions

A single stage of the proposed topology is shown in Fig. 3.4 with its conventional counterpart. It should be noted that for the single stage DA (SSDA), there is no need for the phase synchronization of the gate and drain lines, therefore, the extra drain capacitor, C_a, has been removed.

The termination impedances are replaced with short circuits in the BPDA topology, which increases its gain and decreases its noise figure as shown later in this section. The small signal models for the circuits in Fig. 3.4 are shown in Fig. 3.5.

The voltage gain of the single stage DA using KVL and KCL for the circuit

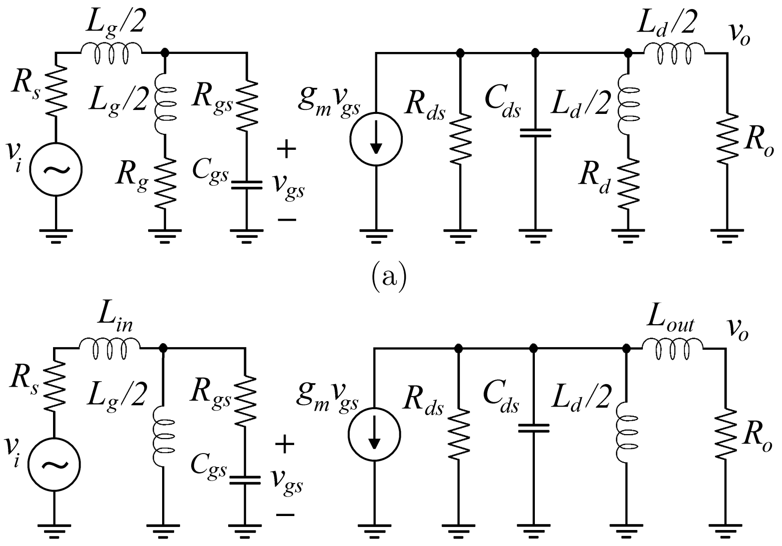

(a)

(b)

Figure 3.5: Equivalent small signal circuit for: (a) the Conventional DA (CDA) and (b) the proposed band pass DA (BPDA).

shown in Fig. 3.5 (a) with $R_g = R_S$ and $R_d = R_L$ is:

$$G_{SSDA} = \frac{v_o}{v_i} = -g_m R_L F_1(s) F_2(s) \tag{3.3}$$

where:

$$\begin{aligned} F_1(s) &= \frac{2R_{ds}}{s^2 L_d C_{ds} R_{ds} + s(L_d + 2C_{ds} R_L R_{ds}) + 4R_{ds} + 2R_L} \\ F_2(s) &= \frac{2}{s^2 L_g C_{gs} + s C_{gs}(2R_S + 4R_{gs}) + 4} \end{aligned} \tag{3.4}$$

As seen from equations (3.3) and (3.4), the CDA has a low pass frequency characteristic. To show the frequency response of the proposed BPDA topology, the voltage gain of Fig. 3.5 (b) is calculated as:

$$G_{BPDA} = \frac{v_o}{v_i} = -g_m R_L G_1(s) G_2(s) \tag{3.5}$$

where $G_1(s)$ and $G_2(s)$ are given as:

$$G_1(s) = \frac{sL_g}{s^3L_gL_{in}C_{gs} + s^2C_{gs}(R_{gs}L_g + 2L_{in}R_{gs} + R_SL_g) + s(L_g + 2L_{in} + 2R_{gs}C_{gs}R_S) + 2R_S} \tag{3.6a}$$

$$G_2(s) = \frac{sL_dR_{ds}}{s^3L_dL_{out}R_{ds}C_{ds} + s^2L_d(L_{out} + R_LR_{ds}C_{ds}) + s(L_dR_L + 2L_{out}R_{ds} + L_dR_{ds} + 2R_LR_{ds}} \tag{3.6b}$$

Equations (3.5) and (3.6) show that the amplifier has a bandpass frequency response.

To compare the voltage gain of the proposed topology with that of the CDA we assume that $L_{in} = L_g/2$ and $L_{out} = L_d/2$ as is the case in the CDA. Using these assumptions, the voltage gain of the BPDA is given as:

$$G_{BPDA} = -g_mR_LH_1(s)H_2(s) \tag{3.7}$$

where $H_1(s)$ and $H_2(s)$ are:

$$H_1(s) = \frac{2sL_dR_{ds}}{s^3Ld^2C_{gs}R_{ds} + s^2(L_d^2 + 2L_dC_{ds}R_{ds}R_L) + 2sL_d(R_L + 2L_dR_{ds}) + 4R_{ds}R_L} \tag{3.8a}$$

$$H_2(s) = \frac{2sL_g}{s^3Lg^2C_{gs} + 2s^2C_{gs}L_g(2R_{gs} + R_S) + 4s(L_g + R_{gs}C_{gs}R_S) + 4R_S} \tag{3.8b}$$

In the above analysis, the inductors are assumed to be lossless and the high frequency drop in the frequency response of the CDA is due to the effect of R_{gs} and R_{ds}, which introduce loss in the artificial gate and drain transmission lines of the DA.

Fig. 3.6 compares the magnitude of the power gain,$|S_{21}|$, of the proposed topology for various termination resistor where $R_d = R_g = 50\Omega$ and $R_d = R_g = 0\Omega$ are the cases for CDA and BPDA topologies, respectively. In this figure, the frequency response and power gain are related by the following equation:

$$20 * log|S_{21}| = 20 * log|H(s)| + 6\,dB \tag{3.9}$$

It is interesting to note that the frequency characteristic of the amplifier is band pass for all terminations less than $50\,\Omega$ and low pass for terminations greater than or equal to $50\,\Omega$ (For the CDA, terminations are $50\,\Omega$). From Fig. 3.6, the frequency response of the BPDA is band pass and its gain is much higher than that of the CDA. The gain superiority of the proposed amplifier with respect to that of the CDA is also clear in Fig. 3.6.

To increase the overall gain of a CDA, multi-stage DA topology shown in Fig. 3.1 is used. However, the gain enhancement is limited as the signal traveling in the lossy artificial gate and drain lines is highly attenuated. Therefore, there will be no further gain increment after the optimum number of stages at the given frequency is reached [57].

The low-pass to band-pass transformation to obtain band-pass response from a CDA further degrades its gain, therefore, it is not suitable for high gain mmW amplifiers using the low-cost CMOS technology. On the other hand, the proposed BPDA, boosts the performance of the amplifier by properly absorbing the unwanted transistor parasitics to provide a high gain band-pass amplification as it is shown in this section.

The reduction in the number of elements in each stage and the number of the required stages to achieve a required performance in the BPDA topology cause its chip area and power consumption to be very small compared to those of the CDAs. The performance comparison of the CDA and BPDA will be presented in section 4.6.

The price paid for this performance improvement is the risk of instability. In section 3.3.4, the guidelines to design a stable BPDA will be presented.

Fig 3.7 shows the simulated noise figure of the above mentioned topologies. The transistor noise model has been added to the small signal circuits shown in Fig. 3.5. All other parameters are given in Fig. 3.6. Since there are no noisy resistive terminations in the new topology, its noise figure is much less than that of the CDA in the higher frequencies. This is a considerable improvement given the fact that the noise figure considerably increases at higher frequencies.

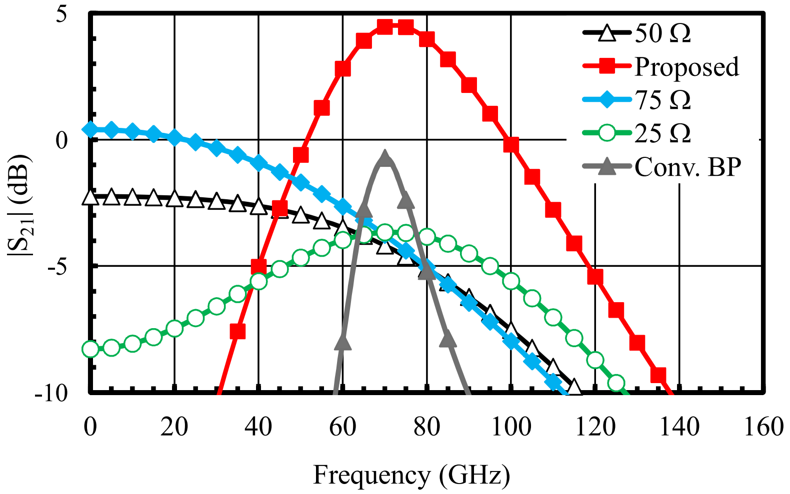

Figure 3.6: Gain comparison of the single stage DA for different termination resistors ($R_d = R_g$). The gain cell parameters are: $L_g = 130$ pF, $L_d = 140$ pF, $C_{gs} = 95$ fF, $C_{ds} = 65$ fF, $R_{gs} = 4\,\Omega$, $R_{ds} = 55\,\Omega$, $g_m = 45$ mS and $R_L = R_S = 50\,\Omega$ (see Fig. 3.4).

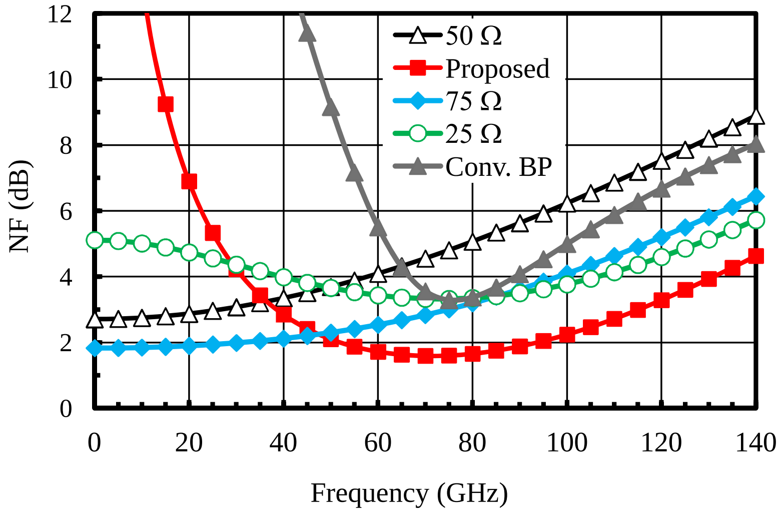

Figure 3.7: Noise figure comparison of different DA topologies.

3.3.2 Bandwidth and center frequency calculations

From equations (3.6), it is seen that the gain functions, $G_1(s)$ and $G_2(s)$ have a band pass behavior. As is common in the band pass filter design, to calculate the center frequency of each gain function, we should find the frequency where these functions become real which means:

$$\begin{aligned} Im[G_1(j2\pi f_{01})] &= 0 \\ Im[G_2(j2\pi f_{02})] &= 0 \end{aligned} \tag{3.10}$$

where f_{01} and f_{02} are the center frequencies of $G_1(s)$ and $G_2(s)$, respectively. The solutions of the equations (3.10) can been easily found:

$$f_{01} = \frac{1}{2\pi}\sqrt{\frac{2R_S}{C_{gs}(L_g R_{gs} + 2L_{in}R_{gs} + R_S L_g)}} \tag{3.11a}$$

$$f_{02} = \frac{1}{2\pi}\sqrt{\frac{2R_L R_{ds}}{L_d(L_{out} + R_L R_{ds} C_{ds})}} \tag{3.11b}$$

The bandwidth and center frequency of the amplifier can be estimated by $BW \simeq f_{02} - f_{01}$ and $f_0 \simeq \sqrt{f_{02}f_{01}}$, respectively. It is interesting to note that f_{01} is a function of gate parameters only (input) and f_{02} is a function of drain parameters only (output).

Therefore, to design a gain cell, first we assume that $L_{in} = L_g/2$ and $L_{out} = Ld/2$ as it is the case in the CDA design. Using this assumption, equations (3.11) reduce to:

$$f_{01} = \frac{1}{2\pi}\sqrt{\frac{2R_S}{C_{gs}L_g(2R_{gs} + R_S)}} \tag{3.12a}$$

$$f_{02} = \frac{1}{\pi}\sqrt{\frac{R_L R_{ds}}{L_d(L_d + 2R_L R_{ds} C_{ds})}} \tag{3.12b}$$

By proper choice of L_g and L_d and using equations (3.12), the amplifier can be designed for any required bandwidth. For example to design a V-band BPDA to work from 50 to 70 GHz, we choose $L_g = 194\,pH$ for $f_{01} = 50$ GHz and $L_d = 121\,pH$ for $f_{02} = 70$ GHz using equations (3.12) for $C_{gs} = 95$ fF, $C_{ds} = 65$ fF, $R_{gs} = 4\,\Omega$, $R_{ds} = 55\,\Omega$ and $R_L = R_S = 50\,\Omega$.

3.3.3 Input/output matchings

In order to optimize the input and output return losses for the proposed band pass DA, the input and output reflection coefficients for Fig. 3.5 (b) should be first calculated. These coefficients are calculated and expressed in equations (3.13).

$$\Gamma_{in}(s) = \frac{s^3 L_{in} L_g C_{gs} + s^2 C_{gs}[(2L_{in} + L_g)R_{gs} - L_g R_S] + s(2L_{in} + L_g - 2C_{gs}R_{gs}R_S) - 2R_S}{s^3 L_{in} L_g C_{gs} + s^2 C_{gs}[(2L_{in} + L_g)R_{gs} + L_g R_S] + s(2L_{in} + L_g + 2C_{gs}R_{gs}R_S) + 2R_S} \tag{3.13a}$$

$$\Gamma_{out}(s) = \frac{s^3 L_{out} L_d C_{ds} R_{ds} + s^2 L_d(L_{out} - C_{ds}R_{ds}R_L) + s[(2L_{out} + L_d)R_{ds} - L_d R_L] - 2R_{ds}R_L}{s^3 l_{out} L_d C_{ds} R_{ds} + s^2 L_d(L_{out} + C_{ds}R_{ds}R_L) + s[(2L_{out} + L_d)R_{ds} + L_d R_L] + 2R_{ds}R_L} \tag{3.13b}$$

Substituting the obtained value of L_g from section 3.3.2 into equations (3.13a), the input reflection coefficient can be expressed as a function of L_{in} at the frequency of operation. Then using numerical methods, L_{in} can be obtained for the minimum input reflection coefficient. A similar procedure can be applied to the output reflection coefficient to calculate L_{out}.

It is interesting to note that L_{in} and L_{out} have little effect on f_{01} and f_{02}. This can be proven by recalculating f_{01} and f_{02} from equations (3.12) using L_g, L_d, L_{in} and L_{out} obtained from equations (3.12) and (3.13).

Fig. 3.8 shows the input and output matching of BPDA for the gain cell with $L_{in} = 78\,\text{pH}$ and $L_{out} = 0\,\text{pH}$ obtained using the above optimization process. All other parameters are given in Fig. 3.6.

3.3.4 Stability consideration

So far the transistor is considered as a unilateral device, however, all transistors have some feedback mechanisms which push the amplifier to the unstable region. This is more critical for the CMOS transistor with high C_{dg}, which has highly

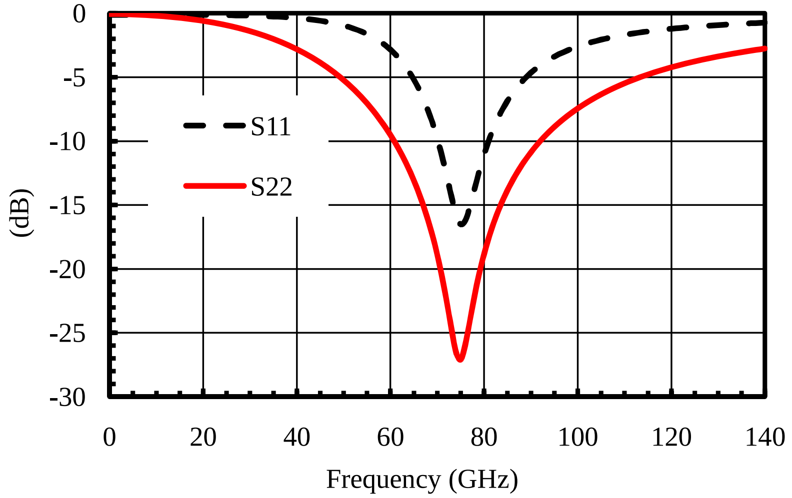

Figure 3.8: Input and output matching of band pass DA for the gain cell with the parameters given in Fig. 3.6 and with $L_{in} = 78\,\text{pH}$ and $L_{out} = 0\,\text{pH}$.

bilateral properties. Therefore, a proper method should be implemented to make the gain cell unconditionally stable.

In addition, the higher gain provided by the BPDA and the presence of standing waves in its gate and drain lines (unlike CDAs) increase the risk of instability. On the other hand, limited g_m of transistors and low quality factor passive components (inductors and capacitors) implemented in the mmW CMOS technology decrease the gain but increase the circuit stability at very high frequencies.

Careful analysis and simulations are required to examine the stability of the amplifier. In [4], by placing a small inductor in the source of the transistor, sufficient stability margin has been achieved. Another method to improve the stability is to replace a common source gain cell with a cascode one. The cascode gain cell has been widely used in the MMIC [79, 89] due to the high input to output isolation which reduces the risk of instability. However, the cascode topology has higher noise figure than that of the common source due to the implementation of the common gate transistor. In addition, usually a large number of inductors are required to implement a cascode stage, leading to a large chip area.

Unconditional stability of an amplifier can be determined by "K, Δ" test based on Rollet's conditions [90, 91]:

$$K = \frac{1 - |S_{11}|^2 - |S_{22}|^2 - |\Delta|^2}{2|S_{12}||S_{21}|} > 1 \tag{3.14a}$$

$$\Delta = |S_{11}S_{22}||S_{12}S_{21}| < 1 \tag{3.14b}$$

For an unconditionally stable amplifier, the above conditions should be simultaneously satisfied. Otherwise, the stability circles must be used to determine if there are source and load reflection coefficients for which the gain cell is conditionally stable. Also one should have $|S_{11}| < 1$ and $|S_{22}| < 1$ for the gain cell to be unconditionally stable.

While K, Δ test of equations (3.15) are mathematically rigorous conditions for unconditional stability, they cannot be used to compare the relative stability of two or more gain cells since it involves constraints on two separate parameters. Another set of criteria for input and output stabilities, which are useful for comparing the stabilities of two or more gain cells, are expressed as [92]:

$$\mu = \frac{1 - |S_{11}|^2}{|S_{22} - \Delta S_{11}^*| + |S_{12}S_{21}|} > 1 \tag{3.15a}$$

$$\acute{\mu} = \frac{1 - |S_{22}|^2}{|S_{11} - \Delta S_{22}^*| + |S_{12}S_{21}|} > 1 \tag{3.15b}$$

Fig. 3.9 (a) shows the input and output stability factors, μ and μ', respectively, for a typical gain cell of the proposed BPDA with the circuit parameters given in section 3.3.1 and by adding a C_{gd}=10 fF. Fig. 3.9 (b) also shows the stability factors for the same gain cell with a $C_{gd} = 20$ fF. From Fig. 3.9 (a), for the gain cell with $C_{gd} = 10$ fF, both μ and μ' are higher than unity which means the gain cell is unconditionally stable at all frequencies, while for the case of $C_{gd} = 20$ fF, μ and μ' are less than unity at some frequencies which means the gain cell is not unconditionally stable. In order to ensure the unconditional stability of the gain cell, a degenerative inductor can be placed at the source of the amplifying transistors as mentioned above. Fig. 3.9 (c) shows the stability factors of the gain cell with $C_{gd} = 20$ fF in which a small inductor of $L_s = 10$ pH has been placed between the source of the transistor and the ground. This ensures the unconditional stability of the gain cell at all frequencies.

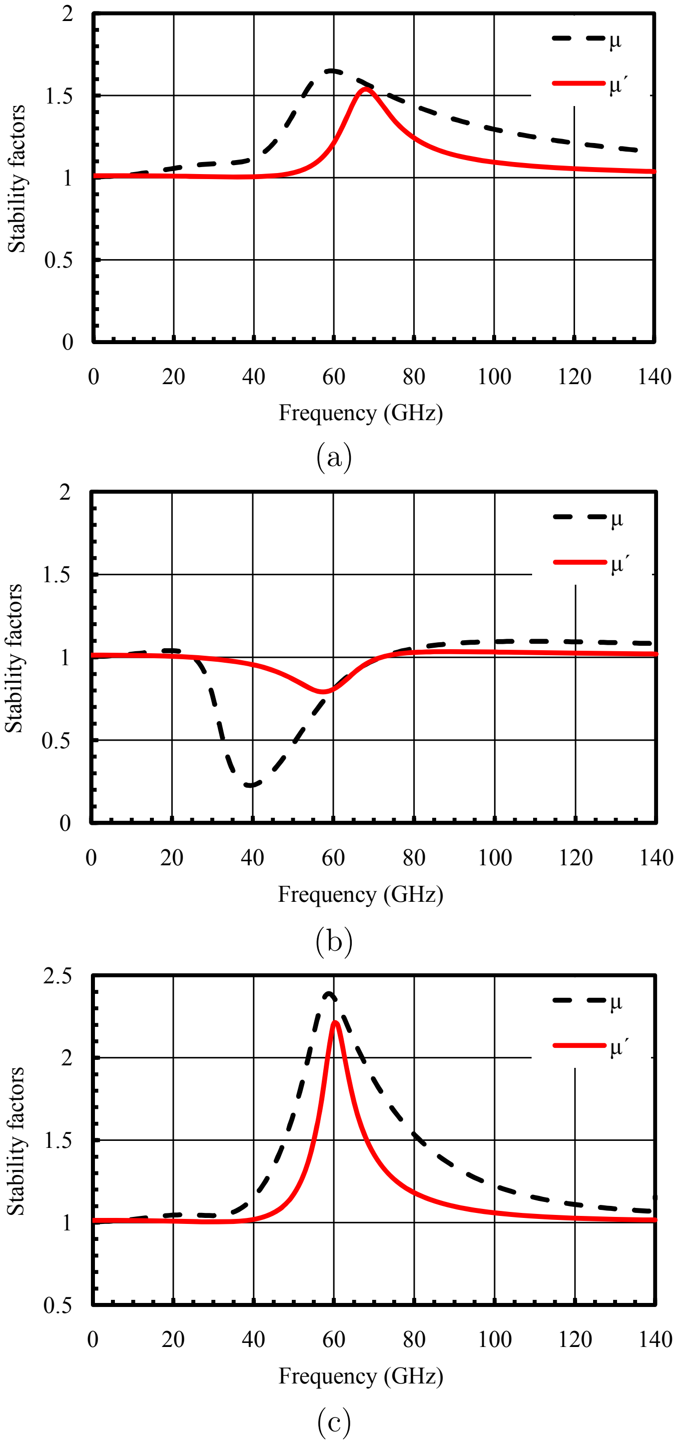

Figure 3.9: Input and output stability factors of a proposed BPDA with added (a) C_{gd}=10 fF (b) C_{gd}=20 fF and (c) C_{gd}=20 fF and L_s=10 pH.

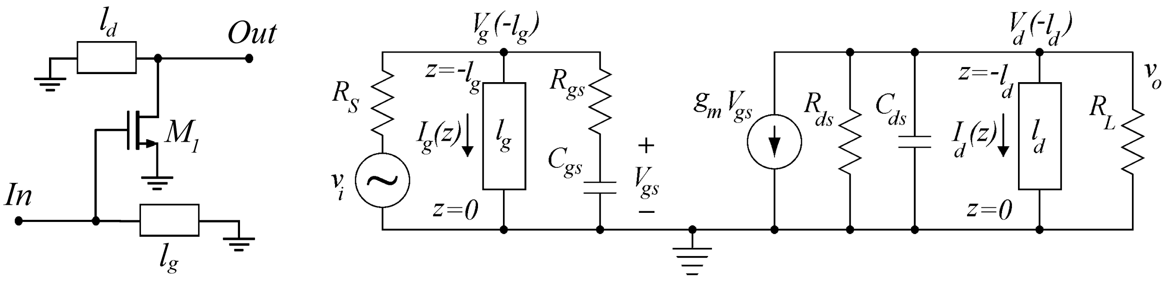

(a) (b)

Figure 3.10: Topology of a single stage: a) Single stage DA and b) the proposed band pass DA.

3.3.5 TL (Transmission Line) analysis of the single stage BPDA topolgy [2]

The presented analysis in section 3.3.1 and 3.3.2, is not accurate enough at higher frequencies like mmW band. This is due to the fact that in these frequencies the dimension of the circuit elements becomes comparable to the wavelength. Therefore, the lumped element model cannot precisely predict the frequency characteristics of the amplifier. In addition, the lumped element model does not take into account the loss of transmission lines. Usually at mmW, inductors are realized by TL segments, therefore, TL equations must be used in the derivation the voltage gain of amplifier.

Fig. 3.10 (a) shows the schematic of the proposed topology shown in Fig. 3.4 (b) in which L_{in} and L_{out} have been eliminated for simplicity and all other inductors are replaced by pieces of transmission line. Fig. 3.10 (b) is the equivalent circuit of Fig. 3.10 (a) where the transistor is represented by its small signal equivalent model.

Each TL is characterized by three parameters, Z_0, α and β which are the characteristics impedance, attenuation constant and the phase constant, respectively. The voltage and current at the input of a piece of transmission line with length l, short circuited at the other end can be written as:

$$\begin{aligned} V(z=-l) &= V^+(e^{\gamma l} - e^{-\gamma l}) \\ I(z=-l) &= \tfrac{V^+}{Z_0}(e^{\gamma l} + e^{-\gamma l}) \end{aligned} \tag{3.16}$$

Using equations (3.16) for Fig. 3.10 (b), one can easily calculate the voltage gain of a single stage of the amplifier as:

$$E(s) = \frac{v_o}{v_i}(TL\ model) = -g_m R_L E_1(s) E_2(s) \tag{3.17}$$

where:

$$E_1(s) = \frac{1}{[1 + \frac{R_S}{Z_0}\coth(\gamma_g l_g)](1 + sC_{gs}R_{gs}) + sC_{gs}R_S} \tag{3.18a}$$

$$E_2(s) = \frac{1}{[\frac{R_L}{Z_0}\coth(\gamma_d l_d)] + sC_{ds}R_L + \frac{R_{ds}+R_L}{R_{ds}}} \tag{3.18b}$$

and $\gamma = \alpha + j\beta$.

For a lossless TL, $\gamma = j\beta$. Then:

$$\coth(\gamma_g l_g) = \coth(j\beta_g l_g) = \coth(j\frac{\omega}{v_g} l_g) = \coth(s\tau_g) \tag{3.19}$$

Using Taylor expansion for $\coth(s\tau_g)$ which is:

$$\coth(s\tau_g) = \frac{1}{s\tau_g} + \frac{s\tau_g}{3} + \dots \tag{3.20}$$

and considering the low frequency approximation of equation (3.20) which is $\coth(s\tau_g) \simeq 1/s\tau_g$:

$$\frac{\coth(s\tau_g)}{Z_0} \simeq \frac{1}{s\tau_g Z_0} = \frac{v_g}{s l_g Z_0} = \frac{1/\sqrt{\bar{L}_g \bar{C}_g}}{s l_g \sqrt{\bar{L}_g/\bar{C}_g}} = \frac{2}{sL_g} \tag{3.21}$$

where $L_g/2 = \bar{L}_g l_g$ and $\bar{L}_g$ is inductance per unit length of gate TL.

Substituting $\coth(s\tau_g)/Z_0 \simeq 2/sL_g$ into equation (3.18a) one can easily prove that $E_1(s) = G_1(s)$. Using the same procedure as above, one can show that $E_2(s) = G_2(s)$ where $G_1(s)$ and $G_2(s)$ are the voltage gain obtained by a lumped element model presented in equations (3.6) of section 3.3.1.

The aforementioned facts show that, at low frequency and for the lossless case, the TL analysis and lumped element models predict similar frequency response for the amplifier. The lumped model approximation is valid if $1/s\tau_g \gg s\tau_g/3$ i.e. $1/s\tau_g > 20s\tau_g$ which means $l < 0.06\lambda$.

Now, considering $\coth(s\tau_g) \simeq 1/s\tau_g + s\tau_g/3$ and substituting into equation (3.18a), the second order approximation of $H_1(s)$ can be obtained. Using the same approach described in [2], the center frequency of this gain function, f_{01}, at which $Im[G_1(j2\pi f_{01})] = 0$ can be calculated as follow:

$$f_{01} = \frac{Z_0}{2\pi}\sqrt{\frac{12R_S}{L_g[L_gR_S + 6Z_0^2C_{gs}(R_S + R_{gs})]}} \tag{3.22}$$

With a similar procedure, the second order approximation of $H_2(s)$ and the center frequency of the gain function, f_{02} can be calculated as follows:

$$f_{02} = \frac{Z_0}{2\pi}\sqrt{\frac{12}{L_d(L_d + 6Z_0^2C_{ds})}} \tag{3.23}$$

The bandwidth of the amplifier is $BW = |f_{02} - f_{01}|$ and its center frequency is $f_0 = \sqrt{f_{01}f_{02}}$.

Fig. 3.11 (a) and (b) compare the voltage gain transfer functions obtained by the TL model and those obtained by lumped element one using the parameters for a typical mmW gain stage of a single gain cell, respectively. In Fig. 3.11 (c) we also compared the power gain obtained by the TL and lumped element models for 2 cascaded gain cells.

In this gain stage, 210 μm transmission lines in a substrate with ϵ_{reff}=4.1 has been used to realize 125 pH inductors for both gate and drain lines. From Fig. 3.11, at low frequency where the loss is negligible and $l < 0.06\lambda$, the gain obtained by lumped element model and that obtained by TL model are approximately the same. However, at high frequency where $l < 0.06\lambda$ is no longer valid and the loss is significant, there is a considerable difference between the gain calculated by each model. Therefore, for amplifier design at high frequency the lumped model approximation is no longer valid and models based on the TL model must be used.

Table 3.2 compares the center frequencies of the gain functions obtained by first and second order approximation of equations (3.18) and those obtained from the TL analysis which is derived by numerically solving equations (3.18). This table clearly shows that the first order approximation is not accurate for the frequencies above 100 GHz where $\lambda_{eff} < 1470$ μm and the assumption of $l < 0.06\,\lambda_{eff}$

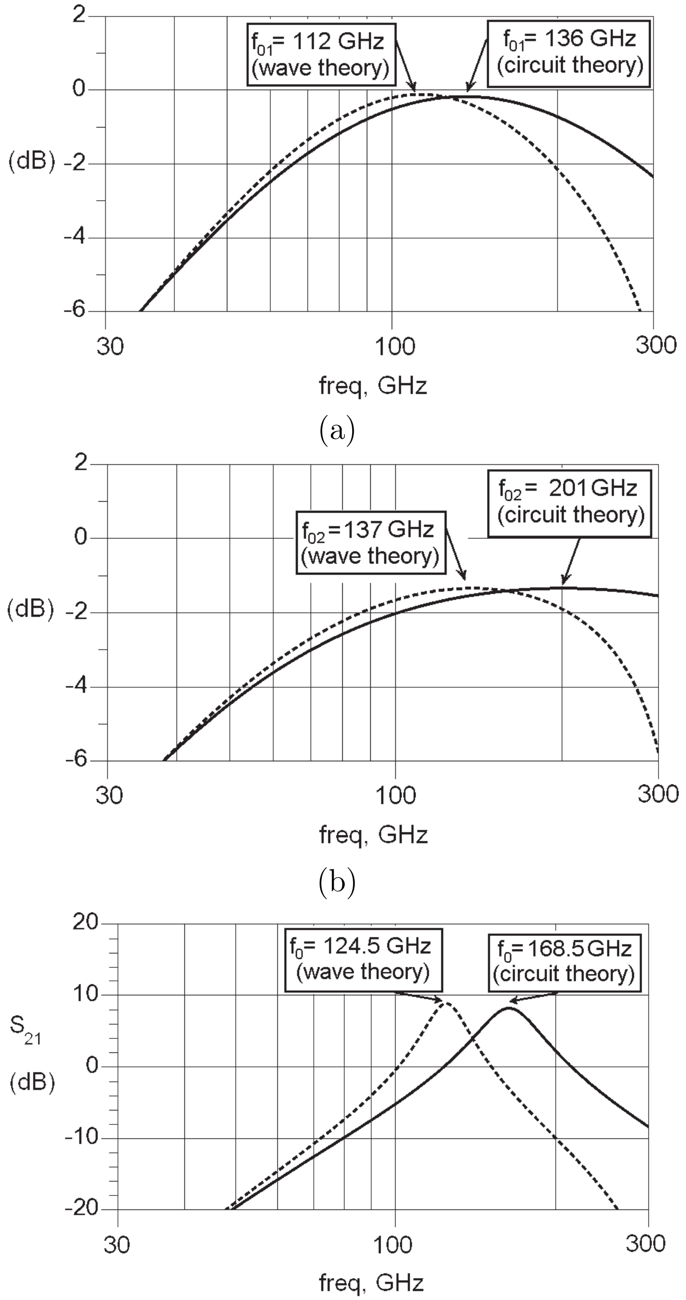

(a)

(b)

(c)

Figure 3.11: Comparison of gain functions for: (a) G_1, H_1, (b) G_2, H_2 for single gain cell and (c) power gains G and H for a 2 stages CSSDA using the TL model (dashed line) and lumped element model (solid line).

for l=210 μm is no longer valid. However, the center frequencies obtained by second order approximation are quite close to those obtained by numerically solving equations (3.18).

Table 3.2: Comparison Results

Calculation Method	f_{01} (GHz)	f_{02} (GHz)	f_0 (GHz)
The TL analysis using equations (3.18)	112	137	123.9
Second order approx. using equations (3.22-3.23)	111	139	124.2
First order approx. using equations (3.12)	136	201	165

The gain cell parameters are: $L_g = L_d$=250 pF, C_{gs}=10 fF,C_{ds}=5 fF, R_{gs}=5 Ω, R_{ds}=300 Ω, $R_S = R_L$=50 Ω and Z_0=86 Ω.

3.4 Conclusion

In this chapter, a novel band pass distributed amplifier (BPDA) topology is presented to realize high performance and miniaturized integrated circuits in the mmW using the low cost CMOS technology.

For the first time, it is shown that using short circuit for the line terminations in the distributed amplifier (DA), which creates a non-traveling (standing) wave in the lines eliminates the low frequency portion of the DA frequency response, which is most vulnerable to oscillation. The parasitic elements of both the amplifying transistors and the transmission lines contribute to the stability of the circuit. This is very advantageous especially when a lossy fabrication technology such as cost-effective CMOS is being used. In addition, in the absence of the resistance for the line terminations, the proposed circuit would have less power dissipation; resulting in higher power efficiency, lower noise figure and significantly higher amplification gain. Another advantage of the proposed topology is that as no matching impedances are used in the line terminations; the footprint of the circuit for integrated circuit fabrication is significantly smaller in comparison to that of the CDAs.

The frequency response and design formulas for a single stage BPDA are obtained using both lumped element and TL models. The results are in excellent agreement at low frequencies while the lumped element model is no longer valid at high frequencies, where the TL model must be used. Input/output matching and stability requirements for this amplifier are also presented.

For a typical gain cell, while the CDA and the conventional BPDA using a low pass to band transform, fail to provide any gain, the proposed topology achieves more than 4.5 dB gain per stage, while its noise figure is less than the conventional topologies. Therefore, the proposed topology is very promising for mmW low-cost applications.

In chapter 4, it will be shown that by cascading multiple stages, the amplifier gain can be boosted. The performance comparison of the designed and fabricated BPDAs with the state of the art will be presented later in this chapter.

Chapter 4

Design and Fabrication of Optimum Millimeter Wave Low Noise Band Pass DAs (BPDA)

4.1 Introduction

As seen in chapter 2, the proposed integrated active lens architecture was presented as a unique solution to implement cost-effective mmW beam-scanning receivers using high gain miniaturized LNAs. To achieve miniaturized, cost-effective and high gain amplification, a new BPDA was proposed and analyzed in chapter 3.

In this chapter, after presenting a new methodology to design a low noise and stable BPDA, design and fabrication of a 60 GHz LNA by cascading 4 similar single stage BPDAs using a 130 nm CMOS technology is presented. To obtain a higher performance, the design is further improved by optimized the component values in the circuit such that the stages are no longer similar and a high performance 6-stage amplifier is achieved.

An amplifier figure of merit is defined to compare the performance of the designed and fabricated amplifiers with the state of the art LNA's at mmW. This comparison shows the superiority of the proposed topology for high performance mmW amplifiers using a cost effective CMOS technology.

To explore the capability of the proposed topology at frequencies above the

f_t of technology, amplifiers at 77 and 85 GHz are designed and the fabrication of the 85 GHz amplifier is presented. Finally, to show the capability of the proposed topology in implementing wide-band mmW amplifiers, a multi-stage BPDA is designed. The comparison between this design and the state of the art, demonstrate a considerable performance improvement in design of wide-band mmW LNAs.

4.2 Characterization of an On-Chip Transmission Line for CMOS MMIC Applications [3]

CMOS/SiGe technologies are promising for low cost MMIC systems [46, 93–96]. Other than high frequency transistors, high quality passive elements are needed to realize circuit building blocks for these systems. Low resistivity silicon substrate which is required for active elements highly reduces the quality factor of on-hip passive elements [94–97]. As the frequency increases, various loss mechanisms increase the signal attenuation in CMOS/SiGe passive elements. High performance transmission lines (TLs) are required to provide low loss interconnection and to replace bulky and lossy inductors in MMIC.

Over mmW range of frequencies, TL segments are increasingly used to realize various high quality factor passive elements. TLs have broad band characteristics and are easier to be modeled [96]. Usually, coplanar waveguide (CPW) is used in RF circuits for this purpose. However, as the frequency goes higher, CPW suffers from increased substrate loss [97, 98]. This is due to the thin dielectric layer in CMOS back end of line (BEOL) which is in order of a few microns. Thus, the field lines penetrate into the lossy silicon substrate and deteriorate the quality factor of the line [97].

To alleviate this problem, grounded CPW (GCPW) is proposed for microwave frequencies [95–98]. Using the bottom thin metal layer of BEOL, a mesh grid is utilized to shield the signal from the lossy silicon substrate. Mesh structure is implemented in order to meet the metal density requirements for reliable fabrication process as a part of density design rules. However, GCPW structure requires a large gap between signal and ground planes which makes it difficult to be implemented in the presence of metal density rules and also occupy more expensive chip area [97]. In comparison, microstrip structures, if properly designed, provide higher quality factor, inductance per lengths and smaller size. These properties make microstrip lines suitable for MMIC applications.

A TL structure, which is suitable for MMIC in CMOS/SiGe technologies, is presented in this section. Instead of conventional open, short and through de-embedding methods [99–102], which occupies a large chip area, a simple yet accurate de-embedding method using two lines with different lengths is employed. The lines are characterized and line parameters are derived and verified by measurement.

4.2.1 On-chip TL structure

A simplified TL structure is shown in Fig. 4.1.

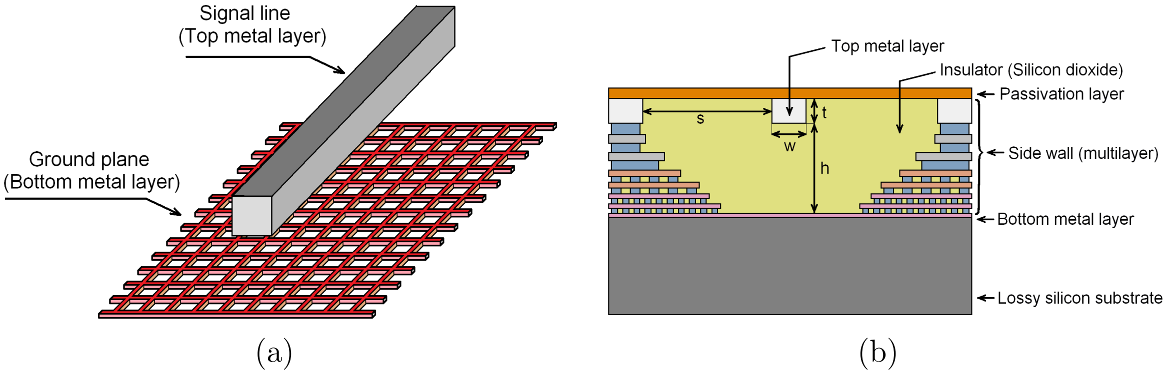

Figure 4.1: A high quality factor microstrip transmission line implemented in the CMOS technology. (a) The simplified structure and (b) the cross section [3].

The signal is carried by the top metal layer. This layer is very thick ($4\,\mu$m) to reduce the conductor loss. Bottom metal layer is used to shield the signal from the lossy silicon substrate. A mesh structure as shown in Fig. 4.1 (a) is used to meet the density rules for this layer. The dielectric is a multi-layer silicon dioxide structure. Fig. 4.1 (b) shows the cross section of the proposed guided microstrip line (GMSL) structure. Curved side walls are constructed using all metal layers and vias available in the BEOL. They are implemented in order to confine and guide the wave in the structure and to reduce its interference with adjacent elements.

4.2.2 TL EM-simulation

The structure is simulated using the ANSYS HFSS 3-D full-wave EM-simulation CAD tool [103]. Fig. 4.2 shows the electric field distribution for the first mode which is similar to that of a planar MSL.

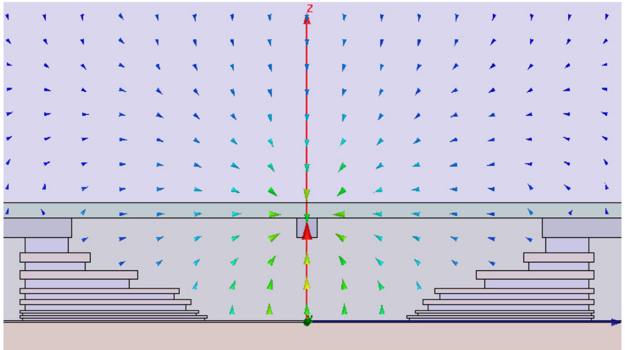

Figure 4.2: Simulated E-field distribution at the wave ports of a GMSL.

TLs are simulated with various lengths, l, from 10 μm to 100 μm to make sure that the results are consistent with both short and long lines. Also parametric sweep is employed for different values of the line width, w. There is a trade-off between quality factor, Q, the equivalent inductance, L and the width of the line. w=4 μm leads to an optimum GMSL with L=62 pH at 30 GHz. It should be noted that, the results are consistent as long as s>30 μm.

4.2.3 TL fabrication and measurement

Optimized lines are fabricated using a low cost 0.13 μm CMOS process in three different lengths of 100, 150 and 200 μm. Another 100 μm line is fabricated in a different fabrication run to validate the consistency of the fabrication and measurement processes. Fig. 4.3 shows the die photos of the fabricated 100 μm and 200 μm lines.

To minimize the pad parasitics, small octagonal pads (w=50 μm) , with a high resistive isolating ground layer are used.

The standard 50 Ω, 2-port S-parameter measurements are performed using an Anritsu ME7808B broadband VNA and a Cascade Microtech Inc (CMI) Summit 12761B probe station system with 150 μm probe pitches. An LRRM calibration

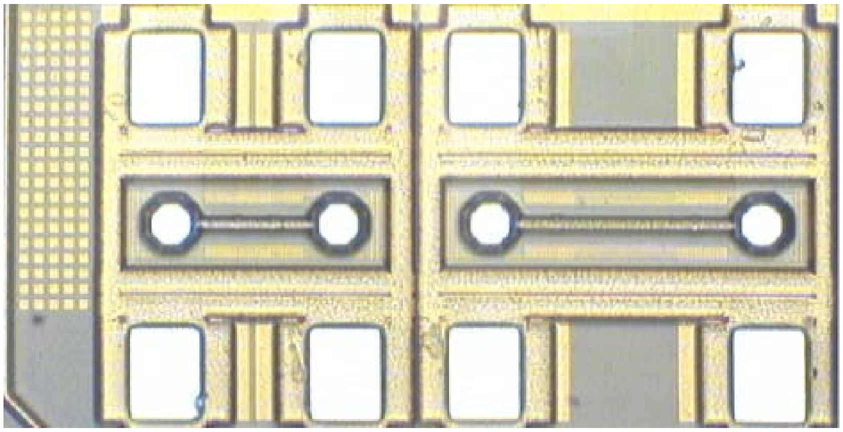

Figure 4.3: Die photo of fabricated lines with (a) 100 μm and (b) 200 μm lengths.

technique is performed based on CMI's custom expansion of the standard LRM technique in order to move the reference plane from the VNA output ports to the probe tips. The WinCal XE calibration software is employed which operated in conjunction with the Nucleus probe station software.

4.2.4 TL parameter extraction

Parameter extraction is performed based on the method explained in [104] from the measured data of the 200 and 100 μm lines.

Simulated and extracted S-parameters for a 100 μm line are shown in Fig. 4.4 and are in a good agreement.

Also, parameters of a 50 μm line segment are extracted for 200/150 μm and 150/100 μm as long/short lines, respectively. The extracted and simulated attenuation and (b) Phase constans , α, and phase constant β are compared in Fig. 4.5 (All converted to 100 μm segments).

Using other extracted parameters, the TL can be easily modeled at mmW as explained in [3].

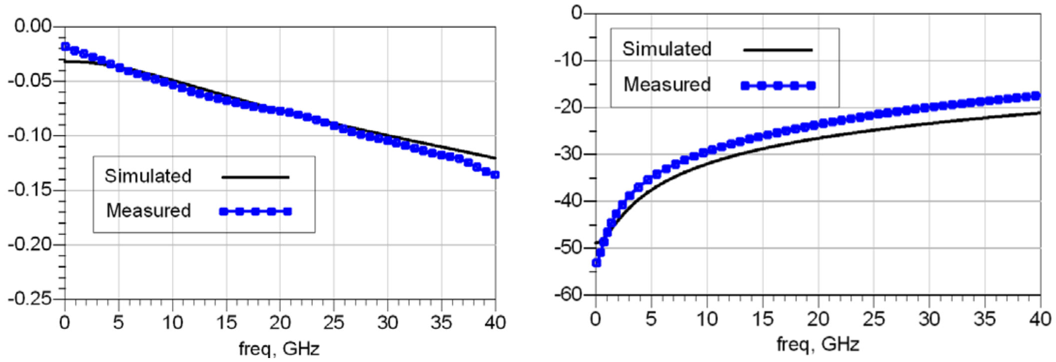

(a) (b)

Figure 4.4: Comparison of extracted and simulated S-parameters for fabricated 100 μm line segment. (a) S_{21} and (b) S_{11}.

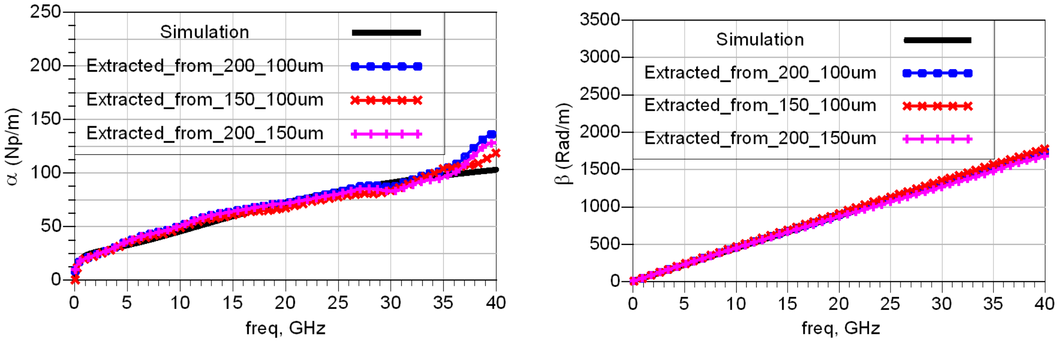

(a) (b)

Figure 4.5: Extracted and simulated TL paraments for a 100 μm line segment. (a) Attenuation constant and (b) Phase constant.

4.3 Low Noise Design of a Single Stage BPDA [4]

Noise figure is one of the most important characteristics of a low noise amplifiers. As shown in Fig. 3.7, the proposed topology if properly designed, provides an optimal noise figure in the desired frequency band. This is also depending on the transistor noise parameters. The noise parameters of a typical mmW CMOS transistor are used in the simulations shown Fig. 3.7.

In this section, a design method to obtain a simultaneous desired optimum noise, gain and stability performances is presented. This is achieved by adding degenerating inductors, L_{gg} and L_s, in the gate and source of the MOS transistor of the BPDA topology shown in Fig. 3.4 (b), respectively. The proposed method is based on this assumption that the initial values of L_{in} and L_s for the optimum input matching and stability margin are obtained using the analysis discussed in chapter 3. Also, it is assumed that the value of L_{in} is small enough to be neglected in this analysis.

Fig. 4.6 shows the resulted gain cell. L_{gg}, and L_s are added to the circuit to achieve noise figure and stability design goals.

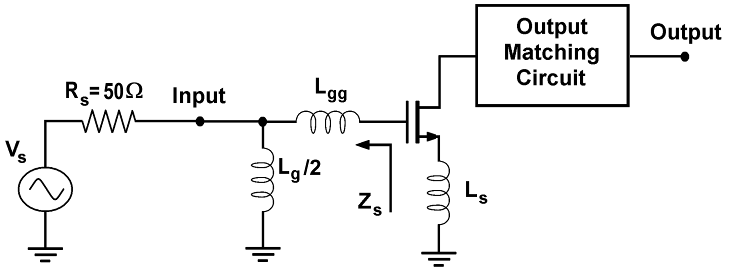

Figure 4.6: The circuit diagram of the proposed gain cell with degeneration inductors.

It is assumed that the transistor design parameters such as its gate width, W, gate length, l, number of gate fingers, nf, and its biasing current, I_{bias} are chosen such that a minimum NF_{min} and a maximum MAG (Maximum Available Gain) are obtained. For the selected transistor in this design, by choosing W=54.8 μm, l=120 nm and nf=40 at I_{bias}=9 mA a low device NF_{min}=2.9 dB at 62 GHz is obtained. As the device performance is limited at mmW, a high current is required to bias the transistor.

In order to minimize the noise figure of the gain cell, Z_S (see Fig. 4.6), the impedance seen by the gate of the transistor, should be equal to Z_{opt}, the optimum noise impedance of the transistor, where $Z_{opt} = R_{opt} + jX_{opt}$. This requirement is achieved by properly choosing L_{gg}. In the designed amplifier, L_s strongly affects the stability, power gain and the center frequency of the cell and its value should be carefully modified to achieve all the design requirements.

Fig. 4.7 shows variations of the stability factor, (K), and $|S_{21}|$ with L_s versus the frequency for the single cell, respectively. Without L_s, the stability factor is less than unity and the amplifier is not unconditionally stable. It is clear that L_s decreases $|S_{21}|$ and increases stability. To design an unconditionally stable amplifier , Ls=20 pH is selected using the design guide line provided in section 3.3.4.

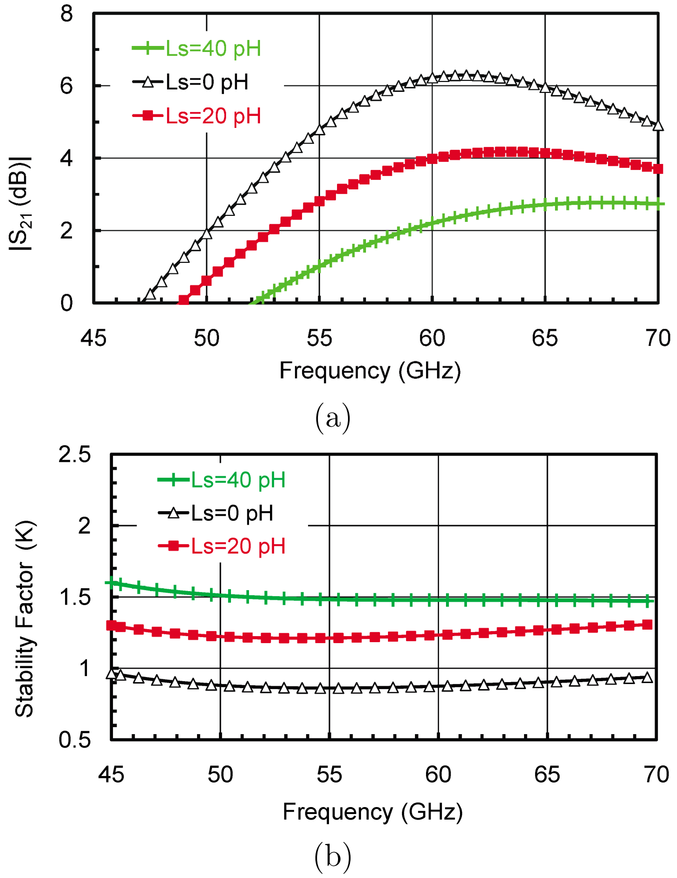

Figure 4.7: Effect of L_s in the gain cell on trade-off between (a) power gain, $|S_{21}|$ and (b) stability factor, K.

Two LNA with, L_s of 20 and 30 pH are design to obtain an unconditionally stable property and to study the tradeoff between the stability and $|S_{21}|$.

From Fig. 4.6, by expressing Z_s and equating it to Z_{opt} one obtains ($R_S = 50\Omega$):

$$Z_s = \frac{200L_g^2\omega^2}{L_g^2\omega^2 + 10000} + j\left(L_{gg}\omega + \frac{5000L_g\omega}{L_g^2\omega^2} + 10000\right) \tag{4.1}$$

or:

$$\frac{200L_g^2\omega^2}{L_g^2\omega^2 + 10000} = R_{opt}, \qquad L_{gg}\omega + \frac{5000L_g\omega}{L_g^2\omega^2} + 10000 = X_{opt} \tag{4.2}$$

From equations 4.1 and 4.2, it can be easily shown that:

$$L_g = \frac{50}{\omega}\sqrt{\frac{R_{opt}}{50 - R_{opt}}}, \qquad L_{gg} = \frac{X_{opt}}{\omega} - \frac{2500 L_g}{L_g^2 \omega^2} + 2500 \tag{4.3}$$

For example, L_s=20 pH, resulted in R_{opt}=8.7 Ω and X_{opt}=34 Ω for the selected transistor. Substituting these values into the equations 4.3, and L_g=118 pH and L_{gg}=38 pH at 62 GHz are obtained.

To show the accuracy of the above calculations, the variation of the noise figure with respect to L_{gg} is plotted at 62 GHz in Fig. 4.8. The noise figure is the lowest and quite close to the NF_{min} of the selected transistor for L_{gg}=34 pH which is close to the calculated value of L_{gg}=38 pH.

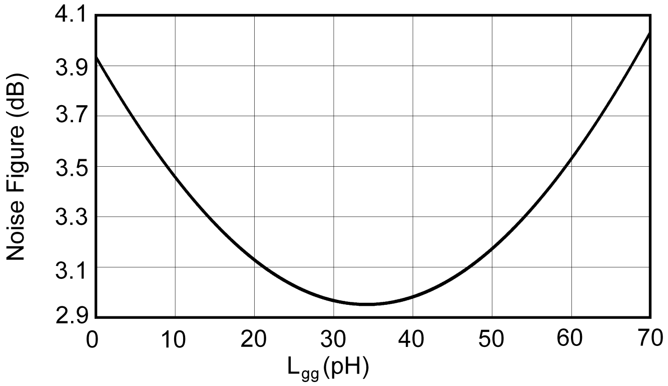

Figure 4.8: Noise figure versus L_{gg} for the designed gain cell at 62 GHz.

4.4 Design and Fabrication of a V-band CMOS SS-BPDA [5]

Many mmW CMOS amplifiers have been reported in the literature. Conventional narrow band amplifiers using different topologies such as cascode [43, 67, 75, 105–108], common source [108–112] or common gate [113] have their own advantages and disadvantages. For example, Cascode topology provides a higher stability and input/output isolation. However, it has a higher noise figure and a lower f_T and f_{max}.

For wide-band applications, Conventional Distributed Amplifiers (CDAs) are used. As discussed in chapter 3, DAs have low pass characteristics with a low gain, high power consumption and large chip foot print and therefore they are not suitable for band-pass mmW. Also, as shown in chapter 3, Conventional Band Pass Distributed Amplifiers (CBPDA) based-on low pass to band pass transformation, also has a high power consumption, large chip area and reduced performance so they are not suitable for cost-effective imaging applications although they have wide band width.

Using the gain cell and design method presented in section 4.3, a 4-stage cascaded single stage BPDA has been designed and fabricated. All inductors are realized using transmission lines, the main design parameters are TL lengths and the gate width of the transistor, W.

The schematic of the designed amplifier is shown in Fig. 4.9. Similar stages are implemented to simplify the layout. This also makes the design modular so additional stages can be easily added to increase the gain.

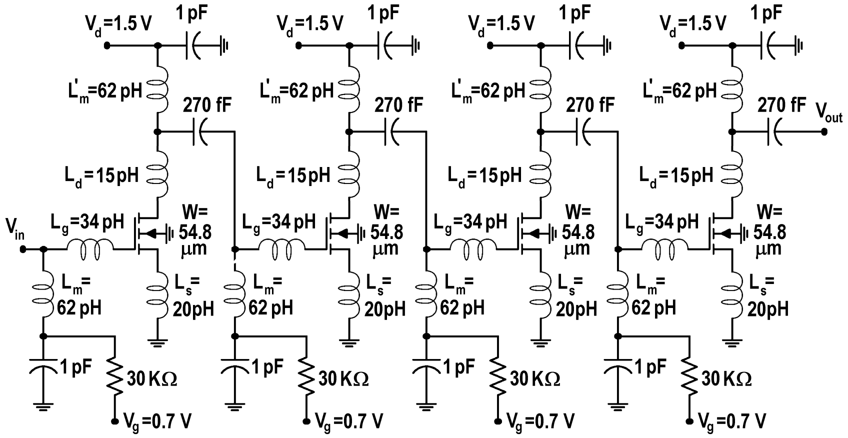

Figure 4.9: The simplified schematic of the fabricated 4-stage cascaded BPDA.

In Fig. 4.9, $L_m{}'$ and L_d are tuned for the output matching of the gain cell. All decoupling and inter-stage capacitors are 1 pF and 270 fF, respectively. The component values are subsequently re-tuned to achieve both overall design goals and layout requirements. As discussed in section, GMSLs have been implemented because of their high quality factor, high inductance per length and also scalability which results in realizing precise values of small inductors [107, 113].

To examine the effect of L_s, two identical LNAs are fabricated with different L_s

of 20 pH and 30 pH. In the final design, larger inductors, L_m=62 pH and L_m'=67 pH, are realized using MSL with lengths of 97 and 105 μm, respectively. On the other hand, smaller inductors (L_s, L_g and L_d) are constructed using the layout interconnections.

These amplifiers are fabricated using a 130 nm CMOS technology which employs a doped p-type substrate with a low resistivity of 1-2 Ω.cm. The process provides eight metal layers including three thin metal layers used to shield signals from a lossy substrate. Three thick metal layers provide a low resistive path for circuit grounding. Two RF metal layers are implemented to create high performance passive elements.

On-wafer measurements have been performed to characterize the fabricated amplifiers. Fig. 4.10 depicts the comparison between the simulated and measured data of these fabricated amplifiers. A good agreement between the simulated and measured S-parameters is evident from this figure. For L_s=20 pH and L_s=30 pH, the peak gain of 14.7 dB and 13.2 dB are achieved, respectively.

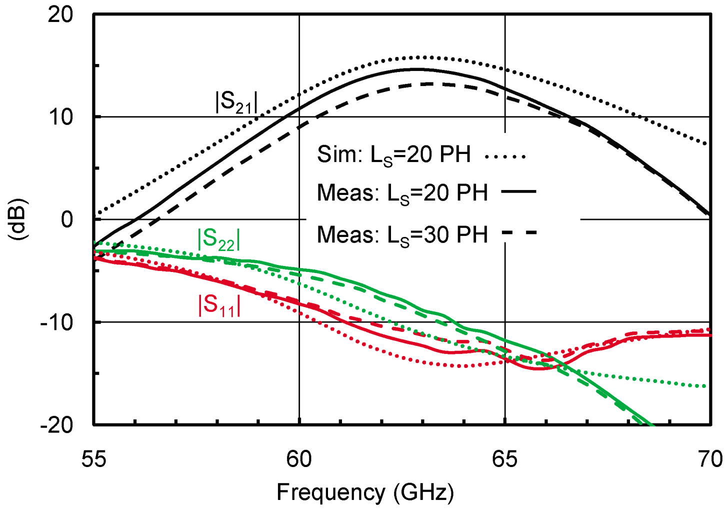

Figure 4.10: The comparison between simulated and measured S-parameters for the fabricated V-band amplifiers.

The 3 dB bandwidth of both amplifiers are 7 GHz. Measured $|S_{11}|$ and $|S_{22}|$ are less than -10 dB at 62 GHz which shows a good input/output matching for the fabricated amplifiers. The measured stability factors (K and Δ) from 55 to 65 GHz are presented in Fig. 4.11 (a). In this frequency range Δ>0 and K>1 which confirm

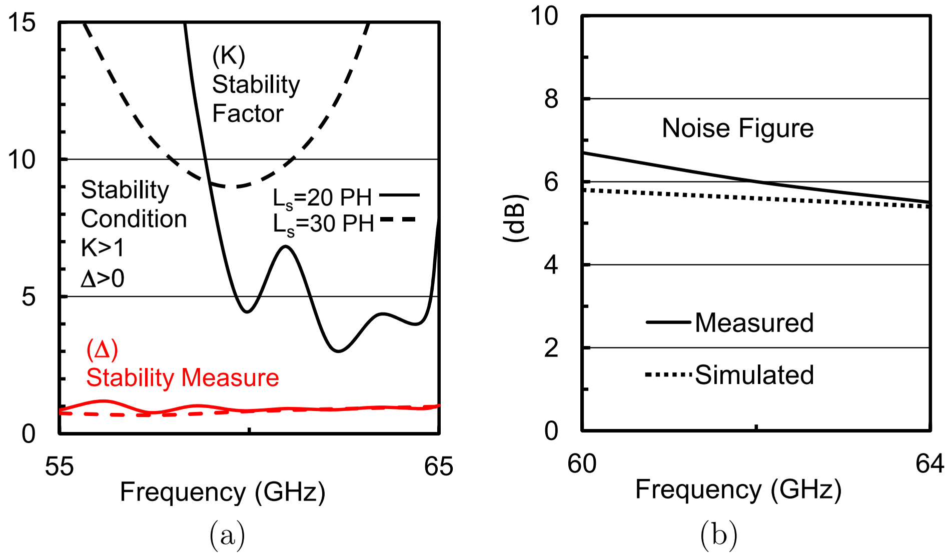

(a) (b)

Figure 4.11: (a) Measured stability parameters for different values of L_s (b) Noise figure comparison between simulation and measurement for L_s=20 pH.

the high stability [92] of the LNAs. By increasing the L_s, the stability of the LNA improves while the gain decreases.

Fig. 4.11 (b) depicts the comparison between the simulated and measured noise figure of the LNA with L_s=20 pH. The noise figure measurement is performed using a Quinstar QNS-FB15LV noise source, Centellax 65 GHz pre-amplifier, Agilent 11970 down-conversion mixer and Agilent N8973A noise figure measurement system.

Under a 1.5 V power supply, the measured input 1-dB compression point of the amplifier is -18 dBm. To measure the third intercept point of the amplifier, two tone signals at 62.5 GHz and 62.7 GHz are used and a IIP3 of -8 dBm is measured. It should be noted that due to the low quality factor of the input matching network, the amplifier is fairly wide-band and less sensitive to the process variations.

Fig. 4.12 shows the die photo of the fabricated amplifiers. The core chip size is 350 μm by 300 μm.

To achieve a higher gain, a 6-stage LNA has been designed and further optimized. Despite, the previous design which similar stages were used, in this design all the circuit components are optimized to boost the performance of the amplifier. The optimization is performed in the Agilent's Advance Design System (ADS) [114]

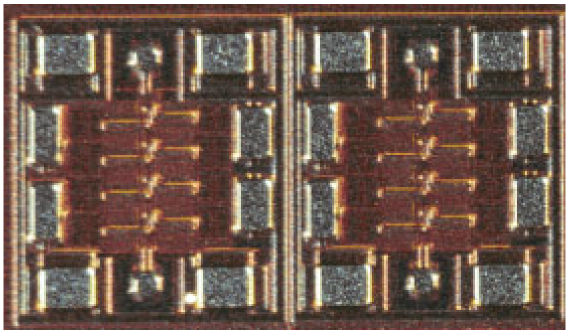

Figure 4.12: Die photo of the fabricated amplifiers.

and by using scalable models for transistor (Appendix A) and transmission line as presented in [5]. A factor combining high gain, low noise, unconditional stability, proper input and output matchings in the band of interest along with low supply power is used as the design goal.

Fig. 4.13 shows the simulated gain and input/output matching for the designed amplifier.

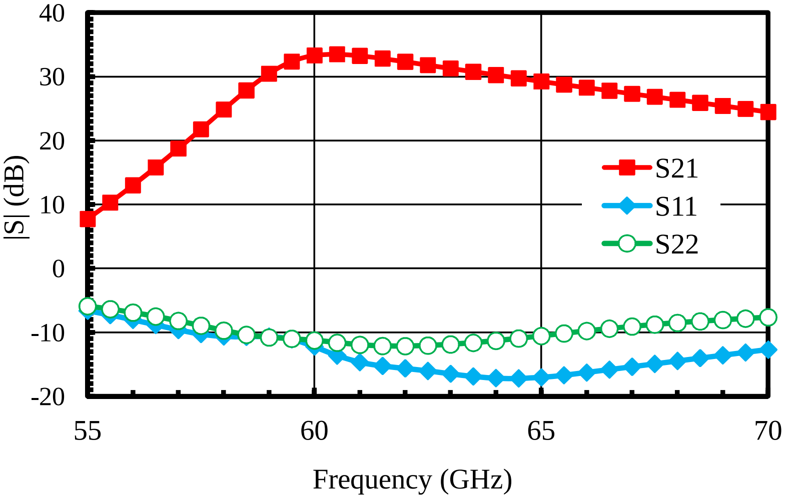

Figure 4.13: Simulated gain and input/output matching for the designed 6-stage amplifier at 60 GHz.

A maximum gain of 33.5 dB with a 3 dB bandwidth of 5 GHz from 59 to 64 GHz is obtained and input/output return losses are less than -10 dB in this frequency range while it consumes 64 mW power from a 1.6 V DC source.

Fig. 4.14 depicts the noise and stability performance of this amplifier. A noise

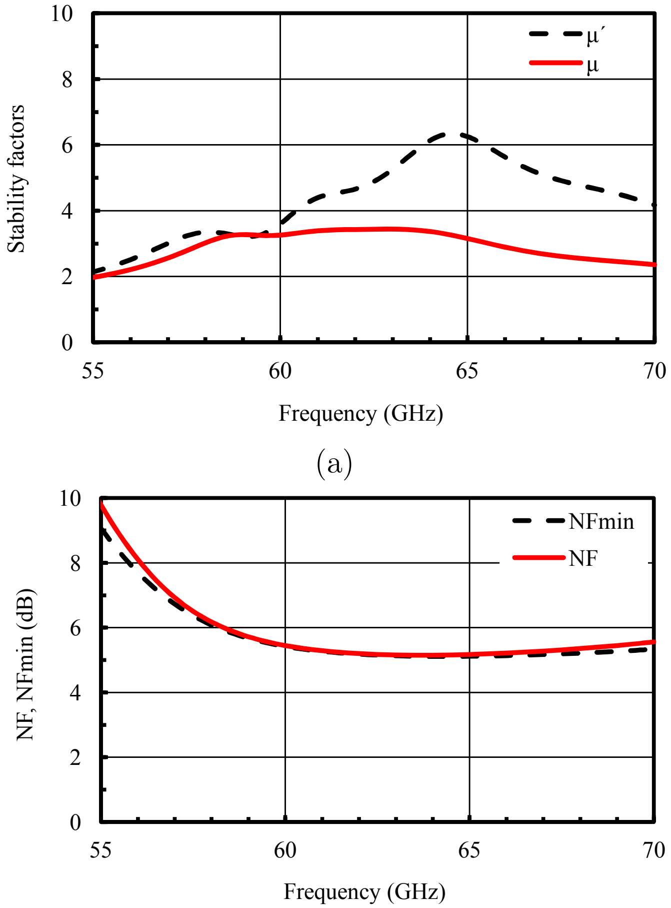

(a)

(b)

Figure 4.14: (a) Simulated stability parameters and (b) Noise performance for the designed 6-stage amplifier.

figure less than 5.5 dB and quite close to the NF_{min} is achieved. The input/output stability measures show that the amplifier is unconditionally stable at this frequency band.

To compare the performance of the designed and fabricated amplifiers with the state-of-the-art CMOS technology, an amplifier figure of merit (FOM) is defined. This FOM takes into the account the gain, G, band-width, BW, noise factor, F, core chip area, A, power consumption, P and a normalized cost factor, C. This cost factor is the cost for chip fabrication per unit area normalized to that of the most expensive technology in the table:

$$FOM(GHz/nmW) = \frac{G(number).BW(GHz)}{(F-1).A(mm^2).P(mW).C} \tag{4.4}$$

It should be noted that in equation 4.4, G and F, are numbers (not in dB). Table 4.1 compares the performance of the designed and fabricated LNAs with those recently reported in the literature using this FOM.

Table 4.1: Performance comparison of the designed and fabricated LNAs to the prior art.

Process	45 nm	90 nm	90 nm	130 nm	130 nm	130 nm	130 nm	130 nm
Gain (dB)	13.4	12.55	14	12	21	14.7	16	33.5
BW (GHz)	11	10	10	14	4.5	7	8	5
NF (GHz)	5.6	6.55	5.7	8.8	8.3	6	5	5.3
P_{DC} (mW)	95	60	27	54	15.1	64.8	42.7	64
Area (mm^2)	0.36	0.4	0.57	0.76	0.4	0.105	0.105	0.15
Cost factor	1	0.42	0.42	0.2	0.2	0.2	0.2	0.2
FOM	2.7	5	14	4	81	51	164	1300
Year	2008	2010	2005	2005	2011	Meas.	Sim.	Sim.
Reference	[105]	[115]	[109]	[106]	[107]	4-stage	4-stage	6-stage

As seen from Table 4.1, a high performance LNA with a high FOM of 51 is achieved using the measured data for the fabricated 4-stage LNA. The measured FOM is less than the simulated one for the 4-stage LNA due to its lower gain and bandwidth and higher noise figure and power consumption.

Also, the simulation results predict an outstanding performance for the designed 6-stage LNA. The considerable improvement in the simulated FOM for the 6-stage LNA compared to that of the 4-stage one is as a result of the increased overall gain of this LNA. It should be implied that the gain in equation 4.4 is a number, therefore, a 3 dB increase in gain will double the resulted FOM.

4.5 CMOS Amplifiers Which Can Operate Above f_T

The goal of this section is to investigate the capability of the proposed topology and presented design methods to realize CMOS amplifiers for operation at the frequencies above the f_t of technology. In [108], it is shown that the actual transistor figure of merit is the f_{max} of the device rather than the f_t. In 130 nm CMOS technology, f_t is around 75 GHz while the f_{max} exceeds 100 GHz.

In frequencies above the f_t, the device is unconditionally stable and the design task will be easier. W-band BPDAs are designed and fabricated using the presented design method in 130 nm CMOS technology. A 77 GHz amplifier is optimized for input/output matchings, high gain, low power consumption and low noise properties using 6 cascaded single-stage BPDA topology.

Fig. 4.15 shows the S-parameters of the design W-band amplifier which needs a 1.5 V supply and consumes 69 mW power.

A 28 dB maximum gain is achieved at 75 GHz with a 3 dB bandwidth of 5 GHz from 74 to 79 GHz while input/output matchings are better than 8 and 13 dB in this frequency band.

Simulated stability parameters (μ and μ) from 70 to 90 GHz are presented in Fig. 4.16 (a). In frequencies above the f_T of the transistor, the amplifier is unconditionally stable and there is no need to insert any source degeneration inductors which is the case here. Fig. 4.16 (b) depicts simulated noise figure and NF_{min} for this amplifier. The noise figure of less than 7 dB quite close to the NF_{min} is achieved at 77 GHz which shows that the noise matching is properly implemented at this frequency.

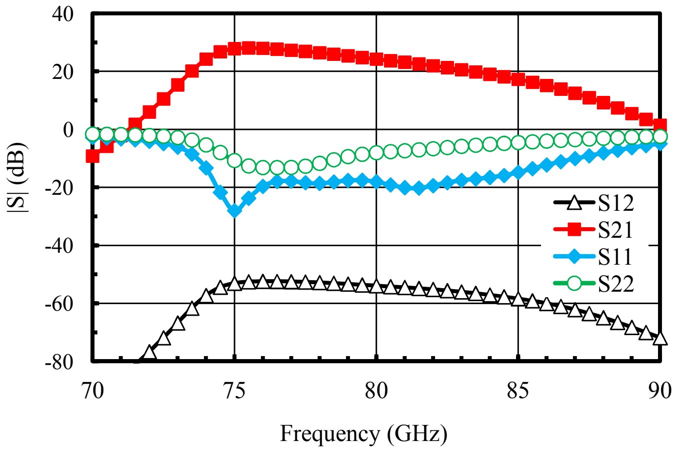

Figure 4.15: Measured S-parameters for the designed W-band amplifiers.

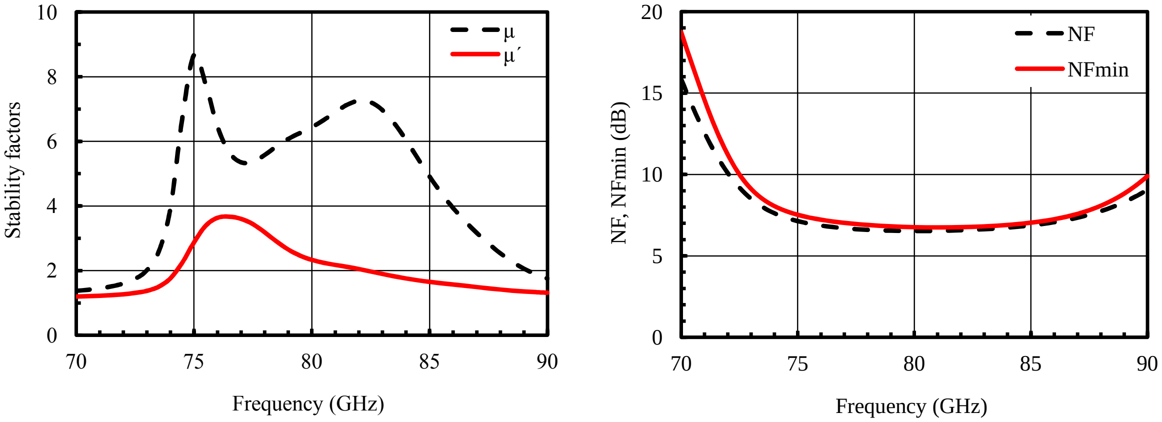

(a) (b)

Figure 4.16: (a) Simulated stability parameters and (b) noise characteristics for the W-band designed amplifier.

A 85 GHz amplifier is implemented using 4 cascaded single-stage BPDA topology. Fig. 4.17 (a) and (b) compare its simulated and measured power gain and reverse isolation, respectively. The amplifier consumes 54 mW with a 1.8 V power supply. A 10 dB maximum gain and a reverse isolation better than 39 dB are obtained at 82 GHz with a measured 3 dB bandwidth of 11Ǵ Hz from 80 to 91 GHz. From this figure, there is a good agreement between simulated and measured results.

Simulated and measured input and output matching of the fabricated amplifier are shown in Fig. 4.18. The input and output matchings are better than 8 and 10 dB from 80 to 91 GHz and an excellent agreement between simulation and measurement

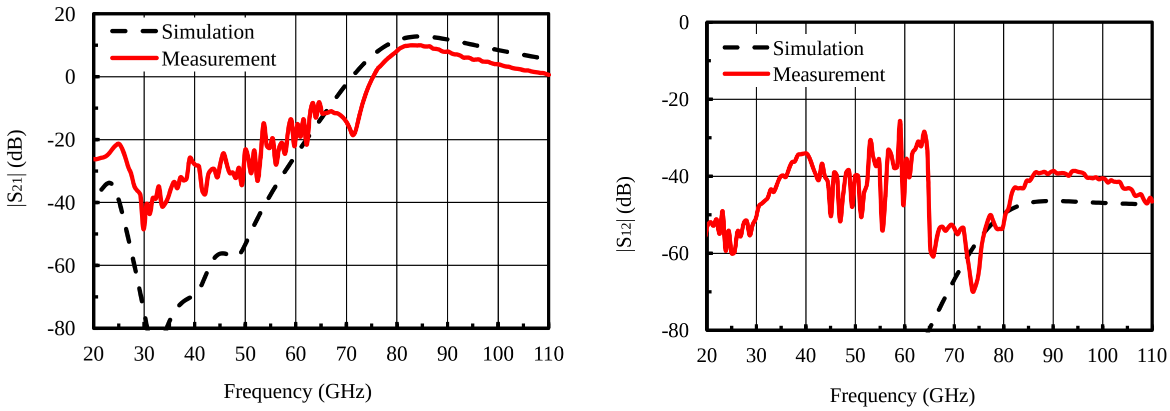

(a) (b)

Figure 4.17: Comparison between simulated and measured results for the fabricated 85 GHz amplifier for its (a) power gain and (b) reverse isolation.

is clear from this figure.

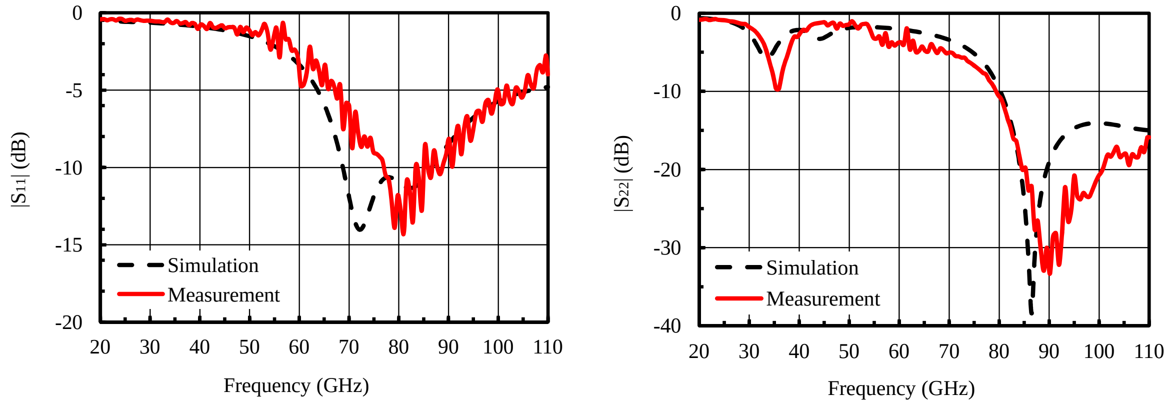

(a) (b)

Figure 4.18: Comparison between simulated and measured matchings for the fabricated 85 GHz amplifier for (a) input and (b) output.

The core chip size is 300 μm by 200 μm. Fig. 4.19 shows the die photo of the fabricated 85 GHz amplifiers.

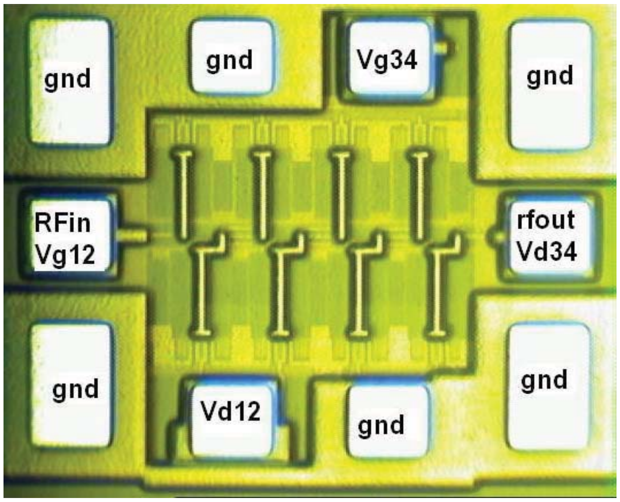

Figure 4.19: Die photo of the fabricated 85 GHz amplifier.

4.6 A Multi-Stage BPDA for Wide-Band MmW Applications

So far, Single Stage BPDAs (SSBPDA) have been studied. It was shown that the SSBPDAs are very good candidates for implementation of high performance mm-wave LNAs. Depending on the design parameters and the fabrication technology, in practice, about 10% band width is achievable using SSBPDAs which is sufficient for many mmW applications such as 60 GHz wireless communication and 77 GHz car radar. However, for imaging applications, a wider band width may be required as the benefit of the wide band-width for imaging application was discussed in chapter 2. This can be achieved using a multi-stage BPDA with the circuit schematic shown in Fig. 4.20.

Similar to the CDA, multiple inductors are implemented in the artificial gate and drain lines, however, as opposed to the conventional DA, 50Ω terminations are replaced with short circuits to create standing waves in the artificial gate and drain lines. This will result in a band pass behavior as opposed to the low pass behavior of the conventional DA. Moreover, by removing the lossy and noisy terminations, the gain and noise performance of the circuit will be improved.

In contrast with the DA and the SSBPDA, the voltage transfer function of a multi-stage BPDA is complicated and cannot be expressed in a closed form formula,

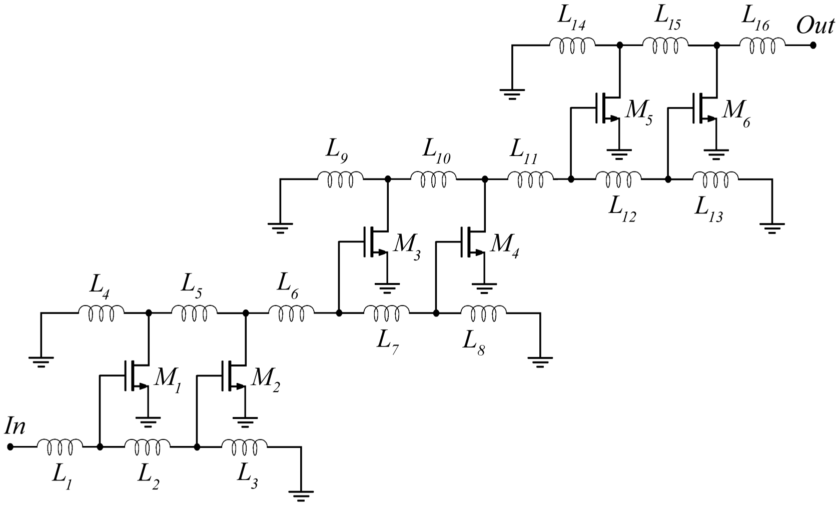

Figure 4.20: The simplified schematic of the designed multi-stage BPDA consisting of three cascaded of a 2-stage BPDA.

therefore, simulation tools are used to analyze the multi-stage BPDA performance. In Fig. 4.20, all inductors are realized with a piece of transmission line and their lengths are optimized along with the width and bias values of the transistors. Fig. Fig. 4.21 shows simulated S-parameters of the designed multi-stage BPDA.

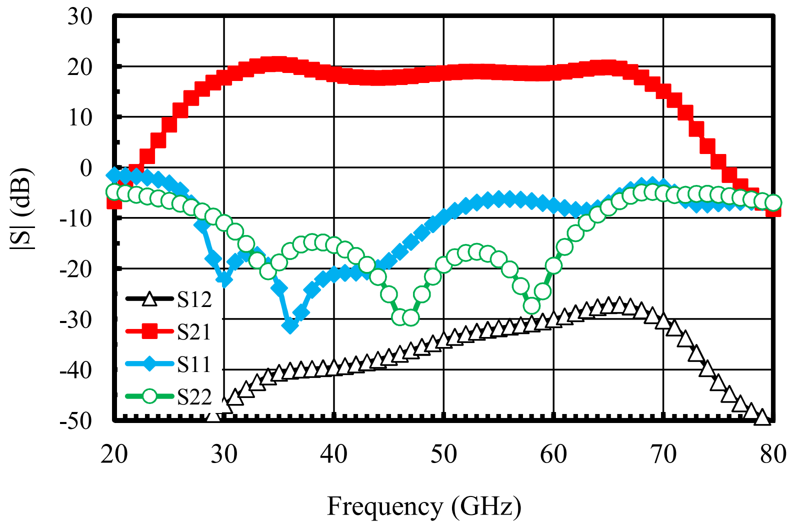

Figure 4.21: Simulated S-parameters for the designed multi-stage BPDA.

Fig. 4.21, shows that a maximum gain of 20.5 dB with a considerable 3 dB bandwidth of 38 GHz from 30 to 68 GHz is achieved while input/output return losses are less than 6 dB in this frequency range which can be further improved by adding m-derived matching circuits in the input and output of the amplifier [116].

Fig. 4.22 shows the simulated noise figure, NF_{min} and stability measures for this amplifier. Noise figure is better than 6 dB in the whole bandwidth and closed to the NF_{min} and the amplifier is unconditionally stable in this frequency range.

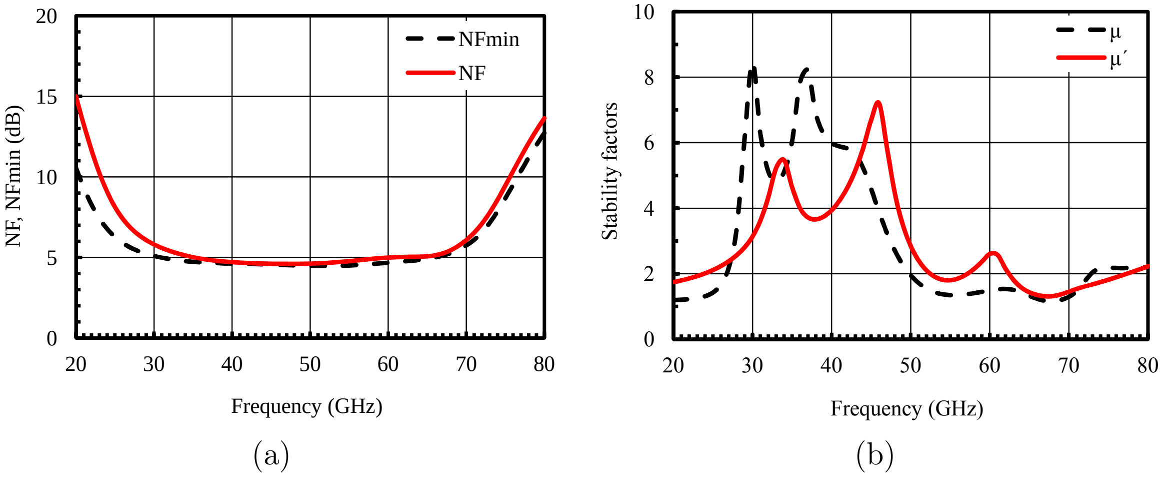

(a) (b)

Figure 4.22: Simulated noise figure, NF_{min}, input and output stability measure (μ and $\acute{\mu}$ for the designed multi-stage BPDA.

Using the amplifier figure of merit presented in section 4.4, a performance comparison is made between the designed amplifier and the state of the art wide band mmW CMOS amplifiers and is shown in Table 4.2:

In this Table, the normalized cost factor is calculated to be 1, 0.42 and 0.1 for 90 , 130 nm and 180 nm CMOS technologies, respectively, as explained in section 4.4. For FOM calculation, a 7 dB noise figure is used for the papers who did not reported their noise figure.

4.7 Conclusion

Design for minimum noise for a BPDA is first studied in this chapter. Then, the fabrication of a 60 GHz amplifier using a low cost 130 nm CMOS technology is presented. A good agreement between the simulated and measured S-parameters is achieved. The measured results shows a peak gain of 14.7 dB at 62 GHz with a 3 dB bandwidth of 7 GHz. Measured $|S_{11}|$ and $|S_{22}|$ are less than -10 dB at 62 GHz.

Table 4.2: Performance of the recently published CDAs in the literature using different fabrication technologies.

Process	Technology	$\lvert S_{21}\rvert$ (dB)	3dB BW (GHz)	Power cons. (mW)	Chip area (mm^2)	Noise Figure (dB)	Figure of Merit	Year Ref.
180 nm CMOS	Modified 8-stage DA	4	39	140	3	7	0.5	2004 [63]
130 nm CMOS	4 cascaded Cascode DAs	8.5	40	135	1.76	7	1.5	2008 [67]
130 nm CMOS	Loss compensated 8-stage DAs	9.8	43.9	103	1.5	7	3.4	2009 [68]
90 nm CMOS	Cascaded multi-stage DA	7	70	122	1.28	7	1.3	2005 [71]
90 nm CMOS	Tapered cascaded multi-stage DA	14	73.5	84	1.72	7	7.6	2008 [72]
180 nm CMOS	High pass TLs Conventional BPDA	6.4	22	64.8	0.17	9.1	12.2	2008 [80]
130 nm CMOS	The proposed multi-stage BPDA	20.5	38	64.8	0.048	6	514	This Work (Sim.)

The amplifier noise figure is measured using a custom made mmW set-up and is measured to be 6 dB at 60 GHz which is in agreement with the simulation results. Using a 1.5 V supply, the measured output 1-dB compression point of the amplifier is -18 dBm and the gain of the amplifier is 14 dB at 62.5 GHz. The measured IIIP3 is -8 dBm. The fabricated LNA chip size is 350 μm by 300 μm.

To obtain a higher performance, a 6-stage LNA is designed and optimized. Simulations show a maximum gain of 33.5 dB with a minimum noise figure of 5.3 dB. The amplifier has a 3 dB bandwidth of 5 GHz from 59 to 64 GHz and the input/output return losses are less than -10 dB in this frequency range while it consumes 64 mW power from a 1.2 V DC source.

Also, high gain amplification at frequencies above the cut-off frequency of the technology, f_T, is demonstrated by design and fabrication of amplifiers at the W-band. The fabricated LNA achieves a peak gain of 10 dB at 82 GHz. The measured 3 dB bandwidth is 11 GHz from 80 to 91 GHz and measured input/output matchings are better than 10 dB in this band. The designed LNA achieves a peak gain of 28 dB at 75 GHz and a 3 dB bandwidth of 5 GHz. The simulated input/output matchings are better than 15 and 6 dB in this bandwidth, respectively. The simulated noise figure is better than 7 dB and quite close to the NF_{min} of the circuit which shows a good noise matching for the designed LNA.

A LNA figure of merit is defined to compare the performance of the fabricated and designed LNAs with the state of the art. The amplifiers realized using the proposed architecture and design strategy and demonstrate a simulated and measured FOM of 51 and 164 for the 4-stage LNA. The outstanding FOM of 1300 is simulated using the 6-stage designed LNA.

A multi-stage BPDA is also designed using a low cost 130 nm CMOS technology. A maximum gain of 20.5 dB with a considerable 3 dB bandwidth of 38 GHz from 30 to 68 GHz is achieved while the noise figure is better than 6 dB , which is quite close to NF_{min}, in the whole frequency bandwidth.

Chapter 5

MINIATURIZED, LOW COST ROTMAN LENS FOR MILLIMETER WAVE APPLICATION

5.1 Introduction

Rotman lens due to its wide band, wide scan angle and true time delay properties has been widely used in microwave systems since its invention in 1962 [117]. However, it has a poor performance at the mmW as its metallic, dielectric and radiation losses increase at higher frequencies.

In this chapter, design of highly efficient microwave and mmW Rotman lenses are presented following a short review of beam forming networks. For the first time, a few lenses are designed and optimized by choosing a very small Focal Lens Ratio (FL) and implemented on low cost substrate. The lens transmission lines are implemented by conventional microstrip and striplines, due to their ease of fabrication and acceptable insertion loss, respectively.

5.2 Beam Forming Techniques

Special multi-path effects and significant path loss highly degrade signals at mm-wave. Therefore, beam forming (beam steering) systems are very attractive for mmW applications. The current distribution on an antenna or an array of antennas determines the radiated field. In an array, both the phase and magnitude of the current fed to each element can be controlled to create the required beam. The required feeding currents are generated by a circuit which is often called a beam forming network.

The beam forming systems are conventionally used for high performance passive microwave imaging or RADAR applications; however, an extensive range of emerging mass market applications require low cost mmW phased array architectures and enabling cost-effective technologies. In military applications, to achieve a fine spatial resolution, thousands of elements are employed [51,118]. Such complex and expensive technologies obviously are not suitable for recent commercial mmW applications such as 94 GHz imaging systems for safety, security, or surveillance, 77 GHz car RADAR or 60 GHz short range high throughput wireless communication; therefore low cost active and passive technologies should be employed to implement the front-end. One optimum solution is to implement the active parts using the low cost silicon integrated circuit technology and integrate the fabricated chips with high quality passive components realized on a low cost high performance passive substrate.

The RF beam forming techniques are performed either using a reflector, lens or circuit beam formers. Circuit beam formers such as Blass [119] and Butler [120] matrices use transmission line as a phase shifter to produce beam scanning. Different transmission line lengths produce the required phased shift and in combination with power splitters and couplers form a multiple beam network.

The Blass matrix uses transmission lines and directional couplers to form beams using time delays and therefore it is suitable for wide band applications. However, it has a considerable amount of insertion loss due to the presence of the line terminations, so it has limited applications.

The Butler matrix uses transmission lines, hybrids and phase shifters to produce orthogonal beams. It is very popular in microwave RADAR and satellite systems due to its low loss and easy implementation. However, as the phase shift is frequency dependent, its beam widths and beam angles vary with frequency and therefore it is suitable for narrow band applications.

Hybrid lenses and reflector are other types of beam former to produce high gain, high directivity beams in small scan range provided by system of reflectors or lenses [118]. However, they very large and not suitable for low profile systems. Wide angle circular scanning can be achieved using the Luneburg or geodesic lenses [7]. Table 5.1 compares some of the representative performances of different beam forming approaches [7].

Table 5.1: Summary of the typical performance characteristics of the microwave beam-forming systems [7].

Beam former type	Typical scan range	Typical aperture size	Typical side-lobe level for multiple beam	Band-width capability	Typical efficiency at microwave [a]	Element use factor
Rotman lens	±45° (linear) 360° (circular)	10λ	-20 dB	4:1	>63%	1
Hybrid lens	±10° for 1.2° beam-width	130λ	-16 dB	-	>60%	1.5
Graded index lens	360°	20λ	-13 dB	9:1	-	1
Hybrid reflector	±30°	230λ	-22 dB	-	>76%	1.46
Blass matrix	±60°	15λ	-13 dB	$<$ 1%	75%	1
Butler matrix	±60°	16λ	-13 dB	$>$ 2:1	40%	1

[a] At mmW efficiency is much lower.

Scan range is depend on bandwidth and aperture size of the system. Wide scan range requires small size system whereas large aperture leads to a limited scan angle and the trade-offs between the size and bandwidth can be made. The large size and the weight of solid dielectric lenses, make them unsuitable for low profile applications but they maybe considered for some mmW and THz systems. [121]. Metal parallel plate lenses reduce this problem using Ruze lens [122], bootlace lens [123], Rotman lens [117] or R-KR lens [124]. These types of lenses are approximately 10 times smaller than solid dielectric lenses [7].

The solution proposed by the present research is to use Rotman lens as the beam former due to its wide band, wide scan angle and true time delay properties along with its low cost, low profile and ease of fabrication nature. Rotman lens allows the systems to simultaneously see targets in multiple directions (mutli-beam capability) without physically moving the antenna system.

5.3 Rotman Lens for Beam Forming

Rotman lens is a planar M input by N output device employed as a beam forming network for switched beam or multi-beam antennas [117]. Scanning without phase shifter or power divider considerably reduces the fabrication costs. Conventional Rotman lens are realized in waveguide or printed circuit board. The other advantages of Rotman lens are lower loss, high power handling, reduced dimensions, wide scanning angle and large frequency band operation.

Figure 5.1 shows top view of a Rotman lens. It consists of an air filled parallel plates region which is bounded on the left by a circular profile called focal arc and an array port curve on the right. The center of the focal arc is located at $(-G + R, 0)$ and its radius is R. The M input ports lie on focal arc ($F_0, F_1, F_2, ...$ points), whereas the N radiating elements are located on the straight profile called array plane. N transmission-lines of length $W_n (n = 1, 2...N)$ connect the P points on array port curve to the corresponding radiating elements on array plane. The beam forming is achieved by switching among the M input ports [125].

F_0, F_1 and F_2 are the perfect focal points. By feeding the lens from these points, a phase-error free excitation is generated at the antenna radiating element, with steering angles of 0, $+\varphi$ and -φ, respectively. The design equations simply consist of conditions imposed on three rays from F_0, F_1 and F_2 to the radiation elements at the array plane having the same electrical length, apart from the contribution required for the beam tilting in the 0, $+\varphi$ and -φ directions, respectively.

The lens parameters and the procedure to derive parallel plate lens design equations are presented at Appendix B. Rotman lens is conventionally used in RF and microwave systems. However, at mmW due to its radiation and the increasing material losses, its efficiency considerably drops. Next section describes the design and fabrication of a high efficiency mmW Rotman lens.

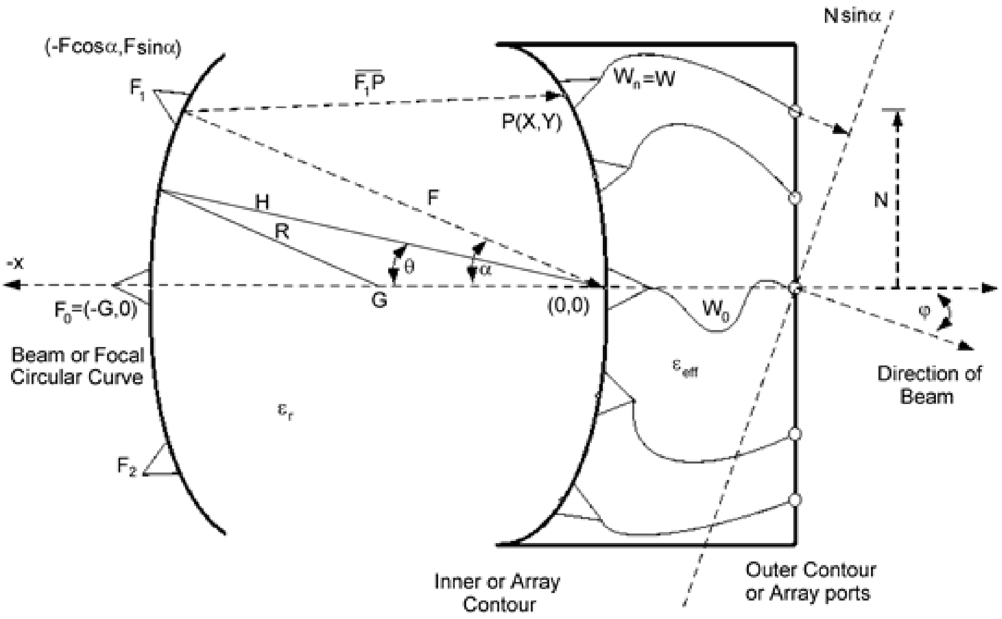

Figure 5.1: Diagram of a Rotman lens [11].

5.4 Miniaturized Rotman Lens for MmW Imaging Systems

The efficiency of the fabricated Rotman lens reported in the literature is usually less than 30% at microwave frequencies [126–130]. Substrate Integrated Waveguide (SIW) lenses have been reported with a slightly higher efficiency , however, their fabrication is costly and not suitable for a cost effective solution [131–134]. At mmW, due to increasing material and radiation losses, the efficiency is expected to be much smaller.

In this work, a low loss Rotman lens design is designed using a very small lens size and by implementing a low loss cost-effective substrate such as Alumina in the lens. In the conventional lens design, the lens diameter which is known as the focal ratio is in the order of 10 λ_0 or more. However, when the number of the lens ports is limited, the lens can be designed in a much smaller size in order to reduce its insertion loss.

Different type of wave-guides can be used to implement the lens and its connection to the ports. Optimum designs are achieved using microstrip line (MSL) and strip line.

5.4.1 Microstrip line for mmW Rotman lens

Microstrip line is one of the simplest transmission line structures and can be easily implemented on many processes. The MSL is made of two metallic conducting plates coated on an insulating material such as Alumina, fiber glass or polystyrene. This insulated plate works as a dielectric in the MSL. Usually the top metal is called the signal line and the bottom metal is called the ground plane. To reduce the conducting loss, a low loss metal such as copper, gold or Aluminum is used. Other than the conducting loss, dielectric loss and radiation loss are two other important sources of loss in MSL. The radiation loss tends to increase using a thicker substrate. Therefore, the substrate thickness should be kept very small compared to the wavelength to minimize the radiation loss in MSL.

Because of its planar nature, MSL can be easily integrated with other parts of the system such as antenna and the MMIC chips. It also has a good mechanical stability, heat transfer properties and low weight. Figure 5.2 shows the structure, main parameters, the Electric and Magnetic field lines for fundamental Quasi-TEM mode in an MSL.

The MSL is a common transmission medium for the Rotman lens implementation. However, at the mmW due to the increase in metallic and dielectric losses the efficiency of the lens is considerably decreased. Therefore, very low loss dielectric substrates such as Alumina are the only feasible substrate for mmW Rotman lens realization. Also, to obtain the required characteristic impedance (usually 50 Ω), the substrate should have a proper dielectric constant and thickness to result in a proper line width, W. If the resulted W is too narrow, the metallic loss will increase and if it is too wide, it will cause the cross-talk between adjusted TLs in the lens or higher mode excitation. Also, if the dielectric constant is low, the radiation loss will increase.

Using a substrate with a large dielectric constant in Rotman lens design has certain advantages. Firstly, it strongly confines field inside the dielectric material and reduces the radiation loss. Secondly, it reduces the circuit size. MSLs support the quasi-TEM mode which means it has non-zero fields in the direction of propagation. This is not desired as it may excite the lossy higher order modes in very high frequencies.

In this work, MSL Rotman lenses are designed using Roger RT 3010 substrate

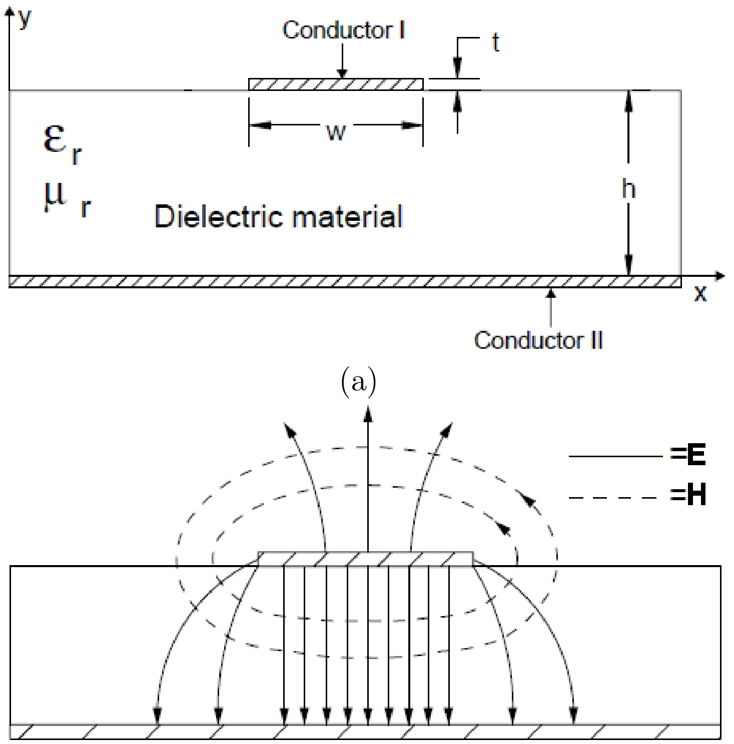

(a)

(b)

Figure 5.2: Microstrip line. a)The structure and main parameters. b) the Electric (E) and magnetic (M) field lines. [12]

with 0.635 mm thickness, loss tangent of 0.0023 and dielectric constant of 10.2 with copper cladding with the center frequencies of 15 and 30 GHz and Alumina substrate with 0.635 mm thickness, loss tangent of 0.0001, dielectric constant of 9.8 and gold metal plates with the center frequencies of 77 GHz.

5.4.2 Stripline for mmW Rotman lens

Stripline requires a conducing signal line sandwiched between two grounded dielectric layers on both sides. Therefore, it is a multi-layer structure and requires a more complicated process for its fabrication compared with that of MSL. Figure 5.3 shows the structure, main parameters, the electric and magnetic field lines for the fundamental TEM mode in a stripline.

TEM modes wave propagation means both electric and magnetic fields are perpendicular to the direction of propagation. As opposed to microstrip, stripline has

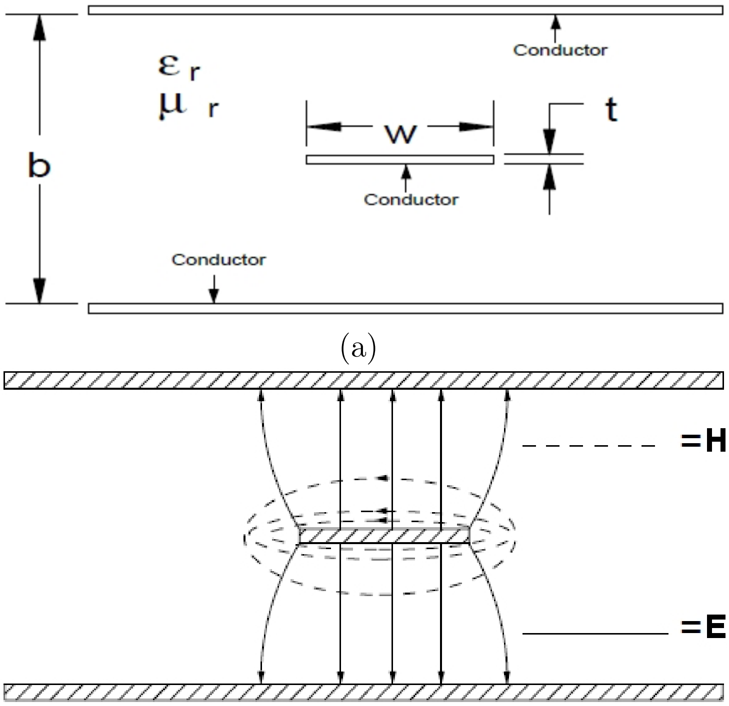

(a)

(b)

Figure 5.3: Stripline. a)The structure and main parameters. b) the Electric (E) and magnetic (M) field lines. [12]

no radiation loss as the whole field is confined between the ground planes and inside the dielectric material. Another advantage of stripline over microstrip is that it is non-dispersive and also the signal is shielded from the outside interference.

However, as compared to MSL, stripline is more difficult and expensive to be fabricated, and because of the second ground plane, the strip widths are much narrower for a given impedance and thicker compared to a MSL.

In this work, in addition to the designed MSL Rotman lenses, stripline Rotman lenses are also designed using Roger RT 3730 substrate with 0.762 mm thickness, loss tangent of 0.0009 and dielectric constant of 3 with copper cladding and Alumina substrate with 0.635 mm thickness, loss tangent of 0.0001 and gold metal plates with the center frequencies of 60 and 77 GHz, respectively.

In designing a stripline Rotman lens, the top and bottom ground plane should have the same potential to prevent the propagation of parallel plate mode in the lens. If this mode is generated, it can propagate wherever the ground planes exist and will not remain confined to the region near the strip. To prevent the propagation of parallel plate mode in stripline lens, proper via holes should be implemented to connect the top and bottom ground layers. At higher frequencies TE and TM modes may propagate inside the stripline which is called an over-moded wave-guide. This may cause signal distortion or other undesired effects.

5.4.3 Design of miniaturized mmW Rotman Lenses

In order to demonstrate the feasibility of this method to design low loss and low cost mmW lens, several 4 by 4 parallel plate Rotman lenses have been first designed. Very low loss Alumina and conventional Printed Circuit Board (PCB) substrates at the microwave and mmW frequencies are used. Table 3-2 shows the design parameters and the achieved performances for the designed lenses.

For lower frequencies, Roger RT 3010 with a 0.635 mm thickness, loss tangent of 0.0023 and dielectric constant of 10.2 is used. Two designs at 15 and 30 GHz are optimized to achieve minimum insertion loss. Microstrip transmission lines are implemented at all the beam, array and dummy ports. Simulations show 10 GHz bandwidth for both lenses and average insertion loss of 3 and 3.5 dB for the 15 and 30 GHz lenses, respectively. For both lenses, the focal length (FL) to the wavelength ratio of two is used and the focal ratio around 1 is used to achieve a circular lens shape. As shown in Table 5.2, lenses have very small dimensions and weight.

Figure 5.4 shows the simulated electric field distribution of the designed MSL lens at 15 GHz. The simulation is performed using the Ansoft HFSS full wave EM simulator. In Figure 5.4, the incoming radiation with a 30° angle of arrival, creates a 120° phase shift in the wave propagated in each of the adjacent array port transmission lines. The waves that radiate into the lens are summed up constructively in the beam port corresponding to a 30° radiation angle.

Also, a stripline Rotman lens using very low loss Alumina substrate with the center frequency of 77 GHz has been designed and simulated. The lens has 6 array ports, 7 beam ports and is designed to cover a 42° scan angle with the standard normalized element spacing of 0.5 (d=$0.5\lambda_0$). An Alumina substrate with very low dielectric loss, 0.635 mm thickness, and a dielectric constant of 9.8 is used to provide both proper physical and electrical properties for the designed lens.

Table 5.2: The lens parameters for some of the designed mmW Rotman lenses.

Physical lens parameters	Substrate material properties	Electrical properties	Dimensions and weight	Number of ports	Average insertion loss
Microstrip Circular FL/λ=2 g=1.03	Roger 3010 $\tan\delta$=0.0023 ϵ_r=10.2 d=0.635 mm	f_0=15 GHz BW=10 GHz η/λ=0.5 2α=70°	Lenght=39.2 mm Width=35.5 mm Weight=3.3 gr Figure 5.4	Array=4 Beam=4 Dummy=4 Total=12	3 dB
Microstrip Circular FL/λ=2 g=1.01	Roger 3010 $\tan\delta$=0.0023 ϵ_r=10.2 d=0.635 mm	f_0=30 GHz BW=10 GHz η/λ=0.5 2α=36°	Lenght=17.6 mm Width=19.4 mm Weight=0.8 gr	Array=4 Beam=4 Dummy=2 Total=10	3.5 dB
Stripline Circular FL/λ=1.2 g=1	Roger 3730 $\tan\delta$=0.0009 ϵ_r=3 d=0.762 mm	f_0=60 GHz BW=10 GHz η/λ=0.5 2α=70°	Lenght=9.6 mm Width=8.5 mm Weight=0.8 gr	Array=4 Beam=4 Dummy=0 Total=8	3 dB
Stripline Circular FL/λ=2.5 g=1.03	Alumina $\tan\delta$=0.0001 ϵ_r=9.8 d=0.64 mm	f_0=77 GHz BW=10 GHz η/λ=0.5 2α=40°	Lenght=9.9 mm Width=9.3 mm Weight=0.12 gr Figure 5.5	Array=6 Beam=7 Dummy=4 Total=17	7 dB
Microstrip Circular FL/λ=1.8 g=1	Alumina $\tan\delta$=0.0001 ϵ_r=9.8 d=0.635 mm	f_0=77 GHz BW=10 GHz η/λ=0.5 2α=70°	Lenght=6 mm Width=5.9 mm Weight=0.1 gr Figure 5.7	Array=4 Beam=4 Dummy=4 Total=12	4.5 dB

Figure 5.5 shows the diagram of the designed lens. The design is based on a small focal length ratio of 2.5 which reduces its insertion loss and allows a very low profile design. The lens dimensions are less than 1 cm.

Figure 5.6 shows the simulated insertion loss for the designed Rotman lens. An average insertion loss of 7 dB is achieved while the amplitude error is less than 1 dB as can be seen from this figure.

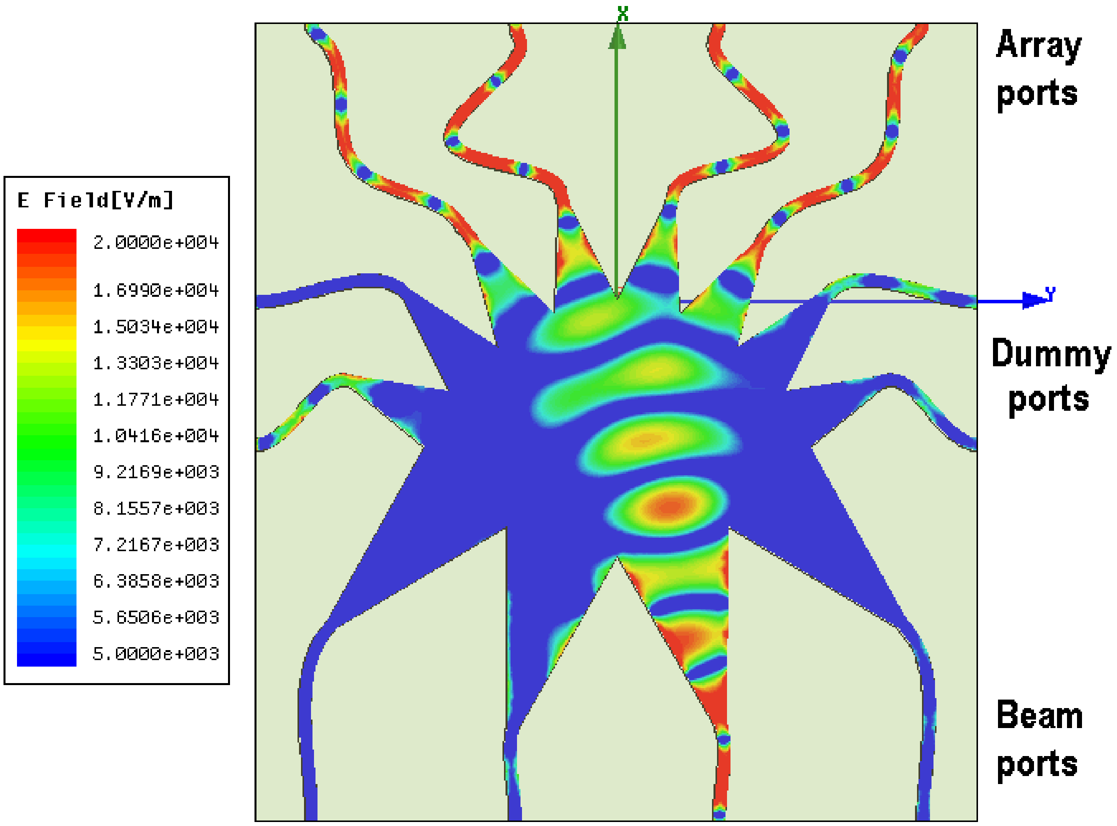

Figure 5.4: Simulated Electric field distribution for the designed 4 by 4 lens on a Roger 3010 substrate at 15 GHz.

5.4.4 Design and fabrication of miniaturized Rotman Lens at 77 GHz

Figure 5.7 shows the simulated field distribution across the designed 77 GHz microstrip lens on an Alumina substrate. In this lens a 39° radiation angle creates a 120° phase shift in the wave propagated in each of the adjacent array port transmission lines and the waves are added up constructively at the corner beam port.

This microstrip lens has been fabricated. Figure 5.8 shows the photo of the fabricated 77 GHz Rotman lens. The lens is fabricated on the Alumina substrate by the standard fabrication process. A gold electroplating layer with a 2 μm thickness is used for MSL top metal. A CPW to microstrip transition has been designed in order to measure the lens performance using a mmW probe station setup.

The fabricated lens is mounted on a gold substrate and bond wires are used to

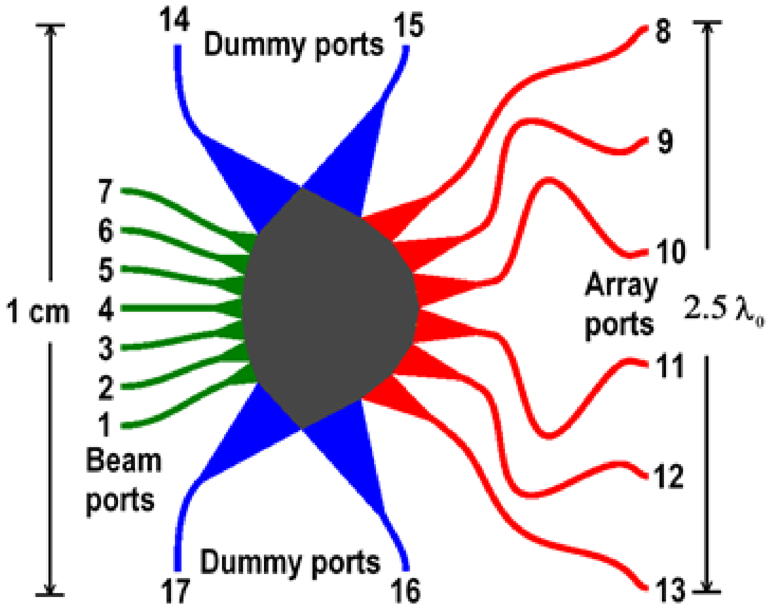

Figure 5.5: The diagram of the designed miniaturized 77 GHz stripline Rotman lens with 6 array ports and 7 beam ports on an Alumina substrate.

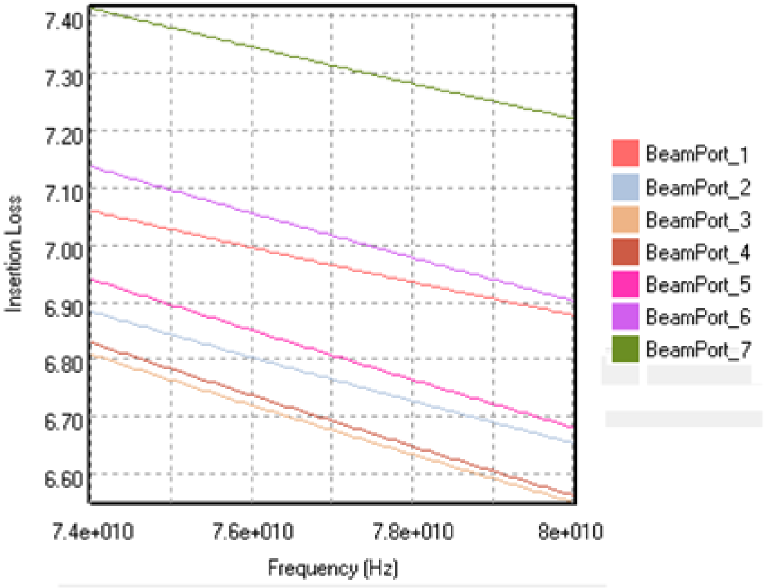

Figure 5.6: The simulated average insertion loss of the beam ports for the designed lens of Figure 5.5.

connect the top metal to the gold substrate. The measurement is performed using a Cascade 11000 probe station set-up. The Cascade infinity waveguide probes with

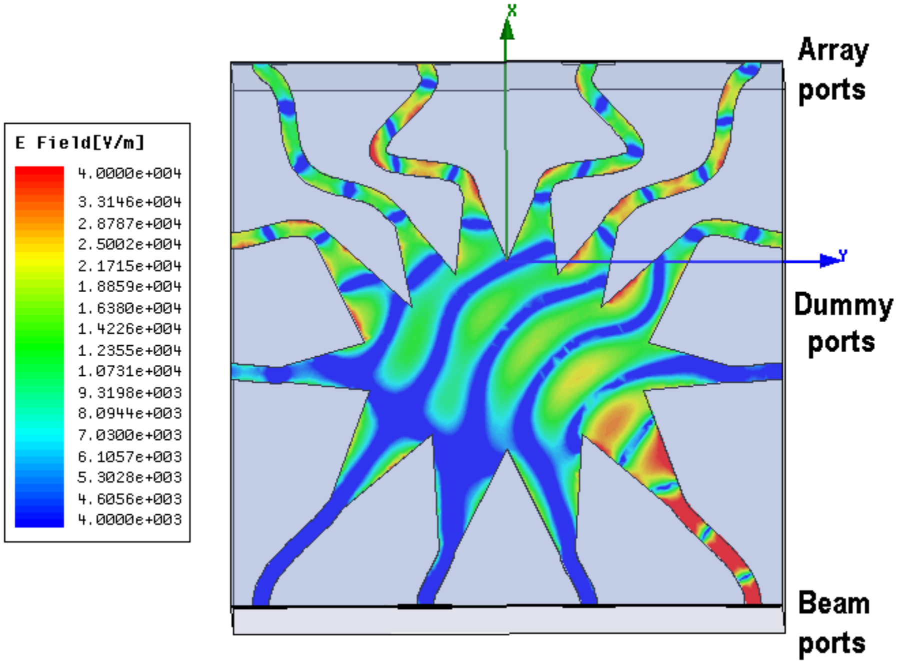

Figure 5.7: Simulated Electric field distribution for the designed 4 by 4 lens on an Alumina substrate at 77 GHz.

Figure 5.8: Photo of the fabricated 77 GHz Rotman lens on Alumina substrate.

a 100 μm pitch size are calibrated using the impedance standard substrate (ISS) and the standard calibration procedure.

Figure 5.9 shows the simulated and measured array factor for the fabricated lens at 77 GHz. AF1 and AF2, show the array factor resulted from the center and corner beam ports which peak at 13° and 39°, respectively. A good agreement between simulation and measurement verifies the design procedure.

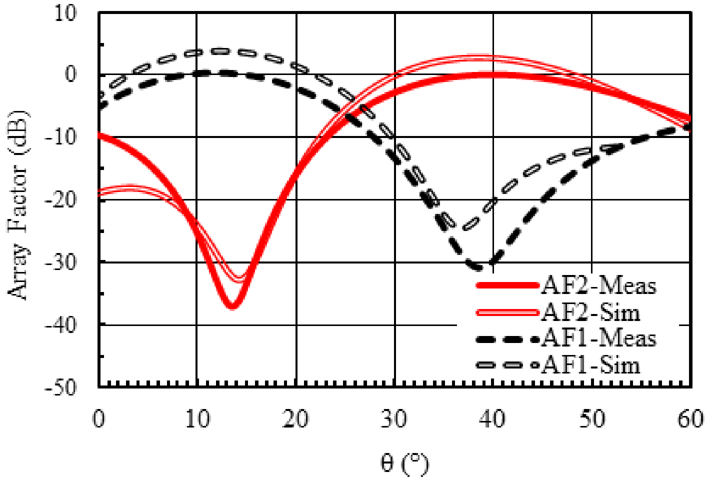

Figure 5.9: The simulated and measured array factor for the fabricated lens at 77 GHz.

5.5 Conclusion

In this chapter, the design and fabrication of an efficient miniaturized Rotman lens for mmW band is presented. A 4 by 4 microstrip lens is fabricated on a low cost Alumina substrate and using conventional microstrip lines to ease its integration with the active parts of the system. To improve the efficiency of the lens, it is optimized by choosing a very small Focal Lens Ratio (FL).

A considerable measured efficiency of greater than 30% is achieved at 77 GHz for the fabricated lens while its dimensions are less than 6 mm. The array factor of the fabricated lens is calculated, using its measured S-parameters. This shows a good agreement with the simulation results.

Chapter 6

CONCLUSIONS AND FUTURE DIRECTIONS

6.1 Conclusion and Contributions

In the course of this research, a new active Rotman lens architecture is proposed as a cost-effective solution for implementation of future mmW imaging, RADAR and radio systems for general purpose applications. The proposed architecture boosts the sensitivity of passive mmW imaging systems by combining a beam-scanning lens and many high-gain LNAs CMOS chips in a miniaturized package.

The proposed architecture combines Rotman lens interesting features including its wide beam-scanning abilities, low cost, low profile, true time delay operation, wide scan angle and wide band performance with cost-effective with high integration capability of the silicon technology to provide an ultimate solution to implement a high performance and cost-effective mmW beam scanning receiver. And most importantly, this architecture allows for the parallel processing of the signals at the beam ports and eliminate the need for antenna feed network.

A system overview for the proposed active Rotman lens architecture is presented in chapter 2 after a short review of the state-of-the-art passive imaging systems and atmospheric frequency windows in propagation constraints at this range of frequencies. The architecture is compared with the conventional configurations and sensitivity improvement is fully discussed. Trade-off's between the different parameters of the proposed architecture are performed. it is shown that for a poor detector performance of NEP=100 or $10\,pW/\sqrt{Hz}$ available in the COMS or SiGe technologies, an LNA with 50 or 35 dB gain will be required, respectively, with a maximum 10 dB noise figure.

As the current microwave CMOS LNAs have a limited gain and band-width and consume a high power supply and a large chip area, a new Band Pass Distributed Amplifier (BPDA) topology is proposed in chapter 3 which is the key element in the proposed active Rotman lens systems. The proposed BPDA topology is analyzed, designed and a few samples are fabricated and tested. The proposed BPDA has a number of advantages for implementation of future miniaturized and wide-band mmW systems using the cost effective CMOS technology.

For the first time, it is shown that using short circuit for the line terminations in distributed amplifiers, which creates a non-traveling (standing) wave in the lines and removes low frequency portion of the DA frequency response, which is most vulnerable to oscillation. The intrinsic impedances of both the amplifying transistors and the transmission lines also contribute to the stability of the circuit. This is very advantageous especially when a lossy fabrication technology such as low-cost CMOS is used. In addition, as no additional resistance for the line terminations is used, the proposed circuit has less power dissipation; resulting in higher power efficiency, lower noise figure and significantly higher amplification gain. Another advantage of the proposed topology is that since no termination impedances are used in the line terminations; the footprint of the circuit for integrated circuit fabrication is significantly smaller in comparison to that of the CDAs.

Also, in chapter 3, the frequency response and design formulas for a single stage BPDA are derived and presented using the lumped element model for inductors in the circuit. It is shown that the transfer function and the designed formula are only accurate up to the microwave frequency range. The transfer function obtained by the transmission line theory can be used for higher frequencies. Using the obtained transfer function, a 2nd order approximation is made to derive the design formula which is valid up to mmW band.

The input and output reflection coefficients are calculated for the modified BPDA topology and it is shown that by a suitable optimization technique, proper input and output matchings can be achieved at the required band. Since the transistors show a bi-lateral behavior at mmW, the stability of the amplifier is studied.

It is shown that if the amplifier is not unconditionally stable, the stability can be achieved by inserting a small degenerative source inductor.

In chapter 4, a new methodology to design a low noise and stable BPDA is presented and based on the proposed design techniques, cascaded BPDAs for different mmW frequencies are designed, fabricated and successfully tested. Fabricated LNAs at 60 and 85 GHz demonstrated that a measured peak gain of 14.7 dB and 10 dB with a 3 dB bandwidth of 7 and 11 GHz, respectively, are achievable using only 4 transistors on a low cost 130 nm technology. The noise figure of the 60 GHz LNA is measured to be 6 dB. The measured results are in a good agreement with the simulations. The core chip size for these amplifiers are 0.105 and 0.06 mm^2, respectively.

Simulations show that with further optimizations, a much higher gain can be obtained. Using 6 transistors in the same technology, 33 dB and 28 dB can be achieved at 60 and 75 GHz, respectively, with a 3 dB bandwidth 5 GHz.

Moreover, a multi-stage high performance wide-band BPDA has been designed which shows the ability of the proposed topology for fabrication of wide band mmW amplifiers using the CMOS technology. 20.5 dB peak gain with a considerable 3 dB bandwidth of 38 GHz from 30 to 68 GHz is achieved while the noise figure is better than 6 dB in the whole bandwidth and closed to the NF_{min}.

A significant result of this research is the proof of feasibility of high gain and wide-band amplification at frequencies above the cut-off frequency of the technology, f_T, by using the proposed BPDA topology.

To compare the results with the state of the art technology, a LNA figure of merit in terms of gain, noise figure, technology cost, chip area, band width, power consumption is defined which shows the superiority of the proposed topology in high performance, wide-band and high frequency LNAs.

Finally in chapter 5, the design and fabrication of a miniaturized mmW Rotman lens is presented. A few lenses are designed and optimized by choosing a very small Focal Lens Ratio (FL) and low cost substrate technologies. A 4 by 4 Rotman lens is fabricated using a low cost Alumina substrate and using conventional microstrip line technology to ease its integration with the active parts of the system. A measured efficiency of greater than 30% is achieved at 77 GHz while the lens dimensions are less than 6 mm.

6.2 Future Research Directions

High performance and low cost CMOS LNAs are key building blocks to develop future mmW, sub-mmW and Terahertz sensing and imaging systems. The integrated active Rotman lens is an ultimate solution to overcome the technology limitations, the intrinsic material loss and high attenuation in common propagating media at the mmW and THz bands. With the rapid advancement of nano-metric silicon integrated circuit technologies and the ability to integrate them with the high quality passive components, this will continue to be a hot research area for the future.

The future research directions based on the outcome of this research include:

- Development of extremely wide-band receiver architectures at mmW and THz for passive mmW imaging systems.
- Development of dielectric Rotman lens for mmW and THz beam forming networks.
- Investigation of novel low cost active and passive circuits and systems for wireless communication, RADAR and imaging applications above 100 GHz.
- Development, design, characterization and modeling of passive and active devices up to 500 GHz, including noise figure measurement and noise characterization.
- Development of packaging and integration technologies to combine passive and active circuits and devices at mmW and THz bands.

APPENDICES

Appendix A

An accurate, simple and scalable model for mmW CMOS transistors

Rapid scaling in CMOS technology, created a great interest in mmW circuits for many applications (see section 1.1). A low noise amplifier is a critical circuit to build sensitive receivers for these applications. However, lack of accurate and simple models for circuit components has resulted difficulties for circuit optimization and discrepancy between simulated and measured performance of these amplifiers.

Transistor modeling is usually done using the physical intrinsic device model provided by the foundry. This model is very complicated and cannot be easily used in circuit optimization. Moreover, the parasitics from layout interconnections which greatly impact the transistor behaviour at mmW are not included in the intrinsic model. Therefore, the layout should be separately simulated and added to the intrinsic model. This can be done by selecting transistor geometry and simulating its extrinsic parasitics using an EM simulator. The extracted parasitics will only be useful for that specific transistor geometry and this limits the circuit optimization as the model is not scalable to other device sizes and geometries. The issue is more critical in mmW amplifier design where many design requirements should be met at the same time. Another method to extract parasitics effect is to use post-layout parasitic extraction tools; however, this method is not accurate enough at mmW due to frequency dependencies of model elements and distributed effects [135]. Measurement of fabricated devices is another method for transistor modeling. Again, the extracted model is limited to the fabricated geometries and does not give information related to design parameters which greatly reduces the design flexibility [107, 136].

In the proposed transistor modeling method, a systematic approach to derive a simple yet accurate and scalable model for transistors is presented to be used in mmW amplifier design. The model is a 2-port one suitable for a common source gain cell with a small source degeneration inductor; however, the methodology can be easily extended to 3-port models.

Fig A.1 shows the 2-port linear transistor model.

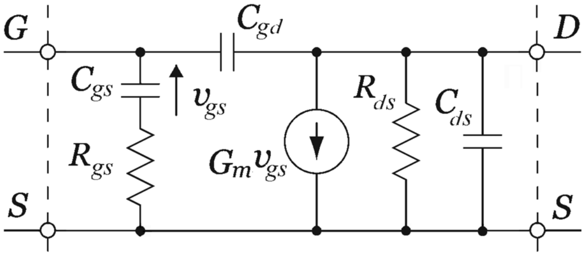

Figure A.1: Two port scalable mmW transistor model

The model values can be easily calculated from 2-port Y-parameters [137, 138]:

$$\begin{aligned}
R_{ds} &= \frac{1}{Re(Y_{22})} \\
C_{gd} &= -\frac{Im(Y_{12})}{\omega} \\
C_{ds} &= \frac{Im(Y_{22})}{\omega} - C_{gd} \\
C_{gs} &= \frac{Im(Y_{11}) - \omega C_{gd}}{\omega}\left[1 + \frac{\Big(Re(Y_{11})\Big)^2}{\Big(Im(Y_{11}) - \omega C_{gd}\Big)^2}\right] \\
R_{gs} &= \frac{Re(Y_{11})}{\Big(Im(Y_{11}) - \omega C_{gd}\Big)^2 + \Big(Re(Y_{11})\Big)^2} \\
g_m &= \sqrt{\Big(\big(Re(Y_{21})\big)^2 + \big(Im(Y_{11}) - \omega C_{gd}\big)^2\Big)(1 + \omega^2 C_{gs}^2 R_{gs}^2)} \\
\tau &= \frac{1}{\omega}\arcsin\left(\frac{-\omega - Im(Y_{21}) - \omega C_{gs} R_{gs} Re(Y_{21})}{g_m}\right)
\end{aligned} \tag{A-1}$$

where $G_m = g_m e^{-j\omega\tau}$.

The transistor S-parameters are obtained for a few different number of gate fingers in the range of interest ($40\mu m < W < 60\mu m$ and 60 GHz< f <110 GHz) by combining the foundry physical model for the intrinsic device and S-parameters of the simulated layouts in HFSS. By converting the resulted S-parameters to Y-parameters and using curve fitting, scalable model values can be easily found from (A-1).

The model values shown in Table A.1 are obtained for 130 nm CMOS transistors at 77 GHz and demonstrate the dependency of model values in terms of transistor gate width ($W = W_{finger}.N_{fingers}, W_{finger} = 1\mu m$) [5]:

Table A.1: Scalable model parameters of transistors versus gate width, W at 77 GHz [5].

$R_{gs}(\Omega)$	688/W-2.5
$R_{ds}(\Omega)$	7774/W-8.7
$C_{gs}(fF)$	0.96W-1.6
$C_{gd}(fF)$	0.34W+0.7
$C_{ds}(fF)$	0.43W+0.27
$g_m(mS)$	0.7W-2
$\tau(fs)$	4800/W-2W+470

The frequency dependency of each parameter is added separately to Table (A.1) using curve fitting to (A-1) for three different transistor gate widths and shown in Fig A.2.

It is seen that C_{ds} and R_{ds} are strongly frequency dependent, while other parameters have less variation with frequency and can be considered constant in a narrow-band analysis.

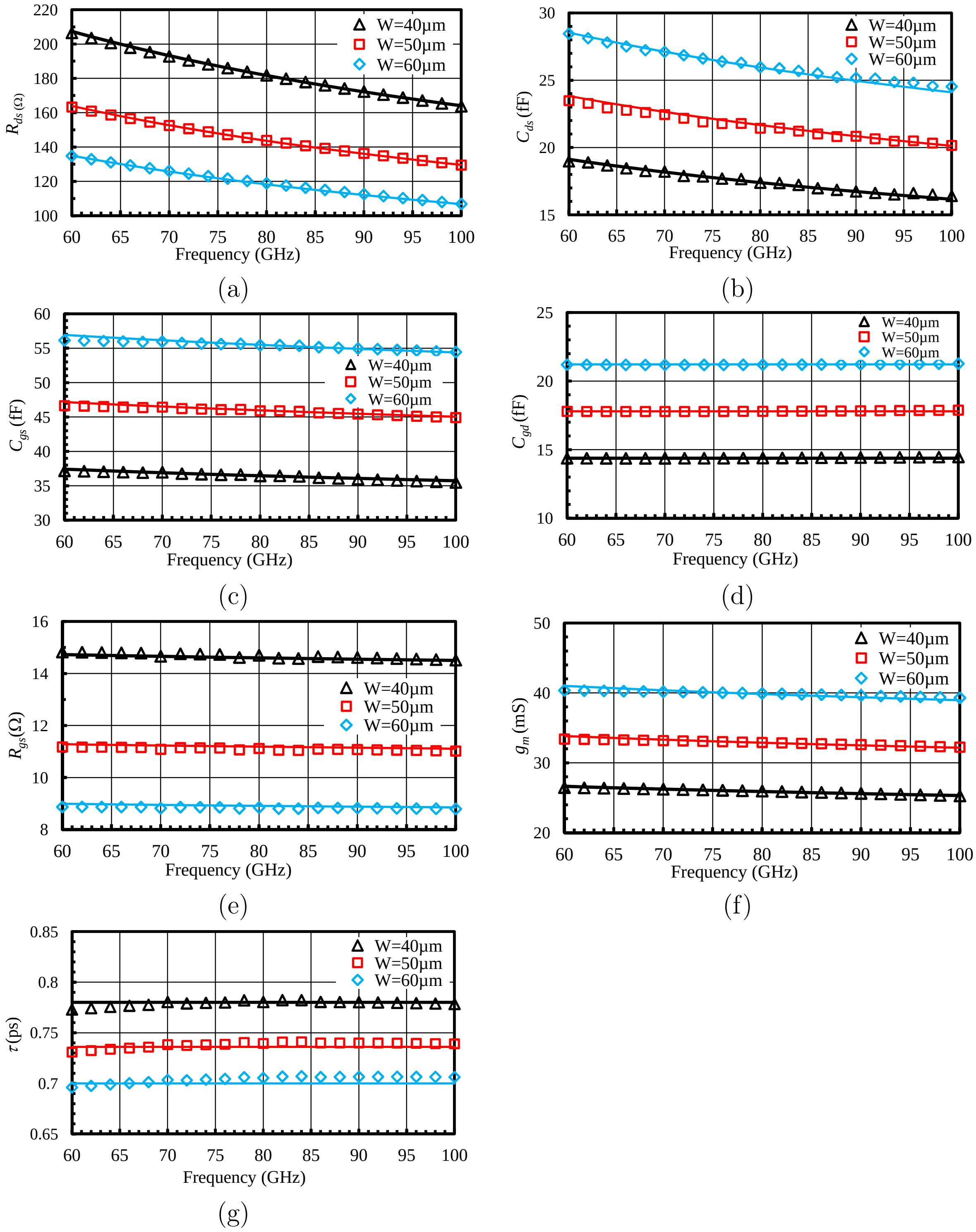

Figure A.2: Frequency dependency of extracted model parameters for three different transistor gate widths. (a) R_{ds} (b) C_{ds} (c) C_{gs} (d) C_{gd} (e) R_{gs} (f) g_m and (g) τ.

Appendix B

Design equations for Rotman lens [11]

The first step in designing the lens is to choose three symmetrical points, F_0, F_1 and F_2, on the focal arc as shown in Figure A.1. Then we introduce the following geometrical quantities as shown in this figure:

Lens Width: (G), the distance of point F_0 to the origin called the on axis focal length.

Off-axis Focal length: (F), the length of F_1O=F_2O.

Scan Angle: (α), the angle between the lens axis and one of the off-axis focal points and is the off axis beam angle for which phase error is zero.

Steering Angle: (φ) obtained by feeding lens from F_1.

Lens Aperture: (N) position of radiating element.

F_0, F_1 and F_2 are perfect focus points. By feeding the lens from these points, a phase-error free excitation is generated at the antenna radiating element, with steering angles of 0, $+\varphi$ and -φ, respectively. The design equations simply consist of mathematical expressions of the conditions that these three rays originating from F_0, F_1 and F_2 and going to the radiation elements at the array plane should have the same electrical length, apart from the delay or phase difference required for the beam tilting in the 0, $+\varphi$ and -φ directions, respectively.

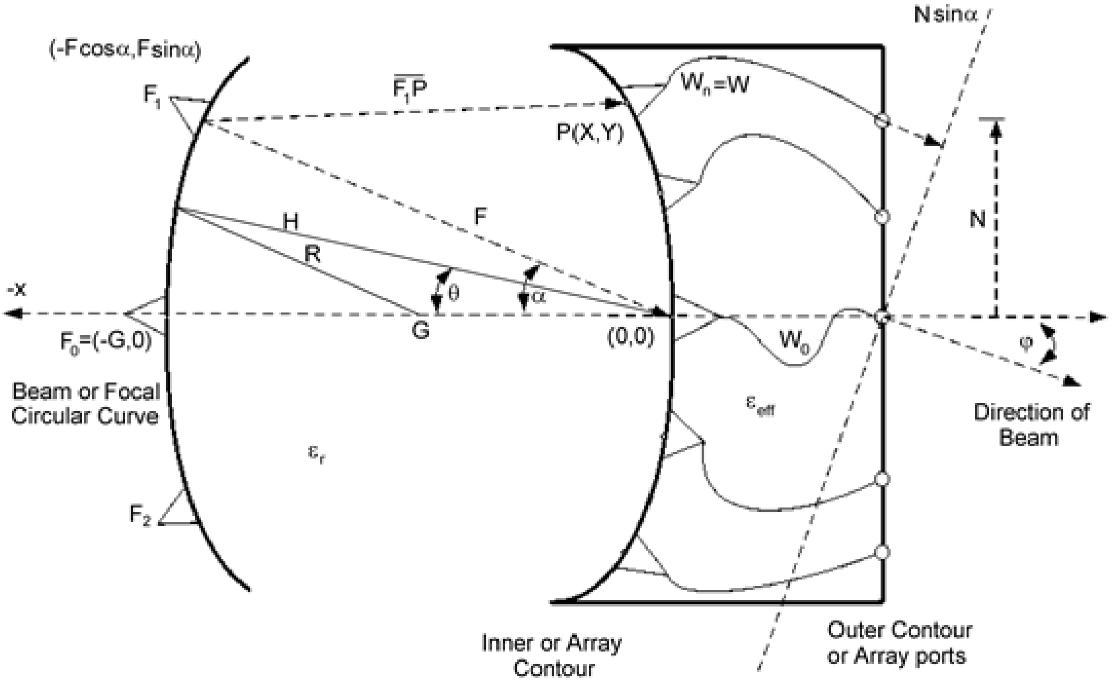

Figure A.1: Diagram of a Rotman lens [11].

It can be easily shown that:

$$\overline{F_1P} + W + N\sin\alpha = F + W_0 \tag{A-1a}$$

$$\overline{F_2P} + W - N\sin\alpha = F + W_0 \tag{A-1b}$$

$$\overline{F_0P} + W = G + W_0 \tag{A-1c}$$

where F_0P, F_1P and F_2P represent path lengths from focal points F_0, F_1 and F_2, respectively to the point P on the array port curve. In equations (A-1), the unknowns are the coordinates of P and the length W.

If instead of air filled parallel plates, dielectric materials is used, (A-1) will be changed to [11]:

$$\begin{gathered}\sqrt{\epsilon_r}\overline{F_1P} + \sqrt{\epsilon_{eff}}W + N\sin\alpha = \sqrt{\epsilon_r}F + \sqrt{\epsilon_{eff}}W_0\\ \sqrt{\epsilon_r}\overline{F_2P} + \sqrt{\epsilon_{eff}}W - N\sin\alpha = \sqrt{\epsilon_r}F + \sqrt{\epsilon_{eff}}W_0\\ \sqrt{\epsilon_r}\overline{F_0P} + \sqrt{\epsilon_{eff}}W = \sqrt{\epsilon_r}G + \sqrt{\epsilon_{eff}}W_0\end{gathered} \tag{A-2}$$

The rest of the procedure would be the same. From geometry of the system illustrated in Figure A.1:

$$\begin{aligned}
\overline{F_1P}^2 &= F^2 + X^2 + Y^2 + 2FX\cos\alpha - 2FY\sin\alpha \\
\overline{F_2P}^2 &= F^2 + X^2 + Y^2 + 2FX\cos\alpha + 2FY\sin\alpha \qquad \text{(A-3)} \\
\overline{F_0P}^2 &= (G+X)^2 + Y^2
\end{aligned}$$

Then we normalize the lengths with respect to the focal length F by defining a new set of input parameters which are used to compute the array contour points as well as the line lengths:

Element Spacing: (η), the spacing of the linear array elements along the outer contour. The spacing is in free-space wavelengths.

Focal Ratio: (g), the ratio of on axis focal length to the off axis focal length. It is used to control the shape of the Focal arc:

$$\begin{aligned}
\eta &= N/F \\
x &= X/F \\
y &= Y/F \\
w &= (W - W_0)/F \qquad \text{(A-4)} \\
g &= G/F \\
a_0 &= \cos\alpha \\
b_0 &= \sin\alpha
\end{aligned}$$

Using (A-4), (A-3) can be written as:

$$\frac{\overline{F_1P}^2}{F^2} = 1 + x^2 + y^2 + 2a_0x - 2b_0y \qquad \text{(A-5a)}$$

$$\frac{\overline{F_2P}^2}{F^2} = 1 + x^2 + y^2 + 2a_0x + 2b_0y \qquad \text{(A-5b)}$$

$$\frac{\overline{F_0P}^2}{F^2} = (g+x)^2 + y^2 \qquad \text{(A-5c)}$$

By using the normalized parameters, (A-4) into (A-1a), one can obtain:

$$\frac{\overline{F_1P}}{F} = 1 + \frac{W_0}{F} - \frac{W}{F} - \frac{N\sin\alpha}{F} = 1 - w - b_0\eta \tag{A-6}$$

Combining (A-5a) and (A-6), results in:

$$\frac{\overline{F_1P}^2}{F^2} = (1 - w - b_0\eta)^2 = 1 + x^2 + y^2 + 2a_0x - 2b_0y \tag{A-7}$$

or:

$$1 + w^2 + b_0^2\eta^2 - 2w - 2b_0\eta + 2b_0w\eta = 1 + x^2 + y^2 + 2a_0x - 2b_0y \tag{A-8}$$

Since the off-axis focal points are symmetrically located, the lens surfaces must also be symmetrical about the center axis. This means that, if η is replaced by -η and y by -y, equation (A-8) should remain unchanged.

Equation (A-8) can therefore be separated into two independent equations; one contains only odd powers of y while the other contains the remaining terms:

$$\underbrace{1 + w^2 + b_0^2\eta^2 - 2w}\overbrace{-2b_0\eta + 2b_0w\eta} = \underbrace{1 + x^2 + y^2 + 2a_0x}\overbrace{-2b_0y} \tag{A-9}$$

Thus:

$$y = \eta(1 - w) \tag{A-10a}$$

$$x^2 + y^2 + 2a_0x = w^2 + 2b_0^2\eta^2 - 2w \tag{A-10b}$$

Therefore, equations (A-1c) and (A-5c) which are related to the on-axis focus, can be written as:

$$\frac{\overline{F_1P}^2}{F^2} = (g - w)^2 = (g + x)^2 + y^2 \tag{A-11}$$

or:

$$x^2 + y^2gx = w^2 - 2gw \tag{A-12}$$

Equations (A-10) and (A-12) can be combined to give the following relation between w and η:

$$aw^2 + bw + c = 0 \tag{A-13}$$

where:

$$a = 1 - \eta^2 - \left(\frac{g-1}{g-a_0}\right)^2 \tag{A-14a}$$

$$b = 2g\left(\frac{g-1}{g-a_0}\right) - \frac{g-1}{(g-a_0)^2}b_0^2\eta^2 - 2g \tag{A-14b}$$

$$c = \frac{gb_0^2\eta^2}{g-a_0} - \frac{b_0^4\eta^4}{4(g-a_0)} - \eta^2 \tag{A-14c}$$

Equation (A-13) is in quadratic form which can be easily solved to complete the lens design. For the given values of α and g we can compute w as a function of η using (A-13). The calculated values can be substituted into the (A-10a) and (A-12) to determine x and y and complete the lens dimensions.

The modified equations to include the permittivity of the lens substrate and the permittivity of the transmission line are given by:

$$\Delta l = \frac{\Delta L}{F} = \sqrt{h^2 + x^2 + y^2 + 2hx\cos\theta - 2hy\sin\theta} - h + w + \eta\sin\theta \tag{A-15}$$

where Δl is the normalized path length error, and $h = H/F$ is the normalized distance from a point on the circular focal arc to the origin. Solving (A-15) along with previous equations, results in lens design parameters as follows:

$$\begin{aligned}
x_n &= W_0 \\
y_n &= -(N-1)d/2 : d : (N-1)d/2 \\
\\
x_{pn} &= w_n \frac{g-1}{a_0(a_0-g)}\sqrt{\frac{\epsilon_{eff}}{\epsilon_r}} + \frac{y_n^2 b_0^2}{2\epsilon_r(a_0-g)F} \\
\\
y_{pn} &= \frac{y_n}{\sqrt{\epsilon_r}}\left(1 - w_n\sqrt{\frac{\epsilon_{eff}}{\epsilon_r}}\right) \\
\\
x_{bn} &= -R\cos\gamma_m - G + r \\
y_{bn} &= R\sin\gamma_m
\end{aligned} \tag{A-16}$$

where d is element spacing and $Aw_n^2 + Bw_n + C = 0$, therefore:

$$A = \left[\frac{(g-1)^2}{(a_0-g)^2} + \frac{y_n^2}{\epsilon_r} - 1\right]\frac{\epsilon_{eff}}{\epsilon_r}$$

$$B = \frac{y_n^2(g-1)s_\alpha^2}{(a-g_0)^2}\sqrt{\frac{\epsilon_{eff}}{\epsilon_r}} - 2y_n^2\sqrt{\frac{\epsilon_{eff}}{\epsilon_r}} + 2\frac{g(g-1)}{(a_0-g)}\sqrt{\frac{\epsilon_{eff}}{\epsilon_r}} + 2g\sqrt{\frac{\epsilon_{eff}}{\epsilon_r}} \tag{A-17}$$

$$C = \left[1 + \frac{s_\alpha^4 y_n^2}{4\epsilon_r(a_0-g)^2}\right]$$

and:

$$w_n = \frac{-B + \sqrt{B^2 - 4AC}}{2A}$$

$$R = \frac{(Fa_0 - G) + F^2 b_0}{2(G - Fa_0)} \tag{A-18}$$

$$\gamma_m = -\alpha + \frac{2\alpha(m-1)}{M-1}$$

Bibliography

[1] M. Fahimnia, S. Safavi-Naeini, M. Mohammad-Taheri, and Y. Wang, "DISTRIBUTED AMPLIFIER FOR BAND PASS RADIO FRONT-END," Europian Patent EP 2 462 692 A1, June 11, 2012.

[2] M. Mohammad-Taheri, M. Fahimnia, Y. Wang, M. Yu, and S. Safavi-Naeini, "Wave analysis for inductively matched millimeter wave amplifier design," *Progress In Electromagnetics Research C*, vol. 13, pp. 41–50, 2010.

[3] M. Fahimnia, M. Mohammad-Taheri, B. Biglarbeigian, and S. Safavi-Naeini, "Characterization of a high-Q on-chip transmission line for CMOS MMIC applications," in *19th Iranian Conference on Electrical Engineering (ICEE 2011)*, Tehran, IR, 17-19 May 2011, pp. 1–4.

[4] M. Fahimnia, M. Mohammad-Taheri, Y. Wang, M. Yu, and S. Safavi-Naeini, "A 59-66 GHz Highly Stable Millimeter Wave Amplifier in 130 nm CMOS Technology," *IEEE Microw. Wireless Compon. Lett.*, vol. 21, no. 6, pp. 320–322, May 2011.

[5] M. Fahimnia, M. Mohammad-Taheri, Y. Wang, S. Safavi-Naeini, and M. Yu, "Optimum millimetre-wave amplifier design using scalable models for circuit elements," *Electronics Letters*, vol. 46, no. 13, pp. 928 –930, June 2010.

[6] E. Brown, "Fundamentals of terrestrial millimeter-wave and thz remote sensing," *International journal of high speed electronics and systems*, vol. 13, no. 04, pp. 995–1097, 2003.

[7] P. Hall and S. Vetterlein, "Review of radio frequency beamforming techniques for scanned and multiple beam antennas," in *IEE Proceedings H Microwaves, Antennas and Propagation*, vol. 137, no. 5. IET, Oct. 1990, pp. 293–303.

[8] J. Wells, *Multi-Gigabit Microwave and Millimeter-Wave Wireless Communications.* Artech House Publishers, 2010.

[9] V. Gregers-Hansen. Radio Propagation at 90 GHz. Accessed: Dec. 2012. [Online]. Available: http://transition.fcc.gov/Bureaus/Engineering_Technology/Documents/presentations/nrl_vg.ppt

[10] K. Moez and M. Elmasry, "Design of broadband bandpass CMOS amplifiers based on modified distributed amplification technique," in *48th Midwest Symposium on Circuits and Systems*. IEEE, 2005, pp. 794–797.

[11] R. Haupt and G. Design, *Antenna arrays*. Wiley Online Library, 1996.

[12] R. I. Microstrip, stripline and cpw design. Accessed Dec. 2012. [Online]. Available: http://www.qsl.net/va3iul/Microstrip_Stripline_CPW_Design/Microstrip_Stripline_and_CPW_Design.pdf

[13] H. Y.-S. Lee, *Principles of Terahertz Science and Technology*. Oregon, US: Springer, 2008, vol. 109.

[14] W. L. Chan, J. Deibel, and D. M. Mittleman, "Imaging with terahertz radiation," *Reports on Progress in Physics*, vol. 70, no. 8, p. 1325, 2007. [Online]. Available: http://stacks.iop.org/0034-4885/70/i=8/a=R02

[15] D. Woolard, W. Loerop, and M. Shur, *Terahertz Sensing Technology: Emerging scientific applications and novel device concepts*, ser. Selected Topics in Electronics and Systems. World Scientific, 2004. [Online]. Available: http://books.google.ca/books?id=QgwPrSBDROUC

[16] J. Federici and L. Moeller, "Review of terahertz and subterahertz wireless communications," *Journal of Applied Physics*, vol. 107, no. 11, pp. 111 101 –111 101–22, June 2010.

[17] N. Kukutsu *et al.*, "Toward practical applications over 100 GHz," in *IEEE MTT-S International Microwave Symposium Digest (MTT)*, May 2010, pp. 1134–1137.

[18] T. Nagatsuma *et al.*, "Giga-bit wireless link using 300-400 GHz bands," in *MWP '09. International Topical Meeting on Microwave Photonics*, Oct. 2009, pp. 1 –4.

[19] T. Rappaport, F. Gutierrez, and T. Al-Attar, "Millimeter-Wave and Terahertz Wireless RFIC and On-Chip Antenna Design: Tools and Layout Techniques," in *IEEE GLOBECOM Workshops*, Dec. 2009, pp. 1 –7.

[20]

[21] V. Jain, *Millimeter-Wave Silicon-Based Ultra-Wideband Automotive Radar Transceivers.* Proquest, UMI Dissertation Publishing, 2011, accessed Dec. 2012. [Online]. Available: http://books.google.ca/books?id=b9riuQAACAAJ

[22] K. Wu *et al.*, "Millimeter-wave integrated waveguide antenna arrays and beamforming networks for low-cost satellite and mobile systems," in *Proceedings of the Fourth European Conference on Antennas and Propagation (EuCAP)*, Apr. 2010, pp. 1 –5.

[23] V. Vdovin and I. Zinchenko, "Modern millimeter and submillimeter receiver systems for radio astronomy," *Radiophysics and Quantum Electronics*, vol. 52, pp. 461–471, 2009.

[24] M. A. Morgan and J. R. Fisher, "Next Generation Radio Astronomy Receiver Systems," *arXiv preprint arXiv:0908.3849*, 2009.

[25] P. Siegel, "Terahertz technology in biology and medicine," *IEEE Transactions on Microwave Theory and Techniques*, vol. 52, no. 10, pp. 2438 – 2447, oct. 2004.

[26] Y. Nikawa, "Medical and dental diagnosis using millimeter-waves," in *APMC 2005. Asia-Pacific Conference Proceedings Microwave Conference Proceedings*, vol. 1, Dec. 2005.

[27] D. T. Petkie, E. Bryan, C. Benton, and B. D. Rigling, "Millimeter-wave radar systems for biometric applications," pp. 748 502–748 502–7, 2009. [Online]. Available: http://dx.doi.org/10.1117/12.830543

[28] V. Emelyanov *et al.*, "Use of bio-resonance effects for medical diagnostics and therapy," in *EuMC 2009. European Microwave Conference*, Oct. 2009, pp. 1591–1594.

[29] I. Kemp, M. Peterson, C. Benton, and D. Petkie, "Sub-mm wave imaging techniques for non-destructive aerospace materials evaluation," *Aerospace and Electronic Systems Magazine, IEEE*, vol. 25, no. 8, pp. 17 –19, Aug. 2010.

[30] N. Karpowicz *et al.*, "Continuous-wave terahertz imaging for non-destructive testing applications," in *IRMMW-THz 2005. The Joint 30th International Conference on Infrared and Millimeter Waves and 13th International Conference on Terahertz Electronics*, vol. 1, Sept. 2005, pp. 329 – 330.

[31] M. Ghasr, B. Carroll, S. Kharkovsky, R. Austin, and R. Zoughi, "Millimeter-wave differential probe for nondestructive detection of corrosion precursor pitting," *IEEE Transactions on Instrumentation and Measurement*, vol. 55, no. 5, pp. 1620 –1627, Oct. 2006.

[32] D. Sheen, D. McMakin, and T. Hall, “Three-dimensional millimeter-wave imaging for concealed weapon detection,” *IEEE Transactions on Microwave Theory and Techniques*, vol. 49, no. 9, pp. 1581 –1592, Sept. 2001.

[33] S. Sundaram and P. Woskov, “Novel millimeter wave sensor concepts for energy, environment, and national security,” in *IRMMW-THz 2009. 34th International Conference on Infrared, Millimeter, and Terahertz Waves*, Sept. 2009, pp. 1 –2.

[34] C. Surussavadee, “Global observations of precipitation using satellite passive millimeter-wave sensors,” in *IGARSS 2008. IEEE International Geoscience and Remote Sensing Symposium*, vol. 1, July 2008, pp. I–126 –I–129.

[35] D. Cimini, E. Westwater, and A. Gasiewski, “Temperature and humidity profiling in the arctic using ground-based millimeter-wave radiometry,” *IEEE Transactions on Geoscience and Remote Sensing*, vol. 48, no. 3, pp. 1381 –1388, Mar. 2010.

[36] G. Farquharson, E. Loew, J. Vivekanandan, and W.-C. Lee, “A new high-altitude airborne millimeter-wave radar for atmospheric research,” in *IGARSS 2007. IEEE International Geoscience and Remote Sensing Symposium*, July 2007, pp. 3313 –3316.

[37] K. Humphreys *et al.*, “Medical applications of terahertz imaging: a review of current technology and potential applications in biomedical engineering,” in *IEMBS ’04. 26th Annual International Conference of the IEEE Engineering in Medicine and Biology Society*, vol. 1, Sept. 2004, pp. 1302 –1305.

[38] A. Arbabian *et al.*, “A 90 GHz Hybrid Switching Pulsed-Transmitter for Medical Imaging,” *IEEE Journal of Solid-State Circuits*, vol. 45, no. 12, pp. 2667 –2681, Dec. 2010.

[39] D. Goshi, Y. Liu, K. Mai, L. Bui, and Y. Shih, “Recent advances in 94 GHz FMCW imaging radar development,” in *MTT ’09. IEEE MTT-S International Microwave Symposium Digest*, June 2009, pp. 77 –80.

[40] H. Hansen, “Standoff Detection Using Millimeter and Submillimeter Wave Spectroscopy,” *Proceedings of the IEEE*, vol. 95, no. 8, pp. 1691 –1704, Aug. 2007.

[41] M. Fahimnia *et al.*, “A 77 GHz low noise amplifier using low-cost 0.13 μm CMOS technology,” in *MNRC 2009. 2nd Microsystems and Nanoelectronics Research Conference*, Oct. 2009, pp. 73 –75.

[42] M. Fahimnia, M. Mohammad-Taheri, Y. Wang, M. Yu, and S. Safavi-Naeini, "An efficient method to design optimum millimeter wave low noise amplifier," in *IEEE Antennas and Propagation Society International Symposium (APSURSI).* IEEE, July 2010, pp. 1 –4.

[43] A. Tomkins, *W-Band Passive and Active Circuits in 65-nm Bulk CMOS for Passive Imaging Applications.* MSc Thesis, University of Toronto, 2010, accessed Dec. 2012. [Online]. Available: https://tspace.library.utoronto.ca/bitstream/1807/24285/11/Tomkins_Alexander_20103_MASc_thesis.pdf

[44] H. Moyer *et al.*, "A low noise chipset for passive millimeter wave imaging," in *IEEE/MTT-S Internation Microwave Symposiumal*, June 2007, pp. 1363 –1366.

[45] J. W. May and G. M. Rebeiz, "Design and Characterization of W-band SiGe RFICs for Passive Millimeter-Wave Imaging," *IEEE Trans. on Microwave Theory and Techniques*, vol. 58, no. 5, pp. 1420–1430, May 2010.

[46] E. Ojefors, A. Lisauskas, D. Glaab, H. Roskos, and U. Pfeiffer, "Terahertz Imaging Detectors in CMOS Technology," *Journal of Infrared, Millimeter and Terahertz Waves*, vol. 30, pp. 1269–1280, 2009. [Online]. Available: http://dx.doi.org/10.1007/s10762-009-9569-4

[47] J. Nemarich, "Microbolometer detectors for passive millimeter-wave imaging," DTIC Document, Tech. Rep., 2005.

[48] K. Mizuno *et al.*, "New applications of millimeter-wave incoherent imaging," in *2005 IEEE MTT-S International Microwave Symposium Digest.* IEEE, 2005.

[49] S. Lee *et al.*, "A V-band beam-steering antenna on a thin-film substrate with a flip-chip interconnection," *IEEE Microwave and Wireless Components Letters*, vol. 18, no. 4, pp. 287–289, 2008.

[50] A. Lettington *et al.*, "Design and development of a high-performance passive millimeter-wave imager for aeronautical applications," in *Defense and Security.* International Society for Optics and Photonics, 2004, pp. 210–218.

[51] J. Lovberg, C. Martin, and V. Kolinko, "Video-rate passive millimeter-wave imaging using phased arrays," in *IEEE/MTT-S International Microwave Symposium, 2007.* IEEE, 2007, pp. 1689–1692.

[52] H. Kazemi *et al.*, "Ultra sensitive ErAs/InAlGaAs direct detectors for millimeter wave and THz imaging applications," in *IEEE/MTT-S International Microwave Symposium*, June 2007, pp. 1367 –1370.

[53] N. Su, R. Rajavel, P. Deelman, J. Schulman, and P. Fay, “Sb-Heterostructure Millimeter-Wave Detectors With Reduced Capacitance and Noise Equivalent Power,” *IEEE Electron Device Letters*, vol. 29, no. 6, pp. 536 –539, June 2008.

[54] M. E. Tiuri, “Radio Astronomy Receivers,” *IEEE Transactions on Military Electronics*, vol. 8, no. 3, pp. 264 –272, July 1964.

[55] W. Horton, J. Jasberg, and J. Noe, “Distributed amplifiers: practical considerations and experimental results,” *Proceedings of the IRE*, vol. 38, no. 7, pp. 748–753, 1950.

[56] W. Chen, “Theory and design of transistor distributed amplifiers,” *IE Journal of Solid-State Circuits*, vol. 3, no. 2, pp. 165–179, 1968.

[57] J. Beyer, S. Prasad, R. Becker, J. Nordman, and G. Hohenwarter, “MESFET distributed amplifier design guidelines,” *IEEE Transactions on Microwave Theory and Techniques*, vol. 32, no. 3, pp. 268–275, 1984.

[58] S. Mohammadi, J. Park, D. Pavlidis, J. Guyaux, and J. Garcia, “Design optimization and characterization of high-gain GaInP/GaAs HBT distributed amplifiers for high-bit-rate telecommunication,” *IEEE Transactions on Microwave Theory and Techniques*, vol. 48, no. 6, pp. 1038–1044, 2000.

[59] E. Hamidi, M. Mohammad-Taheri, and G. Moradi, “Improvements in the noise theory of the MMIC distributed amplifiers,” *IEEE Transactions on Microwave Theory and Techniques*, vol. 56, no. 8, pp. 1797–1806, 2008.

[60] M. Parlak and J. Buckwalter, “A low-power dual-channel distributed amplifier for multielement receivers,” *IEEE Transactions on Microwave Theory and Techniques*, vol. 59, no. 2, pp. 435–442, 2011.

[61] K. Ansari, C. Plett, and M. Yagoub, “A low-power 0.4-22GHz CMOS cascode distributed amplifier for optical communication systems,” in *ICECS 2009. 16th IEEE International Conference on Electronics, Circuits, and Systems*. IEEE, 2009, pp. 387–390.

[62] A. Safarian and P. Heydari, “UWB Distributed Low Noise Amplifiers (DLNA),” *Silicon-Based RF Front-Ends for Ultra Wideband Radios*, pp. 15–44, 2008.

[63] H. Shigematsu, M. Sato, I. Hirose, F. Brewer, and M. Rodwell, “40Gb/s CMOS distributed amplifier for fiber-optic communication systems,” in *Digest of Technical Papers. ISSCC. 2004 IEEE International Solid-State Circuits Conference*, vol. 1, Feb. 2004, pp. 476 – 540.

[64] F. Zhang and P. Kinget, “Low-power programmable gain CMOS distributed LNA,” *IEEE Journal of Solid-State Circuits*, vol. 41, no. 6, pp. 1333–1343, 2006.

[65] K. Deng, T. Huang, and H. Wang, “Design and analysis of novel high-gain and broad-band GaAs pHEMT MMIC distributed amplifiers with traveling-wave gain stages,” *IEEE Transactions on Microwave Theory and Techniques*, vol. 51, no. 11, pp. 2188–2196, 2003.

[66] K. Moez and M. Elmasry, “Area-efficient CMOS distributed amplifier using compact CMOS interconnects,” *Electronics letters*, vol. 42, no. 17, pp. 970–972, 2006.

[67] M. Egels, J. Gaubert, P. Pannier, and S. Bourdel, “A 52 GHz, 8.5 dB Traveling Wave Amplifier in 0.13 μm standard CMOS process,” in *IEEE Radio Frequency Integrated Circuits (RFIC) Symposium.* IEEE, 2007, pp. 391–394.

[68] K. Moez and M. Elmasry, “A new loss compensation technique for CMOS distributed amplifiers,” *IEEE Transactions on Circuits and Systems II: Express Briefs*, vol. 56, no. 3, pp. 185–189, 2009.

[69] J. Plouchart *et al.*, “A 4-91-GHz traveling-wave amplifier in a standard 0.12-μm SOI CMOS microprocessor technology,” *IEEE Journal of Solid-State Circuits*, vol. 39, no. 9, pp. 1455–1461, 2004.

[70] C. Pavageau *et al.*, “A 7-dB 43-GHz CMOS distributed amplifier on high-resistivity SOI substrates,” *IEEE Transactions on Microwave Theory and Techniques*, vol. 56, no. 3, pp. 587–598, 2008.

[71] M. Tsai, H. Wang, J. Kuan, and C. Chang, “A 70GHz cascaded multi-stage distributed amplifier in 90nm CMOS technology,” in *ISSCC. 2005 IEEE International Solid-State Circuits Conference, 2005. Digest of Technical Papers.* IEEE, 2005, pp. 402–606.

[72] A. Arbabian and A. Niknejad, “A tapered cascaded multi-stage distributed amplifier with 370GHz GBW in 90nm CMOS,” in *RFIC 2008. IEEE Radio Frequency Integrated Circuits Symposium.* IEEE, 2008, pp. 57–60.

[73] M. Chen *et al.*, “A 1–25 GHz GaN HEMT MMIC Low-Noise Amplifier,” *IEEE Microwave and Wireless Components Letters*, vol. 20, no. 10, pp. 563–565, 2010.

[74] M. Krcmar *et al.*, “Sige hbt wideband amplifier for millimetre wave applications,” in *Microwaves, Radar & Wireless Communications, 2006. MIKON 2006. International Conference on.* IEEE, 2006, pp. 1047–1050.

[75] H. Chang *et al.*, "Design and analysis of a DC–43.5 GHz fully integrated distributed amplifier using GaAs HEMT–HBT cascode gain stage," *IEEE Transactions on Microwave Theory and Techniques*, vol. 59, no. 2, pp. 443–455, 2011.

[76] J. Liang and C. Aitchison, "Gain performance of cascade of single stage distributed amplifiers [microwave circuits]," *Electronics Letters*, vol. 31, no. 15, pp. 1260–1261, 1995.

[77] B. Banyamin and M. Berwick, "Analysis of the performance of four-cascaded single-stage distributed amplifiers," *IEEE Transactions on Microwave Theory and Techniques*, vol. 48, no. 12, pp. 2657–2663, 2000.

[78] K. Koon, Z. Hu, P. Langlois, and A. Rezazadeh, "Improving baseband performance of four-cascaded single stage distributed amplifiers for high speed optical communication," in *EDMO 2002. The 10th IEEE International Symposium on Electron Devices for Microwave and Optoelectronic Applications.* IEEE, 2002, pp. 254–258.

[79] M. Tsai *et al.*, "A miniature 25-GHz 9-dB CMOS cascaded single-stage distributed amplifier," *IEEE Microwave and Wireless Components Letters*, vol. 14, no. 12, pp. 554–556, 2004.

[80] P. Chen, P.-C. Huang, J.-J. Kuo, and H. Wang, "A 22-31 GHz Distributed Amplifier Based on High-Pass Transmission Lines Using 0.18 mum CMOS Technology," *IEEE Microwave and Wireless Components Letters*, vol. 21, no. 3, pp. 160 –162, Mar. 2011.

[81] M. Yazgi and A. Toker, "Improving the gain-frequency performance of cascaded single-stage distributed amplifiers with bandpass filter structure," *Analog Integrated Circuits and Signal Processing*, vol. 39, no. 2, pp. 157–167, 2004.

[82] F. Thompson, "Broad-Band UHF Distributed Amplifiers Using Band-Pass Filter Techniques," *IRE Transactions on Circuit Theory*, vol. 7, no. 5, pp. 8–17, 1960.

[83] B. Minnis, "Novel variation of distributed amplifier for millimetre-wave operation," *Electronics Letters*, vol. 24, no. 9, pp. 513–514, 1988.

[84] S. Prasad, A. Kajjam, and Z. Li, "Bandpass distributed amplifier design guidelines," *Microwave and Optical Technology Letters*, vol. 10, no. 4, pp. 215–218, 1995.

[85] N. Mehta and P. Shastry, "Design guidelines for a novel bandpass distributed amplifier," in *2005 European Microwave Conference*, vol. 1. IEEE, 2005.

[86] F. Ng-Molina, T. Martín-Guerrero, and C. Camacho-Peñalosa, “Experimental large-signal performance of a dual-fed band-pass distributed amplifier,” in *Workshop on Integrated Nonlinear Microwave and Millimeter-Wave Circuits (INMMIC).* IEEE, 2010, pp. 164–167.

[87] T. Gathman and J. Buckwalter, “A Ka-band high-pass distributed amplifier in 120nm SiGe BiCMOS,” in *2010 IEEE MTT-S International Microwave Symposium Digest (MTT).* IEEE, 2010, pp. 952–955.

[88] P. Wu, H. Chang, M. Tsai, T. Huang, and H. Wang, “New miniature 15-20-GHz continuous-phase/amplitude control MMICs using 0.18-μm CMOS technology,” *IEEE Transactions on Microwave Theory and Techniques*, vol. 54, no. 1, pp. 10–19, 2006.

[89] P. Heydari, “Design and analysis of a performance-optimized cmos uwb distributed lna,” *Solid-State Circuits, IEEE Journal of*, vol. 42, no. 9, pp. 1892–1905, 2007.

[90] J. Rollett, “Stability and power-gain invariants of linear twoports,” *IRE Transactions on Circuit Theory*, vol. 9, no. 1, pp. 29–32, 1962.

[91] G. Gonzalez, *Microwave transistor amplifiers: analysis and design.* Prentice hall New Jersey, 1997, vol. 2.

[92] M. Edwards and J. Sinsky, “A new criterion for linear 2-port stability using a single geometrically derived parameter,” *IEEE Transactions on Microwave Theory and Techniques*, vol. 40, no. 12, pp. 2303–2311, 1992.

[93] Y. Zhang and T. Wong, “Prospects of CMOS technology for millimeter-wave radio-over-fiber applications,” in *2010 International Conference on Microwave and Millimeter Wave Technology (ICMMT).* IEEE, 2010, pp. 476–479.

[94] A. Margomenos, “A comparison of si cmos and sige bicmos technologies for automotive radars,” in *Silicon Monolithic Integrated Circuits in RF Systems, 2009. SiRF’09. IEEE Topical Meeting on.* IEEE, 2009, pp. 1–4.

[95] Y. Zhao, Y. Jin, M. Spirito, and J. Long, “Millimeter-wave passive components on silicon for wireless communication applications,” in *ICECS 2009. 16th IEEE International Conference on Electronics, Circuits, and Systems.* IEEE, 2009, pp. 972–975.

[96] J. Hasani, M. Kamarei, and F. Ndagijimana, “Sub-nH inductor modeling and design in 90-nm CMOS technology for millimeter-wave applications,” *IEEE Transactions on Circuits and Systems II: Express Briefs*, vol. 55, no. 6, pp. 517–521, 2008.

[97] J. Lee and C. Park, "A slow-wave microstrip line with a high-Q and a high dielectric constant for millimeter-wave CMOS application," *IEEE Microwave and Wireless Components Letters*, vol. 20, no. 7, pp. 381–383, 2010.

[98] A. Mangan, *Millimetre-wave device characterization for nano-CMOS IC design.* University of Toronto, 2005, accessed Dec. 2012.

[99] W. Eisenstadt and Y. Eo, "S-parameter-based IC interconnect transmission line characterization," *IEEE Transactions on Components, Hybrids, and Manufacturing Technology*, vol. 15, no. 4, pp. 483–490, 1992.

[100] M. Ferndahl *et al.*, "A general statistical equivalent-circuit-based de-embedding procedure for high-frequency measurements," *IEEE Transactions on Microwave Theory and Techniques*, vol. 56, no. 12, pp. 2692–2700, 2008.

[101] Y. Tretiakov *et al.*, "On wafer de-embedding for SiGe/BiCMOS/RFCMOS transmission line interconnect characterization," in *Proceedings of the IEEE 2004 International Interconnect Technology Conference.* IEEE, 2004, pp. 166–168.

[102] M. Siti, N. Mohd, A. Marzuki, A. Rahim, and R. Mohamed, "Characterization of on-wafer RF passive components for RFIC devices using three-steps de-embedding method," in *IEEE 9th Malaysia International Conference on Communications (MICC).* IEEE, 2009, pp. 362–366.

[103] Accessed Dec. 2012. [Online]. Available: http://www.ansys.com/Products/Simulation+Technology/Electromagnetics/High-Performance+Electronic+Design/ANSYS+HFSS

[104] A. Mangan, S. Voinigescu, M. Yang, and M. Tazlauanu, "De-embedding transmission line measurements for accurate modeling of IC designs," *IEEE Transactions on Electron Devices*, vol. 53, no. 2, pp. 235–241, 2006.

[105] C. Pavageau *et al.*, "A 60-GHz LNA and a 92-GHz low-power distributed amplifier in CMOS with above-IC," in *EuMIC 2008. European Microwave Integrated Circuit Conference.* IEEE, 2008, pp. 250–253.

[106] C. Huang, H. Kuo, T. Huang, and H. Chuang, "Low-power, high-gain V-band CMOS low noise amplifier for microwave radiometer applications," *IEEE Microwave and Wireless Components Letters*, vol. 21, no. 2, pp. 104–106, 2011.

[107] C. Doan, S. Emami, A. Niknejad, and R. Brodersen, "Millimeter-wave CMOS design," *IEEE Journal of Solid-State Circuits*, vol. 40, no. 1, pp. 144–155, 2005.

[108] B. Heydari, *CMOS circuits and devices beyond 100 GHz.* ProQuest, 2008.

[109] K. Kim, K. Ahn, T. Lim, H. Park, and J. Yu, "A 60 GHz wideband phased-array LNA with short-stub passive vector generator," *IEEE Microwave and Wireless Components Letters*, vol. 20, no. 11, pp. 628–630, 2010.

[110] X. Guan and C. Nguyen, "Low-power-consumption and high-gain CMOS distributed amplifiers using cascade of inductively coupled common-source gain cells for UWB systems," *IEEE Transactions on Microwave Theory and Techniques*, vol. 54, no. 8, pp. 3278–3283, 2006.

[111] G. Yang, Z. Wang, L. Qin, and K. Wang, "A Q-band common source low noise amplifier using 90-nm RF CMOS process," in *2011 3rd International Conference on Computer Research and Development (ICCRD)*, vol. 3. IEEE, 2011, pp. 430–433.

[112] Z. Deng and A. Niknejad, "On the noise optimization of CMOS common-source low-noise amplifiers," *IEEE Transactions on Circuits and Systems I: Regular Papers*, vol. 58, no. 4, pp. 654–667, 2011.

[113] B. Razavi, "A 60-GHz CMOS receiver front-end," *IEEE Journal of Solid-State Circuits*, vol. 41, no. 1, pp. 17–22, 2006.

[114] Accessed Dec. 2012. [Online]. Available: http://www.home.agilent.com/en/pc-1297113/advanced-design-system-ads?&cc=CA&lc=eng

[115] K. Maruhashi *et al.*, "60-GHz-band CMOS MMIC technology for high-speed wireless personal area networks," in *CSIC'08. IEEE Compound Semiconductor Integrated Circuits Symposium.* IEEE, 2008, pp. 1–4.

[116] A. Niknejad and R. Meyer, *Design, simulation and applications of inductors and transformers for Si RF ICs.* Springer, 2000, vol. 586.

[117] W. Rotman and R. Turner, "Wide-angle microwave lens for line source applications," *Antennas and Propagation, IEEE Transactions on*, vol. 11, no. 6, pp. 623–632, 1963.

[118] Z. L. Sun and W. B. Dou, "Far-field pattern of a focal-plane array-lens antenna at millimeter wavelengths," *International Journal of Infrared and Millimeter Waves*, vol. 19, pp. 673–685, 1998, 10.1023/A:1022630422177. [Online]. Available: http://dx.doi.org/10.1023/A:1022630422177

[119] J. Blass, "Multidirectional antenna - a new approach to stacked beams," in *IRE International Convention Record*, vol. 8, march 1960, pp. 48 –50.

[120] J. Butler, “Beam-forming matrix simplifies design of electronically scanned antennas,” *Electron. Des.*, vol. 9, no. 8, pp. 170–173, 1961.

[121] J. Lee, “Lens antennas,” *Antenna Handbook Theory Applications and Design*, 1988.

[122] J. Ruze, “Wide-angle metal-plate optics,” *Proceedings of the IRE*, vol. 38, no. 1, pp. 53–59, 1950.

[123] H. Gent, “The bootlace aerial,” *Royal Radar Establishment Journal*, pp. 47–57, 1957.

[124] R. Clapp, “Extending the R-2R Lens to 360,” *IEEE Transactions on Antennas and Propagation*, vol. 32, no. 7, pp. 661–671, 1984.

[125] R. Sorrentino and G. Bianchi, *Microwave and RF engineering.* Wiley, 2010, vol. 1.

[126] J. Dong, “Microwave lens designs: Optimization, fast simulation algorithms, and 360-degree scanning techniques,” Ph.D. dissertation, Virginia Polytechnic Institute and State University, 2009.

[127] L. Schulwitz and A. Mortazawi, “A new low loss Rotman lens design using a graded dielectric substrate,” *IEEE Transactions on Microwave Theory and Techniques*, vol. 56, no. 12, pp. 2734–2741, 2008.

[128] W. Lee, J. Kim, and Y. Yoon, “Compact two-layer Rotman lens-fed microstrip antenna array at 24 GHz,” *IEEE Transactions on Antennas and Propagation*, vol. 59, no. 2, pp. 460–466, 2011.

[129] W. Lee, Y. Kim, J. Kim, and Y. Yoon, “Multi-layer beamforming lens antenna array with a new line design for millimeter-wave system-in-package applications,” in *Antennas and Propagation (EUCAP), Proceedings of the 5th European Conference on.* IEEE, 2011, pp. 2954–2958.

[130] P. Singhal, P. Sharma, and R. Gupta, “Rotman lens with equal height of array and feed contours,” *IEEE Transactions on Antennas and Propagation*, vol. 51, no. 8, pp. 2048–2056, 2003.

[131] Y. Cheng *et al.*, “Substrate integrated waveguide (SIW) Rotman lens and its Ka-band multibeam array antenna applications,” *IEEE Transactions on Antennas and Propagation*, vol. 56, no. 8, pp. 2504–2513, 2008.

[132] M. Ettorre, R. Sauleau, and L. Le Coq, “Multi-beam multi-layer leaky-wave SIW pillbox antenna for millimeter-wave applications,” *IEEE Transactions on Antennas and Propagation*, vol. 59, no. 4, pp. 1093–1100, 2011.

[133] Y. Cheng, W. Hong, and K. Wu, “Design of a substrate integrated waveguide modified R-KR lens for millimetre-wave application,” *IET Microwaves, Antennas and Propagation*, vol. 4, no. 4, pp. 484–491, 2010.

[134] E. Sbarra, L. Marcaccioli, R. Gatti, and R. Sorrentino, “A novel Rotman lens in SIW technology,” in *EuRAD 2007. European Radar Conference.* IEEE, 2007, pp. 236–239.

[135] C. Liang and B. Razavi, “Systematic transistor and inductor modeling for millimeter-wave design,” *IEEE Journal of Solid-State Circuits*, vol. 44, no. 2, pp. 450–457, 2009.

[136] T. Suzuki, Y. Kawano, M. Sato, T. Hirose, and K. Joshin, “60 and 77ghz power amplifiers in standard 90nm cmos,” in *IEEE International Solid-State Circuits Conference, ISSCC 2008. Digest of Technical Papers.* IEEE, 2008, pp. 562–636.

[137] G. Dambrine, A. Cappy, F. Heliodore, and E. Playez, “A new method for determining the FET small-signal equivalent circuit,” *IEEE Transactions on Microwave Theory and Techniques*, vol. 36, no. 7, pp. 1151–1159, 1988.

[138] M. Berroth and R. Bosch, “Broad-band determination of the FET small-signal equivalent circuit,” *IEEE Transactions on Microwave Theory and Techniques*, vol. 38, no. 7, pp. 891–895, 1990.

[139] V. Dimitrov *et al.*, “Small-signal performance and modeling of sub-50nm MOSFETs with fT above 460-GHz,” *Solid-state electronics*, vol. 52, no. 6, pp. 899–908, 2008.

[140] M. Krcmar *et al.*, “SiGe HBT Wideband Amplifier for Millimetre Wave Applications,” in *MIKON 2006. International Conference on Microwaves, Radar and Wireless Communications.* IEEE, 2006, pp. 1047–1050.

[141] J. Lovberg, C. Martin, and V. Kolinko, “Video-rate passive millimeter-wave imaging using phased arrays,” in *IEEE/MTT-S International Microwave Symposium.* IEEE, 2007, pp. 1689–1692.

[142] A. Munger, G. Vaughn, J. Provencher, and B. Gladman, “Conical array studies,” *Antennas and Propagation, IEEE Transactions on*, vol. 22, no. 1, pp. 35–43, 1974.

[143] Z. L. Sun and W. B. Dou, “Far-field pattern of a focal-plane array-lens antenna at millimeter wavelengths,” *International Journal of Infrared and Millimeter Waves*, vol. 19, pp. 673–685, 1998, 10.1023/A:1022630422177. [Online]. Available: http://dx.doi.org/10.1023/A:1022630422177